EUROPEAN ORGANISATION FOR NUCLEAR RESEARCH (CERN)

Submitted to: JHEP

CERN-EP-2021-227
2nd February 2022

Measurements of the Higgs boson inclusive and differential fiducial cross-sections in the diphoton decay channel with pp collisions at $\sqrt{s} = 13$ TeV with the ATLAS detector

The ATLAS Collaboration

A measurement of inclusive and differential fiducial cross-sections for the production of the Higgs boson decaying into two photons is performed using 139 fb^{-1} of proton–proton collision data recorded at $\sqrt{s} = 13$ TeV by the ATLAS experiment at the Large Hadron Collider. The inclusive cross-section times branching ratio, in a fiducial region closely matching the experimental selection, is measured to be 67 ± 6 fb, which is in agreement with the state-of-the-art Standard Model prediction of 64 ± 4 fb. Extrapolating this result to the full phase space and correcting for the branching ratio, the total cross-section for Higgs boson production is estimated to be 58 ± 6 pb. In addition, the cross-sections in four fiducial regions sensitive to various Higgs boson production modes and differential cross-sections as a function of either one or two of several observables are measured. All the measurements are found to be in agreement with the Standard Model predictions. The measured transverse momentum distribution of the Higgs boson is used as an indirect probe of the Yukawa coupling of the Higgs boson to the bottom and charm quarks. In addition, five differential cross-section measurements are used to constrain anomalous Higgs boson couplings to vector bosons in the Standard Model effective field theory framework.

Contents

1 Introduction

Following the discovery of the Higgs boson (H) in July 2012 by the ATLAS [1] and CMS [2] collaborations, extensive studies were carried out to precisely measure the properties of the new particle. These studies yielded measurements of the different Higgs boson production mechanisms in several decay modes [3–25], constraints on the spin and parity of the Higgs boson [26, 27], and measurements of the Higgs boson mass, which average to $m_H = 125.09 \pm 0.24$ GeV [28].

The results of these measurements were found to be consistent with the Standard Model (SM) predictions. These measurement were carried out using data from proton–proton (pp) collisions at the Large Hadron Collider (LHC) using the full Run 1 data sets at centre-of-mass energies of $\sqrt{s} = 7$ TeV and 8 TeV, as well as partial and full Run 2 data sets at $\sqrt{s} = 13$ TeV.

Among the possible studies of the properties of the Higgs boson, a particular interest is covered by the measurement of its production cross-section in fiducial regions for which the final-state particles are limited to a specific volume of the phase space defined by the detector acceptance, thus minimising the physics assumptions that would be needed for the extrapolation to the full phase space. In addition, the measured cross-sections are inclusive instead of being split by production process, thus further minimising SM assumptions. The measurements are corrected for detector response effects (unfolding) and yield results that can be compared directly with any current or future theoretical predictions.

This paper presents measurements of fiducial inclusive and differential cross-sections in the $H \to \gamma\gamma$ decay channel. The signature of the Higgs boson in the diphoton final state is a narrow resonance rising above a smooth background in the diphoton invariant mass ($m_{\gamma\gamma}$) distribution with a width consistent with the detector resolution. Despite the small branching ratio for Higgs boson decay into two photons, $(2.27 \pm 0.07) \times 10^{-3}$ for $m_H = 125.09$ GeV [29], the Higgs boson signal can be extracted thanks to the excellent photon reconstruction and identification efficiency of the ATLAS detector. All the measurements are performed assuming a Higgs boson mass of 125.09 GeV, and are compared with SM predictions. Unless explicitly stated otherwise, all results include the Higgs boson branching ratio to two photons.

The measurements presented in this paper follow previous fiducial cross-section measurements using the full Run 1 data set [30] and a partial Run 2 data set [11]. Those measurements showed agreement with SM predictions, and the measured differential cross-sections were used to constrain anomalous coupling of the Higgs boson to other SM particles in an effective field theory (EFT) framework. The study described in this paper relies on the full Run 2 pp collision data set collected at $\sqrt{s} = 13$ TeV at the LHC by the ATLAS detector between 2015 and 2018, corresponding to an integrated luminosity of 139.0 fb^{-1}. This data set is approximately four times larger than the one used in the previous ATLAS publication, and hence it significantly reduces the statistical uncertainty of the measurements. In addition, the latest ATLAS developments in the reconstruction and identification of the various physics objects used in the analysis, namely updates to photon reconstruction and identification and jet reconstruction, are employed. Furthermore, the paper presents measurements of new kinematical observables and new fiducial regions sensitive to the various Higgs boson production modes, including regions that are sensitive to potential beyond-the-SM (BSM) effects.

The paper also reports a measurement of the total Higgs boson production cross-section in the full phase space, as well as two interpretations of the measured fiducial differential cross-sections: constraints on Higgs boson Yukawa couplings to charm and bottom quarks from the differential cross-section as a function of the diphoton transverse momentum, $p_{\mathrm{T}}^{\gamma\gamma}$, and constraints on anomalous couplings of the Higgs boson to other SM particles from a combined fit including several kinematic observables in an EFT approach.

The paper is organised as follows. Section 2 provides a brief description of the ATLAS detector. The data and Monte Carlo samples used are described in Section 3. An overview of the event reconstruction and selection is given in Section 4. Section 5 summarises the definition of the fiducial regions and the differential cross-sections measured by the analysis. The details of the signal and background modelling and of how these models are fitted to the data are provided in Section 6. A summary of the different theoretical and experimental systematic uncertainties is given in Section 7. The measured cross-sections are presented in Section 8. The interpretations of the measured cross-sections are presented in Section 9. The summary and conclusion are given in Section 10.

2 ATLAS detector

The ATLAS detector [31] is a multipurpose particle detector with a forward–backward symmetric cylindrical geometry[1] and a near 4π coverage in solid angle. It consists of an inner tracking detector (ID) surrounded by a thin superconducting solenoid, which provides a 2 T axial magnetic field, electromagnetic (EM) and hadronic calorimeters, and a muon spectrometer (MS).

The inner tracking detector covers the pseudorapidity range $|\eta| < 2.5$. It consists of a silicon pixel detector, including the insertable B-layer [32, 33] installed before Run 2, a silicon microstrip detector, and a straw-tube tracking detector featuring transition radiation to aid in the identification of electrons.

Lead/liquid-argon (LAr) sampling calorimeters provide electromagnetic energy measurements with high granularity. In the region up to $|\eta| = 2.5$ they are segmented longitudinally into three layers and they are complemented with an additional thin LAr presampler covering $|\eta| < 1.8$ to correct for energy loss in material upstream of the calorimeters. A steel/scintillator-tile hadron calorimeter covers the central pseudorapidity range ($|\eta| < 1.7$). The endcap and forward regions are instrumented up to $|\eta| = 4.9$ with LAr calorimeters for both the EM and hadronic energy measurements.

The calorimeters are surrounded by the muon spectrometer, which has three large air-core toroidal superconducting magnets with eight coils each. The field integral of the toroid magnets ranges between 2.0 and 6.0 T m across most of the detector. The muon spectrometer includes a system of precision tracking chambers and fast detectors for triggering with a coverage of $|\eta| < 2.7$.

Events are selected using a first-level trigger implemented in custom electronics, which reduces the event rate to a maximum of 100 kHz using a subset of detector information. Software algorithms with access to the full detector information are then used in the high-level trigger to yield a recorded event rate of about 1 kHz [34].

An extensive software suite [35] is used in the reconstruction and analysis of real and simulated data, in detector operations, and in the trigger and data acquisition systems of the experiment.

[1] ATLAS uses a right-handed coordinate system with its origin at the nominal interaction point (IP) in the centre of the detector and the z-axis along the beam pipe. The x-axis points from the IP to the centre of the LHC ring, and the y-axis points upwards. Cylindrical coordinates (r, ϕ) are used in the transverse plane, ϕ being the azimuthal angle around the z-axis. The pseudorapidity is defined in terms of the polar angle θ as $\eta = -\ln\tan(\theta/2)$. When dealing with massive particles, the rapidity $y = (1/2)\ln[(E + p_z)/(E - p_z)]$ is used, where E is the energy and p_z is the z-component of the momentum. Angular distance is measured in units of $\Delta R = \sqrt{(\Delta\eta)^2 + (\Delta\phi)^2}$.

3 Data and simulation samples

The results presented in this paper are based on the full Run 2 proton–proton collision data at $\sqrt{s} = 13$ TeV recorded by the ATLAS detector between 2015 and 2018. Only data collected while all the detector components were operational are used [36]. The integrated luminosity is 139.0 fb^{-1} and the average number of interactions per bunch-crossing is $\langle\mu\rangle = 34$, varying from 24 in 2015–2016 to 38 in 2017 and 36 in 2018.

Events were selected with a trigger requiring at least two photon candidates with energies greater than 35 and 25 GeV, respectively [37]. In addition, loose photon identification requirements were applied by the trigger in 2015–2016 and were tightened in 2017 and 2018 to cope with the higher instantaneous luminosity. Once the full diphoton event selection described in Section 4 is applied, the average trigger efficiency for $H \to \gamma\gamma$ events is found to be greater than 99% for the 2015–2016 data-taking period, and greater than 98% for the 2017–2018 data-taking period.

Monte Carlo (MC) event generators were used to generate signal samples for the main Higgs boson production modes: gluon–gluon fusion (ggF), vector-boson fusion (VBF), Higgs boson production in association with a vector boson $V = W, Z$ (VH) or with a top-quark pair ($t\bar{t}H$), a bottom-quark pair ($b\bar{b}H$) or a single top quark (tH, with either an additional W boson, tWH, or an additional b-quark and light quark, $tHqb$). About 40 million events were produced with the nominal set-up and almost twice as many with alternative set-ups used to estimate modelling uncertainties, as described later. The samples are normalised to the latest available calculations of the corresponding SM production cross-sections. The normalisation of all Higgs boson samples also accounts for the $H \to \gamma\gamma$ branching ratio of 0.227%, calculated with HDECAY [38–40] and Prophecy4f [41–43].

The events were generated using Powheg Box v2 [44–46] and the PDF4LHC15 PDF set [47], except for tH production events, which were generated with MadGraph5_aMC@NLO 2.6 [48] and the NNPDF3.0nlo PDF set. The mass of the Higgs boson was set to $m_H = 125$ GeV, while the width was set to $\Gamma_H = 4.07$ MeV. For all signal samples, the parton-level events from the generator were interfaced to Pythia 8 [49] for the parton shower and the modelling of the underlying event, with parameter values set according to the AZNLO tune [50] for ggF, VBF and VH production, and to the A14 tune [51] for the others.

Higgs boson production via ggF was generated at next-to-next-to-leading-order (NNLO) accuracy in QCD using Powheg Box v2 [52, 53] and the NNLO family of PDF4LHC15 PDFs. The simulation achieves NNLO accuracy for arbitrary inclusive $gg \to H$ observables by reweighting the Higgs boson rapidity spectrum in Hj-MiNLO [54–56] to that of HNNLO [57], and the total cross-section is normalised to a prediction calculated at next-to-next-to-next-to-leading-order ($\mathrm{N^3LO}$) accuracy in QCD and has next-to-leading-order (NLO) electroweak (EW) corrections applied [29, 58–67].

Higgs boson production via VBF was simulated with Powheg Box v2 [68] using the PDF4LHC15nlo PDF set. The generation is accurate to NLO in QCD and the total cross-section is normalised to a calculation with full NLO QCD and EW corrections and approximate-NNLO QCD ones [69–71].

Higgs boson production via VH was simulated using Powheg Box v2 and the PDF4LHC15nlo PDF set. The generation has NLO accuracy in QCD for $q\bar{q}/qg \to VH$ events with up to one extra jet in the event, while the loop-induced $gg \to ZH$ process was generated separately at leading order in QCD. The two samples are normalised to cross-sections calculated at NNLO in QCD with NLO electroweak corrections for $q\bar{q}/qg \to VH$ and at NLO and next-to-leading-logarithm (NLL) accuracy in QCD for $gg \to ZH$ [72–78].

The production of $t\bar{t}H$ events was modelled using Powheg Box v2 [79, 80], while $tHqb$ and tWH events were generated using MadGraph5_aMC@NLO 2.6.0 and 2.6.2 [48], respectively. In these samples, the decays of bottom and charm hadrons were performed by EvtGen 1.6.0 [81]. Events in the tH samples originating from $t\bar{t}H$ production were removed using the diagram removal scheme [82, 83]. The cross-section used to normalise the $t\bar{t}H$ sample is calculated at NLO in QCD and electroweak couplings [29, 84–87], while those used to normalise the tH samples are calculated at NLO in QCD [83, 88].

Events from $b\bar{b}H$ production were generated with Powheg Box at NLO in QCD with the NNPDF3.0 PDF set [89]. The $b\bar{b}H$ sample contains additional NLO electroweak corrections, accounting for the treatment of the quark mass effects. The sample is normalised with the cross-section calculation obtained by matching the five-flavour scheme cross-section accurate to NNLO in QCD with the four-flavour scheme cross-section accurate to NLO in QCD [90–92], using the Santander scheme [92].

Additionally, alternative signal samples were generated in order to estimate uncertainties related to the modelling of the parton shower or of the matrix element and, in particular, of extra jet radiation in ggF. For the estimation of the uncertainties related to the modelling of the parton shower, for the ggF, VBF, VH, tH ($t\bar{t}H$) samples, the same events from the matrix element generator of the nominal signal samples were showered with Herwig 7.1.3 (Herwig 7.0.4) [93, 94] instead of Pythia, using the H7UE set of tuned parameters [94]. For the estimation of the uncertainties related to the matrix element calculation, alternative ggF, VH and $t\bar{t}H$ (VBF) samples were produced with MadGraph5_aMC@NLO interfaced to Pythia 8 (Herwig 7.1.3). The alternative ggF sample is at NLO QCD accuracy for zero, one and two additional partons merged using the FxFx merging scheme [95].

The generated Higgs boson events were passed through a Geant4 [96] simulation of the ATLAS detector [97] and reconstructed with the same software used for the data [35].

The main background originates from continuum diphoton production. Prompt diphoton MC events were generated with Sherpa 2.2 [98], using the NNPDF3.0nnlo PDF set and the dedicated set of tuned parton-shower parameters developed by the Sherpa authors. In this set-up, NLO-accurate matrix elements for up to one parton, and LO-accurate matrix elements for up to three partons were calculated with the Comix [99] and OpenLoops [100–102] libraries. They were matched with the Sherpa parton shower [103] using the MEPS@NLO prescription [104–107] with a dynamic merging cut [108] of 10 GeV. Photons were required to be isolated according to a smooth-cone isolation criterion [109]. Due to the large size of the non-resonant diphoton sample (around one billion generated events), needed for an accurate modelling of the background shape, these events were passed through a fast parametric simulation of the ATLAS detector response [97]. Smaller backgrounds from non-prompt photons are studied using control regions in data as described in the following.

The generation of the simulated event samples includes the effect of multiple pp interactions per bunch crossing, as well as the effect on the detector response due to interactions from bunch crossings before or after the one containing the hard interaction. Events in the simulation are weighted in order to reproduce the distribution of the number of interactions per bunch crossing observed in real collisions. In addition, simulated events are corrected to reflect the momentum scales and resolutions as well as the trigger, reconstruction, identification and isolation efficiencies measured in data for all the objects used in the analysis.

4 Event reconstruction and selection

This section describes how the events and the objects used in the analysis are reconstructed and selected. In addition to photons, these objects include jets, b-jets, leptons and missing transverse momentum since several fiducial regions and differential cross-sections are defined using these additional objects.

4.1 Photon reconstruction and identification

Photon candidates are reconstructed from dynamic, variable-size topological clusters of cells with significant energy in the EM calorimeter and from potentially matching tracks reconstructed in the inner detector [110]. The photon candidates are classified as converted if two tracks forming a conversion vertex, or one track with the signature of an electron track but without hits in the innermost pixel layer, are matched to the cluster; otherwise they are labelled as unconverted. Photon candidates are required to have pseudorapidity $|\eta| < 2.37$, excluding the transition region between the barrel and endcap calorimeter, $1.37 < |\eta| < 1.52$. In this acceptance region, the high granularity of the first sampling layer of the EM calorimeter allows efficient discrimination between isolated photons and closely spaced photon pairs from meson decays. The photon candidate energy is calibrated using the procedure described in Ref. [111].

Photon candidates are selected by an identification algorithm based on multiple shower-shape variables related to the energy deposited by the candidate in the calorimeters. Two working points of the identification algorithm are defined in order to reduce the contamination from the background, primarily associated with diphoton decays of neutral hadrons in jets [112]. The *loose* working point uses the lateral and longitudinal shape of the electromagnetic shower in the second layer of the calorimeter, together with the fraction of the shower's energy deposited in the hadronic calorimeter. The *tight* selection adds information from the finely segmented first sampling layer of the EM calorimeter, and imposes requirements tighter than those of the *loose* working point on shower shapes in other layers. The criteria are tuned separately for unconverted and converted photons in several pseudorapidity regions and as a function of the photon transverse energy E_T.

To further reject the hadronic jet background, photon candidates are required to be isolated from any significant activity in the calorimeter and tracking detector. A calorimeter-based isolation variable is defined as the sum of the transverse energy of positive-energy topological clusters contained within a cone of $\Delta R = 0.2$ around the photon candidate, after removing the transverse energy of the photon candidate. The pile-up and underlying-event contributions are removed by using an ambient energy correction computed from low-p_T jets in the events [113–117]. A track-based isolation observable is computed as the scalar sum of the transverse momenta of tracks within a $\Delta R = 0.2$ cone around the photon candidate. Tracks are required to have $p_T > 1$ GeV and to originate from the selected diphoton vertex, defined in Section 4.2. For converted photon candidates, the tracks associated with the conversion are not considered. Isolation requirements that scale with the transverse energy E_T of the candidate are applied to the selected photons. Photons are considered to be isolated if the calorimeter-based isolation is less than 6.5% of the photon E_T and if the track-based isolation is less than 5% of the photon E_T.

4.2 Event selection and identification of the diphoton primary vertex

An initial preselection retains events with at least two photon candidates with $E_T > 25$ GeV satisfying the *loose* identification criteria. Among all photon candidates passing this requirement, the two with the highest E_T values are retained for further analysis.

The primary vertex of the event is then selected from among all the reconstructed vertices, using a neural-network algorithm based on track and primary vertex information, as well as the directions of the two selected photons measured in the calorimeter and inner detector [118]. The algorithm was optimised to distinguish between hard vertices from gluon–gluon fusion signal events and ones from pile-up interactions. The direction of each photon candidate is recomputed with respect to the selected primary vertex, leading to an improvement of 11% in the diphoton invariant mass resolution in the inclusive case, computed with MC simulations. Agreement between data and simulation was checked with $Z \to ee$ events, using only the electrons' calorimeter energy clusters, and not their tracks, as input.

The event is finally selected if the leading- and subleading-E_T photon candidates have $E_T/m_{\gamma\gamma} > 0.35$ and 0.25, respectively, if they fulfil the *tight* identification criteria and the calorimetric and track-based isolation requirements, and if their invariant mass is in the range 105–160 GeV.

The number of selected events in the full Run 2 data set is 1 178 855. The reconstruction efficiency estimated from simulated $H \to \gamma\gamma$ events with respect to the full phase space is 36%. A shift in the simulated Higgs boson mass corresponding to the precision of the Higgs boson measurement has a negligible impact on the signal acceptance.

4.3 Reconstruction and selection of hadronic jets, leptons and missing transverse momentum

Jets, electrons and muons are also considered in events passing the diphoton selection described above. Hadronic τ-lepton decays are also reconstructed as jets.

Jet clustering uses the anti-k_t algorithm [119, 120] with a radius parameter $R = 0.4$. Differently from the previous analysis, the inputs come from a particle-flow algorithm which combines information from the tracker and the calorimeters [121]. The resulting jets exhibit improved energy and angular resolution, reconstruction efficiency, and pile-up stability compared to jets reconstructed using only the calorimeter information. Jets must satisfy $|y| < 4.4$ and $p_T > 30$ GeV. In order to suppress jets coming from pile-up interactions, a jet-vertex tagger (JVT) multivariate discriminant [122] is applied for jets within the tracking acceptance ($|\eta| < 2.5$) and $p_T < 60$ GeV.

Jets with $|\eta| < 2.5$ containing b-hadrons (b-jets) are identified using the DL1r b-tagging algorithm with the 70% efficiency working point [123].

Electron candidates are reconstructed by matching tracks in the inner detector with variable-size topological clusters of cells with significant energy in the EM calorimeter formed with the same algorithm as in the photon reconstruction. Tracks are required to be consistent with the diphoton vertex using their longitudinal (z_0) and transverse (d_0) impact parameters. In particular, tracks must satisfy $|z_0 \sin\theta| < 0.5$ mm and a transverse impact parameter significance $|d_0/\sigma(d_0)| < 5$, where θ is the track's angle with respect to the beam axis and $\sigma(d_0)$ is the uncertainty of d_0. In addition, electron candidates are selected using a likelihood-based identification method (*medium* working point) combining both track and calorimeter information and are required to satisfy isolation criteria based on the calorimeter and track information (*Fixed-cut loose* working point), detailed in Ref. [117]. Electron candidates are preselected by requiring $p_T > 10$ GeV and $|\eta| < 2.47$, excluding the transition region between the barrel and endcap sections of the EM calorimeter ($1.37 < |\eta| < 1.52$). In the measurement, only electrons with $p_T > 15$ GeV are considered.

Muon candidates are reconstructed by matching tracks from the MS and ID subsystems [124]. Muon candidates without an ID track but whose MS track is compatible with the interaction point, in the pseudorapidity range of $2.5 < |\eta| < 2.7$, are also considered. Muon tracks must satisfy $|z_0 \sin\theta| < 0.5$ mm and $|d_0/\sigma(d_0)| < 3$. Muon candidates are required to have $p_T > 15$ GeV and must satisfy *medium* identification requirements. Muons are also required to satisfy isolation criteria based on calorimeter and track information (*PflowLoose* working point), detailed in Ref. [124].

To avoid double-counting of reconstructed objects, an overlap removal procedure based on the angular distance $\Delta R_y = \sqrt{(\Delta y)^2 + (\Delta\phi)^2}$ is applied. First, electrons overlapping with the selected photons ($\Delta R_y < 0.4$) are removed. Next, jets overlapping with the selected photons ($\Delta R_y < 0.4$) and preselected electrons ($\Delta R_y < 0.2$) are removed. After that, electrons overlapping with the remaining jets ($\Delta R_y < 0.4$) are removed. Finally, muons overlapping with the selected photons or jets ($\Delta R_y < 0.4$) are removed.

The missing transverse momentum is computed as the negative vector sum of the transverse momenta of the selected photon, electron, muon and jet candidates, as well as the transverse momenta of remaining low-p_T particles, estimated using tracks associated with the diphoton primary vertex but not with any of the selected objects [125].

5 Fiducial phase space and differential observables

In this paper, inclusive and differential cross-sections are measured in various fiducial regions. As described in detail in Section 6, the $H \to \gamma\gamma$ signal is extracted in each fiducial region or bin of a differential distribution using a signal-plus-background fit to the corresponding diphoton invariant mass spectrum. The cross-sections are then computed from the signal yields, by correcting the signal yields for the effects of detector inefficiency and resolution, and accounting for the integrated luminosity of the data set.

Most of the measurements are performed in a baseline 'diphoton' fiducial region which closely matches the selection requirements of the reconstructed photons, described in Section 4.1, in order to minimise model-dependent acceptance extrapolations. The diphoton fiducial region is defined by the presence of two isolated photons in the final state with transverse momenta greater than 35% and 25% of the diphoton invariant mass, respectively. Each photon is required to have an absolute pseudorapidity $|\eta| < 1.37$ or $1.52 < |\eta| < 2.37$. The photons are required to be isolated in order to reduce hadronic activity, and the isolation energy must be less than 5% of the photon's transverse momentum. The isolation energy is defined as the scalar sum of the transverse momenta of stable charged particles (with a mean lifetime $c\tau > 10$ mm) with $p_T > 1$ GeV within a $\Delta R = 0.2$ cone around the photon direction. This isolation criterion is chosen so that it matches the detector isolation requirement in order to reduce model dependence that is introduced when assuming SM composition for response matrices built from the different Higgs boson production modes. The acceptance of the diphoton fiducial region with respect to the full phase space is 50% and the efficiency of the selection criteria described in Section 4 for signal events in the fiducial volume is close to 70%.

In addition, subsets of the diphoton baseline fiducial region are defined, providing a variety of phase-space regions sensitive to particular Higgs boson production modes. The definitions of these subregions, as well as of some of the observables for the differential measurements, are based on the following particle-level selections:

- **Leptons** are defined from all electrons and muons that are not produced during hadronisation. The prompt leptons are dressed by adding the four-momenta of stable photons within $\Delta R < 0.1$. Selected electrons (muons) are required to pass the kinematic selection of $p_{\mathrm{T}} > 15$ GeV and $|\eta| < 2.47$ ($|\eta| < 2.7$ for muons). Electrons are rejected if they pass through the barrel–endcap transition region $1.37 < |\eta| < 1.52$, or if their distance from a selected photon is $\Delta R < 0.4$. No isolation requirement is applied.
- **Jets** are defined by clustering all stable particles using the anti-k_t algorithm with a radius parameter $R = 0.4$. The clustering algorithm excludes prompt leptons and Higgs boson decay products. Selected jets are required to have transverse momentum $p_{\mathrm{T}} > 30$ GeV and rapidity $|y| < 4.4$. Selected jets are required to be well separated from photons with $p_{\mathrm{T}} > 15$ GeV ($\Delta R > 0.4$) and electrons ($\Delta R > 0.2$). Leading and sub-leading jets are defined as the ones with the largest and second-largest transverse momenta.
- ***b*-jets** are defined from selected central jets ($|\eta| < 2.5$) if there is a b-hadron with $p_{\mathrm{T}} > 5$ GeV within $\Delta R = 0.4$ of the jet axis.
- **Missing transverse momentum ($E_{\mathrm{T}}^{\mathrm{miss}}$)** is defined as the vector sum of the transverse momenta of all neutrinos that do not originate from the decay of a hadron.

The following fiducial subregions of the diphoton baseline region, with larger sensitivity to specific Higgs production modes, are defined:

- **VBF-enhanced**: a region composed of events with at least two jets, where the two leading jets have a large invariant mass, $m_{jj} \geq 600$ GeV, and large rapidity separation, $|\Delta y_{jj}| \geq 3.5$.
- **$N_{\mathrm{lepton}} \geq 1$**: a region composed of events containing at least one additional charged lepton (electron or muon) with transverse momentum $p_{\mathrm{T}}^{\ell} > 15$ GeV. This region is sensitive to the VH, $t\bar{t}H$ and tH production modes.
- **High $E_{\mathrm{T}}^{\mathrm{miss}}$**: a region composed of events with large missing transverse momentum ($E_{\mathrm{T}}^{\mathrm{miss}} > 80$ GeV) and a diphoton transverse momentum ($p_{\mathrm{T}}^{\gamma\gamma} > 80$ GeV). This region is sensitive to the VH and $t\bar{t}H$ production mechanisms and to BSM effects such as weakly interacting dark matter particles.
- **$t\bar{t}H$-enhanced**: a region composed of events with at least one b-jet and either no leptons and at least four jets, or at least one lepton and at least three jets. This region is mostly sensitive to $t\bar{t}H$, but also to tH production.

The acceptance of these fiducial regions varies between 0.2% for the High $E_{\mathrm{T}}^{\mathrm{miss}}$ region and 1.2% for the VBF-enhanced region. Figure 1 shows the expected contributions of signal events from the different SM Higgs boson production modes to the various fiducial regions. The fiducial regions are not orthogonal and non-negligible overlap exists between the $N_{\mathrm{lepton}} \geq 1$, High $E_{\mathrm{T}}^{\mathrm{miss}}$ and $t\bar{t}H$-enhanced regions. The largest overlap is between the first two, where 42% of the events in the High $E_{\mathrm{T}}^{\mathrm{miss}}$ fiducial region are also in the $N_{\mathrm{lepton}} \geq 1$ fiducial region.

Differential cross-sections are measured as a function of one or two of several observables in the diphoton fiducial region. In addition, a limited set of observables is studied in the VBF-enhanced fiducial region. The measured observables probe the Higgs boson kinematics and decay information, and also associated jet activity. The list of observables and a brief motivation for them is outlined below.

- Diphoton kinematic variables:

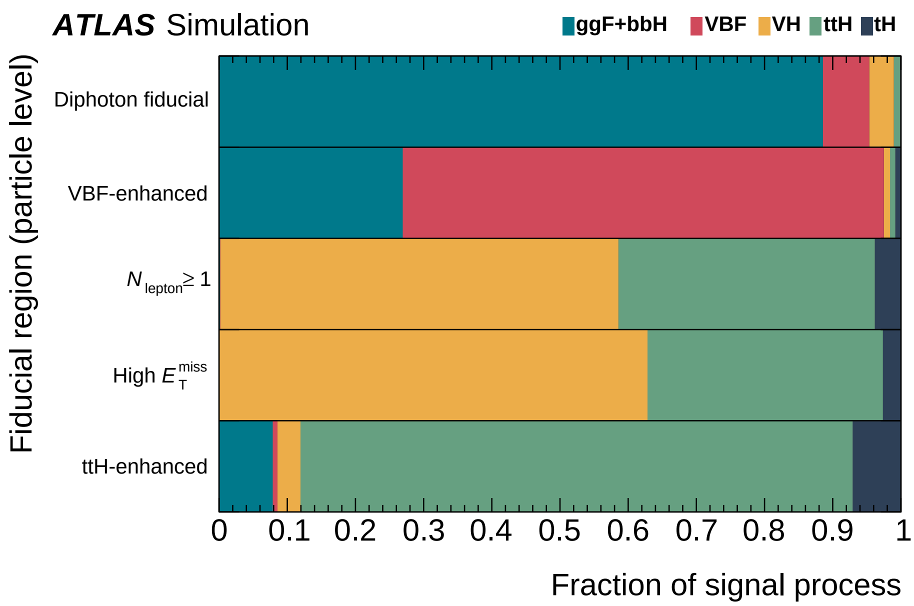

Figure 1: The expected production mode composition of Higgs boson events in each fiducial region at particle level, as estimated from simulated SM Higgs boson events with $m_H = 125.09$ GeV.

  - The transverse momentum $p_T^{\gamma\gamma}$ and the rapidity $|y_{\gamma\gamma}|$ of the diphoton system describe the fundamental kinematics of the Higgs boson. The low-p_T region of the Higgs boson is sensitive to the bottom- and charm-quark Yukawa couplings [126], and also to QCD resummation effects. The high-p_T region, on the other hand, is sensitive to the Higgs boson's coupling to the top quark, and to BSM scenarios where heavy resonances in the loops can further boost the Higgs boson [127–131]. The Higgs boson rapidity, $|y_{\gamma\gamma}|$, is sensitive to light-quark Yukawa couplings [132] in addition to the parton distribution functions (PDFs) of the colliding protons.
  - The relative transverse momenta of the leading and sub-leading photons, $p_T^{\gamma 1}/m_{\gamma\gamma}$ and $p_T^{\gamma 2}/m_{\gamma\gamma}$, probe the kinematics of the Higgs boson decay.

- Jet multiplicities:
  - The cross-sections as a function of the inclusive and exclusive jet multiplicities, N_{jets} (for jets with $p_T^j > 30$ GeV) are sensitive to the different Higgs boson production mechanisms and to QCD modelling of the gluon–gluon fusion production mode.
  - The cross-section as a function of the number of b-jets, $N_{b\text{-jets}}$, is sensitive to Higgs boson production in association with heavy-flavour particles. The measurement is carried out in the diphoton fiducial region requiring at least one central jet[2] with $p_T^j > 30$ GeV. In addition, in order to suppress the $t\bar{t}H$ contribution, a veto on electrons and muons is employed.

- $\geq$ 1-jet observables:

[2] Central jets are defined as having $|\eta| < 2.5$, matching the acceptance of the inner detector.

- The transverse momentum of the leading jet, $p_{\mathrm{T}}^{j_1}$, and of the scalar sum of the transverse momenta of all jets in the events, H_{T}, probe the perturbative QCD modelling and are sensitive to the relative contributions of the different Higgs production mechanisms.
- The transverse momentum $p_{\mathrm{T}}^{\gamma\gamma j}$ and the invariant mass $m_{\gamma\gamma j}$ of the system made by the two leading photons and the leading jet are sensitive to resummation effects.
- Beam-thrust-like variables $\tau_{C,j1}$ and $\Sigma\tau_{C,j}$, with $\tau_{C,j}$ for a given jet j being defined as:

$$\tau_{C,j} = \frac{m_{\mathrm{T}}}{2\cosh(y_j - y_{\gamma\gamma})}, \qquad m_{\mathrm{T}} = \sqrt{p_{\mathrm{T}}^2 + m^2},$$

  where m is the jet mass and y_j is the jet rapidity. The $\tau_{C,j1}$ observable is defined as the highest value of $\tau_{C,j}$ among all jets in the event, whereas $\Sigma\tau_{C,j}$ is the scalar sum of τ for all jets with $\tau > 5\,\mathrm{GeV}$. For large jet rapidities, τ corresponds to the small light-cone component of the jet, $p_j^+ = E_j - |p_{z,j}|$, whereas the sum corresponds to the beam-thrust global event-shape variable measured in the diphoton rest frame [133].

- The transverse momentum distribution of the diphoton system in events with a veto on the transverse momentum of the hardest accompanying jet, $p_{\mathrm{T}}^{\gamma\gamma,\,\text{jet veto}}$, provides insights into jet-veto resummation [134]. This cross-section is measured using different jet vetoes: $p_{\mathrm{T}}^{j} > 30,\ 40,\ 50,\ 60\,\mathrm{GeV}$.
- $\geq$ 2-jet observables:
  - The dijet invariant mass, m_{jj}, and the signed dijet azimuthal angle separation, $\Delta\phi_{jj}$, are sensitive to the VBF production mechanism. The sign of $\Delta\phi_{jj}$ is determined by ordering the jets in decreasing rapidity,[3] making this observable sensitive to the CP properties of the Higgs boson's couplings to gluons and weak vector bosons [135, 136]. The azimuthal angle between the dijet and diphoton systems, $\Delta\phi_{\gamma\gamma,jj}$, is sensitive to the VBF production mechanism and can be used to distinguish it from ggF events with at least two jets. Only the leading and sub-leading jets are considered.
  - The transverse momentum of the system made by the two leading photons and the two leading jets, $p_{\mathrm{T},\gamma\gamma jj}$, is sensitive to additional jet activity in the event.
- VBF-enriched phase space observables:

  Several fiducial differential cross-sections are measured in the VBF-enriched fiducial region as a function of observables sensitive to the kinematic features of the VBF production mode. These observables include: (i) the transverse momentum of the leading jet, $p_{\mathrm{T}}^{j_1}$; (ii) the signed dijet azimuthal angle separation, $\Delta\phi_{jj}$, which helps disentangle CP effects originating from gluon–gluon fusion and VBF; (iii) the pseudorapidity of the diphoton system relative to the average rapidity of the two leading jets, $|\eta^*|$, as its shape differs between ggF and VBF and hence can be used to disentangle the two production modes; (iv) the transverse momentum of the diphoton-plus-dijet system $p_{\mathrm{T},\gamma\gamma jj}$, which also helps to disentangle ggF and VBF, in addition to being sensitive to additional jet activity.

For each observable, the binning was designed to have an expected signal significance of close to or greater than 2σ and to minimise migrations of signal events between bins. The definition of the binning is summarised in Table 1.

[3] This definition of $\Delta\phi_{jj}$ is invariant under a redefinition of the ordering by choosing the opposite beam axis as detailed in Ref. [135]

Table 1: Bin ranges for the differential cross-section measurements. Transverse momenta, invariant masses and the H_T and τ variables (defined in the text) are given in GeV. For the jet multiplicities, the values reported in the table are the definition of the bins.

Variable	Bin Edges	N_{bins}
$p_T^{\gamma\gamma}$	0, 5, 10, 15, 20, 25, 30, 35, 45, 60, 80, 100, 120, 140, 170, 200, 250, 300, 450, 650, 13000	20
$\lvert y_{\gamma\gamma}\rvert$	0, 0.15, 0.3, 0.45, 0.6, 0.75, 0.9, 1.2, 1.6, 2.0, 2.5	10
$p_T^{\gamma 1}/m_{\gamma\gamma}$	0.35, 0.45, 0.5, 0.55, 0.6, 0.65, 0.75, 0.85, 0.95, 10	9
$p_T^{\gamma 2}/m_{\gamma\gamma}$	0.25, 0.35, 0.4, 0.45, 0.5, 0.55, 0.65, 0.75, 0.85, 10	9
N_{jets}	0, 1, 2, ≥3	4
$N_{b\text{-jets}}$	$N_{jets}^{central} = 0$ or $N_{lep} > 0$, $N_{b\text{-jets}} = 0$, ≥ 1	3
$p_T^{j_1}$	30, 60, 90, 120, 350, 13000	5
H_T	30, 60, 140, 200, 500, 13000	5
$p_T^{\gamma\gamma j}$	0, 30, 60, 120, 13000	4
$m_{\gamma\gamma j}$	120, 220, 300, 400, 600, 900, 13000	6
$\tau_{C,j1}$	0, 5, 15, 25, 40, 13000	5
$\sum \tau_{C,j}$	5, 15, 25, 40, 80, 13000	5
$p_T^{\gamma\gamma,\text{ jet veto 30 GeV}}$	0, 5, 10, 15, 20, 30, 40, 50, 100, 13000	9
$p_T^{\gamma\gamma,\text{ jet veto 40 GeV}}$	0, 5, 10, 15, 20, 30, 40, 50, 60, 100, 13000	10
$p_T^{\gamma\gamma,\text{ jet veto 50 GeV}}$	0, 5, 10, 15, 20, 30, 40, 50, 60, 70, 100, 13000	11
$p_T^{\gamma\gamma,\text{ jet veto 60 GeV}}$	0, 5, 10, 15, 20, 30, 40, 50, 60, 70, 80, 100, 13000	12
m_{jj}	0, 120, 450, 3000, 13000	4
$\Delta\phi_{jj}$	$-\pi, -\frac{\pi}{2}, 0, \frac{\pi}{2}, \pi$	4
$\pi - \lvert\Delta\phi_{\gamma\gamma,jj}\rvert$	0, 0.15, 0.65, π	3
$p_{T,\gamma\gamma jj}$	0, 30, 60, 120, 13000	4
VBF-enhanced: $p_T^{j_1}$	30, 120, 13000	2
VBF-enhanced: $\Delta\phi_{jj}$	$-\pi, -\frac{\pi}{2}, 0, \frac{\pi}{2}, \pi$	4
VBF-enhanced: $\lvert\eta^*\rvert$	0, 1, 2, 10	3
VBF-enhanced: $p_{T,\gamma\gamma jj}$	0, 30, 13000	2

Fiducial differential cross-sections are also measured in two-dimensional combinations of some of these observables, providing deeper insight into event kinematics and correlations across observables. The full list and the binning are summarised in Table 2.

6 Signal and background modelling of the diphoton mass spectrum

The Higgs boson signal yield is measured using an unbinned maximum-likelihood fit to the diphoton invariant mass spectrum in the fiducial regions and in each bin of the differential distributions. The fit is performed in the invariant mass range 105 GeV < $m_{\gamma\gamma}$ < 160 GeV. This range is chosen to be wide enough to allow a reliable determination of the background shape from the data, while being narrow enough to limit the uncertainties from the choice of background parameterisation. The fit model (detailed in Section 6.3) is the sum of the two analytic functions describing signal and background components. The signal and background shapes are modelled as described below.

Table 2: Binning for the double-differential cross-section measurements. Transverse momenta and τ variables (defined in the text) are given in GeV.

Variable	Bin Edges		N_{bins}
$p_{\text{T}}^{\gamma\gamma}$ vs $\lvert y_{\gamma\gamma}\rvert$	$0.0 < \lvert y_{\gamma\gamma}\rvert < 0.5$	$p_{\text{T}}^{\gamma\gamma}$: 0, 45, 120, 350	12
	$0.5 < \lvert y_{\gamma\gamma}\rvert < 1.0$	$p_{\text{T}}^{\gamma\gamma}$: 0, 45, 120, 350	
	$1.0 < \lvert y_{\gamma\gamma}\rvert < 1.5$	$p_{\text{T}}^{\gamma\gamma}$: 0, 45, 120, 350	
	$1.5 < \lvert y_{\gamma\gamma}\rvert < 2.5$	$p_{\text{T}}^{\gamma\gamma}$: 0, 45, 120, 350	
$(p_{\text{T}}^{\gamma 1} + p_{\text{T}}^{\gamma 2})/m_{\gamma\gamma}$ vs $(p_{\text{T}}^{\gamma 1} - p_{\text{T}}^{\gamma 2})/m_{\gamma\gamma}$	$0.6 < (p_{\text{T}}^{\gamma 1} + p_{\text{T}}^{\gamma 2})/m_{\gamma\gamma} \leq 0.8$	$(p_{\text{T}}^{\gamma 1} - p_{\text{T}}^{\gamma 2})/m_{\gamma\gamma}$: 0, 0.3	8
	$0.8 < (p_{\text{T}}^{\gamma 1} + p_{\text{T}}^{\gamma 2})/m_{\gamma\gamma} \leq 1.1$	$(p_{\text{T}}^{\gamma 1} - p_{\text{T}}^{\gamma 2})/m_{\gamma\gamma}$: 0, 0.05, 0.1, 0.2, 0.8	
	$1.1 < (p_{\text{T}}^{\gamma 1} + p_{\text{T}}^{\gamma 2})/m_{\gamma\gamma} \leq 4$	$(p_{\text{T}}^{\gamma 1} - p_{\text{T}}^{\gamma 2})/m_{\gamma\gamma}$: 0, 0.3, 0.6, 4	
$p_{\text{T}}^{\gamma\gamma}$ vs $p_{\text{T}}^{\gamma\gamma j}$	$N_{\text{jets}} = 0$	$p_{\text{T}}^{\gamma\gamma}$: 0, 350	9
	$0 < p_{\text{T}}^{\gamma\gamma j} \leq 30$	$p_{\text{T}}^{\gamma\gamma}$: 0, 100, 350	
	$30 < p_{\text{T}}^{\gamma\gamma j} \leq 60$	$p_{\text{T}}^{\gamma\gamma}$: 0, 45, 120, 350	
	$60 < p_{\text{T}}^{\gamma\gamma j} \leq 350$	$p_{\text{T}}^{\gamma\gamma}$: 0, 80, 250, 450	
$p_{\text{T}}^{\gamma\gamma}$ vs $\tau_{C,j1}$	$N_{\text{jets}} = 0$	$p_{\text{T}}^{\gamma\gamma}$: 0, 350	9
	$0 < \tau_{C,j1} \leq 15$	$p_{\text{T}}^{\gamma\gamma}$: 0, 100, 350	
	$15 < \tau_{C,j1} \leq 25$	$p_{\text{T}}^{\gamma\gamma}$: 0, 120, 350	
	$25 < \tau_{C,j1} \leq 40$	$p_{\text{T}}^{\gamma\gamma}$: 0, 200, 350	
	$40 < \tau_{C,j1} \leq 400$	$p_{\text{T}}^{\gamma\gamma}$: 0, 250, 650	
VBF-enhanced: $p_{\text{T}}^{j_1}$ vs $\Delta\phi_{jj}$	$-\pi < \Delta\phi_{jj} < 0$	$p_{\text{T}}^{j_1}$: 30, 120, 500	4
	$0 < \Delta\phi_{jj} < \pi$	$p_{\text{T}}^{j_1}$: 30, 120, 500	

6.1 Signal model

The Higgs boson signal manifests itself as a narrow peak in the $m_{\gamma\gamma}$ spectrum. The signal distribution is empirically modelled as a double-sided Crystal Ball function consisting of a Gaussian central part and a power-law tail on each side. The Gaussian core of the Crystal Ball function is parameterised by the peak position ($m_H + \Delta\mu_{\text{CB}}$) and width ($\sigma_{\text{CB}}$). The non-Gaussian contributions to the mass resolution arise mostly from photons converted to electrons with at least one electron losing a significant fraction of its energy through bremsstrahlung in the inner-detector material.

The parametric form of the double-sided Crystal Ball function can be found in Ref. [11]. The parameters of the model except its normalisation are determined through fits to the simulated signal samples, taking into account all production modes according to their expected contributions. To take into account the different values of the Higgs boson mass assumed in the analysis ($m_H = 125.09$ GeV) and in the MC event samples ($m_H = 125$ GeV), a shift of 90 MeV is applied to the position of the signal peak.

The parameterisation is derived separately for each bin considered in the cross-section measurement. As an example of the signal model, Figure 2 shows the parameterisations in the lowest and the highest $p_{\text{T}}^{\gamma\gamma}$ bin considered in the measurement. The $m_{\gamma\gamma}$ resolution for the signal is evaluated as half the width of the narrowest interval containing 68.3% of the distribution. In the inclusive case, it corresponds to 1.9 GeV. The resolution in the bins of the single-differential cross-sections ranges from a minimum of 1.0 GeV in the highest $p_{\text{T}}^{\gamma\gamma}$ bin, to 2.2 GeV in the bins corresponding to the diphoton rapidity region $1.2 < \lvert y_{\gamma\gamma}\rvert < 2.0$.

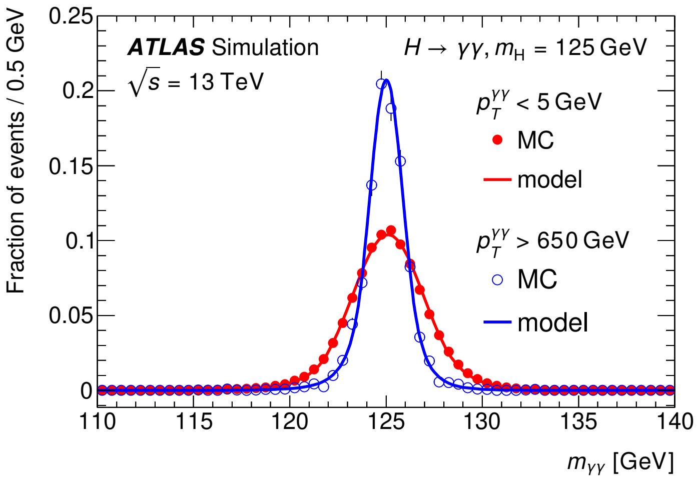

Figure 2: Signal $m_{\gamma\gamma}$ model in the lowest and highest $p_{\mathrm{T}}^{\gamma\gamma}$ bins considered. The two fitted models (solid curves) are compared with the $m_{\gamma\gamma}$ distributions of the signal MC events in the lowest (filled markers) and highest (open markers) $p_{\mathrm{T}}^{\gamma\gamma}$ bins. The resolution, evaluated as half the width of the narrowest interval containing 68.3% of the simulated events, varies between 1.0 GeV and 1.9 GeV.

6.2 Background model

The background in the Higgs boson signal extraction fit is modelled analytically. The functional form chosen for the background model is based on background templates built using simulations and data control-regions, and these are also used in the estimation of related systematic uncertainties. This section details the choice of background model.

The main sources of background are the non-resonant production of prompt and isolated diphotons ($\gamma\gamma$) and the γj and jj processes where one or two hadronic jets are misidentified as photons. For each bin of the analysis, the $m_{\gamma\gamma}$ distribution of the background falls smoothly and is described by an empirically chosen function. The parameters of these functions are fitted to data, but the functional forms are chosen from dedicated studies. The fraction contributed by each background component is measured in data using a two-dimensional double-sideband method [137] for each bin of a given observable. In this method, the identification and isolation requirements for the photons are loosened. The events are then separated into 16 orthogonal regions, depending on whether one or both photons satisfy or fail the nominal identification and/or isolation requirements as described in Section 4.1. The $\gamma\gamma$, γj and jj yields after the nominal selection are obtained by solving a system of equations using the observed yields in the 16 regions and the photon efficiencies estimated from MC simulation as inputs. The systematic uncertainties in the measured background fractions are due to the definition of the control regions arising from the different inverted photon identification and isolation criteria, resulting in a systematic uncertainty that dominates the total uncertainty. The fractions contributed by the $\gamma\gamma$, γj and jj background sources after the inclusive diphoton selection are $(75 \pm 4)\%$, $(22 \pm 3)\%$ and $(3 \pm 1)\%$, respectively. The $\gamma\gamma$ fraction changes smoothly across the bins of the differential measurements and ranges from 66% to 92%.

To study the modelling of the background, a background template of the diphoton invariant mass is built as the sum of the $\gamma\gamma$ and the γj components. Adding the jj component or the contribution due to cases where the two photons originate from two different pile-up interactions was found to have a negligible impact on the results. For each bin, the background template is built by summing the two considered components according to the relative fractions measured with data. The $\gamma\gamma$ template is a histogram determined from the events of the simulation described in Section 3 that pass the full event selection. The template of the reducible γj component is obtained from data in control regions formed by inverting the tight photon identification requirement, while still imposing the loose identification requirement, on any of the two photons in the final state. The total background template is then normalised to match the data entries in the mass sidebands (i.e. excluding the range $123\,\text{GeV} < m_{\gamma\gamma} < 127\,\text{GeV}$).

Several functional forms were considered for the modelling of the background template distributions, including an exponential function of a polynomial of first to fourth order, a power law of first or second order, and a Bernstein polynomial of third, fourth or fifth order. The choice of functional form for the background modelling is based on the estimated potential bias in the fitted signal yield (spurious signal) and the goodness of the fit. Both criteria are evaluated using the background template. The spurious signal is estimated as the maximum of the absolute value of the fitted signal yield in successive fits to background templates, using a signal model with resonant mass scanning the range between 123 GeV and 127 GeV. The spurious signal must be less than 20% of the background uncertainty or less than 10% of the expected signal yield. In addition, the goodness of the fit of the functional form to the background template is evaluated with a χ^2 test and the relative p-value is required to be larger than 1%. If more than one function fulfils the criteria, the one with fewer degrees of freedom is chosen. The value of the spurious signal is considered as a systematic uncertainty of the signal yield due to the background modelling.

Due to the finite size of the simulation samples used to build the background templates, large statistical fluctuations are often observed. These fluctuations can adversely affect the estimation of the spurious signal, particularly when they occur in the Higgs signal window between 123 GeV and 127 GeV. These fluctuations would nominally be interpreted as a spurious signal, hence resulting in an overestimation of the background model's systematic uncertainty. Given the computational limitations in generating larger data sets, an alternative approach is employed. The background templates are smoothed using Gaussian process regression (GPR) [138], using the Gibbs Kernel. The GPR approach suppresses statistical fluctuations in the background templates, without biasing the shape of wider features in the template. The GPR approach was validated using pseudo-experiments in which sets of pseudo-data, with different statistics, were generated from known functions, using the functional forms considered to model the background distribution, and the bias from the GPR smoothing was tested. The pseudo-experiments show that the smoothing procedure maintains the underlying shape of the $m_{\gamma\gamma}$ distribution, hence introducing no significant bias in the spurious signal. Overall, use of the GPR approach resulted in an average reduction of the spurious signal by 30%, with the largest improvements seen in the low-yield bins, and little to no change seen in high-yield bins. This is expected given the statistical fluctuations in the low-yield templates, and hence GPR provides an accurate estimate of the spurious signal that is due to real shape mis-modelling. This is in contrast to the high-yield templates, where the spurious-signal estimates from the GPR-smoothed template and the original template are compatible.

The selected background functions are further validated in the $m_{\gamma\gamma}$ data sideband regions by means of likelihood-ratio tests that check the hypothesis that a function with an additional degree of freedom is not needed to better describe the distribution. The following test statistic is computed:

$$\lambda_{1,2} = -2\log(L_1/L_2),$$

where L_1 and L_2 are the likelihood with the nominal background model and an alternative one with an additional degree of freedom, respectively. The function with the extra degree of freedom is chosen if the probability of obtaining a $\lambda_{1,2}$ value higher than the observed one computed under the nominal-background hypothesis, $P(\lambda_{1,2} \geq \lambda_{1,2}^{\text{obs}})$, is less or equal to 0.05. The procedure is then repeated with higher degrees of freedom until $P(\lambda_{1,2} \geq \lambda_{1,2}^{\text{obs}})$ exceeds 0.05. Overall, approximately 6% of the total number of different differential observable bins and fiducial regions considered for the measurement required an increase of the number of degrees of freedom of the background model by one unit.

6.3 Measurement procedure

Reconstructed events passing the event selection are assigned to one of several different bins, each corresponding to a fiducial bin to be measured, called reco-bins. The classification is performed using reconstructed quantities following the same definition as at particle level. When measuring the cross-section for the fiducial regions which are subsets of the diphoton region, an additional reco-bin is filled with events passing the diphoton selection but failing the full selection corresponding to that region in order to help the fit constrain systematic uncertainties. For example, when measuring the cross-section in the VBF-enhanced fiducial region, an additional reco-bin named 'anti-VBF', filled with events passing the analysis selection but not passing the definition of the VBF region at detector level, is added. Similarly, for the differential cross-sections involving the presence of at least one or at least two jets, one or two additional reco-bins are filled with events passing the selection with zero jets or exactly one jet. In addition, when applicable, underflow and overflow reco-bins are considered.

Differently from the previous analysis [11], the measurement of the fiducial cross-section as a function of a certain particle-level observable is performed in a single step through a simultaneous fit of the $m_{\gamma\gamma}$ distribution in all the reco-bins for the corresponding detector-level observable. For each reco-bin r, the number of selected events originating from Higgs boson diphoton decays $N_r^{(H)}$ is parameterised as a function of the cross-sections under study through the response matrix R:

$$N_r^{(H)} = \frac{1}{C_r^{\text{fid}}} \left[\sum_t L \times (\sigma_t \times B_{\gamma\gamma}) \times R_{t,r} \right], \qquad (1)$$

where the sum inside the square brackets represents the number of fiducial signal events reconstructed in the reco-bin r. In this formula, L is the integrated luminosity, and $(\sigma_t \times B_{\gamma\gamma})$ is the fiducial Higgs boson production cross-section in the 'truth'-bin t times the Higgs boson diphoton branching ratio, where 'truth' refers to information from the MC generator's event record. The matrix element $R_{t,r}$ of the response matrix describes the probability to reconstruct a signal event originating from a particle-level truth-bin t in a reconstructed detector-level reco-bin r. As a consequence of carefully choosing the binning of the observables under study to minimise migrations between bins, the response matrices for all the variables considered are well-conditioned, with a condition number[4] that ranges from 1.1 for quantities with very small migrations, such as $|y_{\gamma\gamma}|$, to 2.1 for quantities involving jets for which the migrations are larger. As an example, Figure 3 shows the response matrices for $p_{\text{T}}^{\gamma\gamma}$ and N_{jets}. The slightly decreasing values of the diagonal elements of the $p_{\text{T}}^{\gamma\gamma}$ response matrix up to $p_{\text{T}}^{\gamma\gamma} = 45$ GeV reflects the dependence of the photon identification efficiency on the single-photon E_{T} [112]. The factor C_r^{fid} is equal to the fraction of selected events in the signal simulation that originate from events within the fiducial volume. It is in general close to one, and corrects for events that pass the selection but are outside of the fiducial region. It also removes a small fraction (around 0.4%) of reconstructed $H \rightarrow f\bar{f}\gamma$ Dalitz decays, where f is any fermion except a top quark, that are present in the MC samples showered with Pythia 8. For example, the value for the

[4] The condition number of a matrix is defined as the ratio of the maximum and minimum singular values of the matrix itself. In the case of a response matrix, the condition number is related to how much an unfolding procedure relying on such a matrix is sensitive to statistical fluctuations in the input.

diphoton inclusive fiducial cross-section C_r^{fid} is 98%. This correction factor and the response matrix are estimated from the SM Higgs boson Monte Carlo simulations taking into account all the production modes and their SM cross-sections.

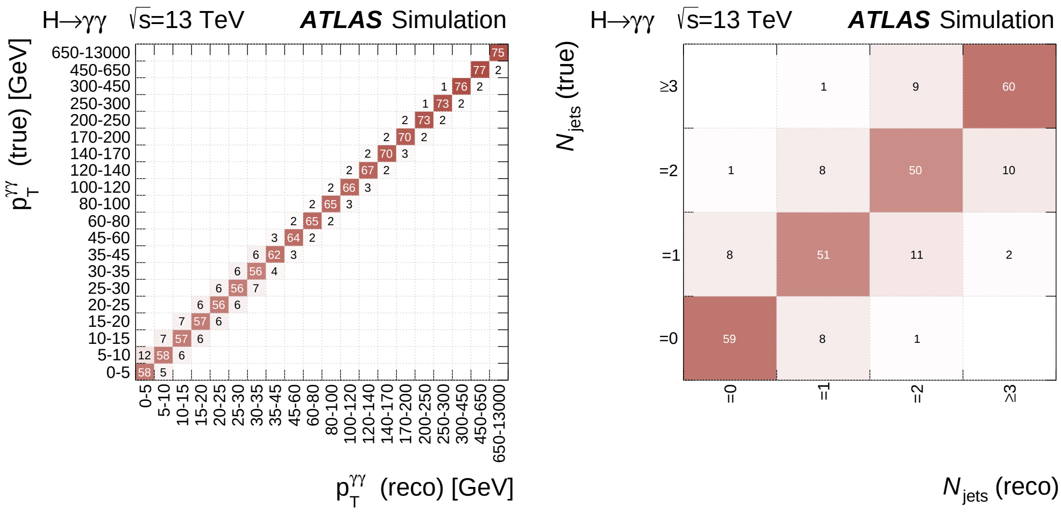

(a) (b)

Figure 3: Response matrices (in %) evaluated from MC simulations of Higgs bosons decaying into two photons for (a) the transverse momentum of the diphoton system $p_{\text{T}}^{\gamma\gamma}$ and (b) the number of jets N_{jets}. Each matrix element is the probability for a signal event generated in a fiducial truth-bin to be selected in a reconstructed reco-bin. Values smaller than 1% (after rounding) are not shown.

For each reco-bin, the $m_{\gamma\gamma}$ distribution is modelled as a mixture of the signal model and the background model taking into account their yields. The yield of the background, as well as its shape parameters, are free in the fit and uncorrelated among the reco-bins. The measurement of $(\sigma_t \times B_{\gamma\gamma})$ is performed with a simultaneous maximum-likelihood fit of all the reco-bins of a given observable.

Systematic uncertainties, described in Section 7, are incorporated into the likelihood as nuisance parameters, each one constrained by a probability density function. Gaussian constraints are used for the peak position of the signal model and for the spurious-signal uncertainty. Log-normal constraints are used for the uncertainties related to the yield and for the signal mass resolution.

7 Systematic uncertainties

The measurements presented in the paper are affected by several systematic uncertainties. Most of the uncertainties fall in one of the following categories and are described in the sections below: (i) uncertainties affecting the modelling of the signal and background shapes, and (ii) experimental and theoretical uncertainties affecting the response matrices. Two additional uncertainties affecting the measured cross-sections are those in the luminosity L of the analysed data set (which enters Eq. (1) directly) and the branching ratio of the Higgs boson Dalitz decays (which enters Eq. (1) through the correction factor C_r^{fid}).

The uncertainty in the combined 2015–2018 integrated luminosity is 1.7%. It is derived from the calibration of the luminosity scale using x–y beam-separation scans, following a methodology similar to that detailed in Ref. [139], and using the LUCID-2 detector for the baseline luminosity measurements [140].

Some of the Higgs boson Dalitz decays pass the analysis selection and the yields have to be corrected to subtract this contribution as explained in the previous section. Since the branching ratio of Higgs boson Dalitz decay is poorly known [141], a 100% uncertainty is assigned to the Dalitz contribution; this results in a small uncertainty corresponding to about 0.4% of the measured cross-section in the fiducial inclusive region.

7.1 Systematic uncertainties in the signal and background $m_{\gamma\gamma}$ models

As described in Section 6, the Higgs boson cross-sections are estimated from a fit to the diphoton invariant mass spectrum. Therefore, the cross-sections are affected by uncertainties in the signal $m_{\gamma\gamma}$ model introduced by photon energy scale and resolution uncertainties, as well as by uncertainties in the background model related to choosing a particular analytic function to represent it.

The photon energy scale uncertainties shift the peak position, whereas the photon energy resolution uncertainties affect the signal width, broadening or narrowing it. These systematic uncertainties are estimated from $Z \to ee$ decays as detailed in Ref. [117]. Photon energy resolution uncertainties dominate the Higgs boson signal shape uncertainties, and typically change the width of the signal distribution by between 5% and 27%. These uncertainties increase with p_{T} of the individual photons and the impact on the final measurement reaches 16% at $p_{\mathrm{T}}^{\gamma\gamma} > 650$ GeV. The photon energy scale uncertainties, on the other hand, have a smaller impact, varying the peak position by between 0.2% and 0.5%. An additional systematic uncertainty in the peak position is included to account for the uncertainty (0.24 GeV) in the Higgs boson mass [10].

As detailed in Section 6.2, choosing an analytic function to model the background diphoton invariant mass distribution in the fit can cause deviations of the true background distribution from the nominal model to be identified as a spurious signal. The spurious signal estimated from fits to the background $m_{\gamma\gamma}$ templates is assigned as the systematic uncertainty in the signal yield originating from the choice of background model. In the likelihood it is implemented as an additional signal component in each reco-bin. The uncertainty is considered to be uncorrelated between different reco-bins.

7.2 Experimental and theoretical uncertainties affecting the response matrices

Experimental uncertainties The response matrices R are affected by different experimental uncertainties in the calibration and identification of photons, jets, and leptons. They can change the total signal yield, migrations across reco-bins, and migrations into and out of the fiducial acceptance:

- **Diphoton trigger efficiency** The efficiency of the diphoton trigger is estimated using the bootstrap method [34] in data and simulation, with an uncertainty close to 1.0%.
- **Vertex selection efficiency** This uncertainty reflects the difference in the selection of the primary vertex using the neural network algorithm between data and the simulation. This uncertainty is estimated using $Z \to e^+e^-$ events after removing the electron tracks. The resulting uncertainty is found to be <0.3%.

- **Photon identification efficiency** This uncertainty is evaluated by varying the efficiency scale factors between data and the simulation, measured using three data-driven techniques as detailed in Ref. [117], within their uncertainties. This uncertainty is estimated to be 1.8% for the inclusive fiducial region, and decreases to 1% with increasing $p_{\mathrm{T}}^{\gamma\gamma}$ as the uncertainties of the single-photon scale factors decrease.

- **Photon isolation efficiency** Similarly to the photon identification efficiency, this uncertainty is evaluated by varying the track and calorimeter isolation scale factors within their uncertainties as detailed in Ref. [117]. This amounts to an uncertainty of 1.6% for the inclusive fiducial region, and varies as function of $p_{\mathrm{T}}^{\gamma\gamma}$, increasing to 2% for the very high $p_{\mathrm{T}}^{\gamma\gamma}$ region.

- **Photon energy scale and resolution** In addition to affecting the signal invariant mass distribution, as detailed in Section 7.1, the photon energy scale and resolution uncertainties also have an effect on the response matrices which results from migrations across bin boundaries and across the boundaries of the fiducial region. The magnitude of this uncertainty is at the per-mille level, reaching 0.2% for the highest $p_{\mathrm{T}}^{\gamma\gamma}$ bins.

- **Modelling of pile-up in the simulation** This uncertainty is derived by varying the average number of interactions per bunch crossing, $\langle\mu\rangle$, in the simulation by an amount consistent with data. This yields an uncertainty of 1.5% for the inclusive fiducial region, and increases with p_{T} and jet activity to 6% for the highest jet multiplicity.

- **Jet energy calibration and jet selection** These uncertainties affect only jet-related measurements. Jet energy calibration uncertainties reflect the remaining differences in the jet energy scale and resolution between data and the simulation as estimated through the p_{T}-balance technique in Z+jets, γ+jet, and dijet events, as detailed in Ref. [142]. Jet selection uncertainties are related to the efficiency of both the jet-vertex tagger and the forward jet-vertex tagger used at higher $|\eta|$. The typical size of the jet-related uncertainties ranges from 5% for topologies with low jet multiplicities to 24% for the highest jet multiplicities.

- **Lepton uncertainties** Lepton uncertainties account for the uncertainties in the reconstruction, identification and isolation efficiencies of electrons [117] and muons [124]. They are obtained from dilepton decays of Z bosons and J/ψ mesons collected in Run 2, using a tag-and-probe technique. The typical size of these uncertainties is about 0.6% for electrons and about 0.5% for muons, and their effect is significant only for the cross-section measurement in the lepton-enhanced fiducial region.

- **$E_{\mathrm{T}}^{\mathrm{miss}}$ uncertainties** Uncertainties related to the reconstruction and calibration of missing transverse momentum are estimated by propagating uncertainties associated with the energy scales and resolutions of photons, jets and leptons in addition to uncertainties from unassociated charged-particle tracks. This results in a cross-section measurement uncertainty of 13% in the High $E_{\mathrm{T}}^{\mathrm{miss}}$ fiducial region.

- ***b*-tagging uncertainties** These uncertainties are associated with the efficiency of the b-tagging algorithm and affect only measurements where b-tagging is required. They correspond to a maximum uncertainty of 4% for the highest $N_{b\text{-jets}}$ bin. They are determined for jets containing the decay of a b-quark, using $t\bar{t}$ events in 13 TeV data and the method outlined in Ref. [143].

Theoretical uncertainties In addition to the previous experimental uncertainties, the following theoretical uncertainties affect the response matrices:

- **Signal composition uncertainty** The response matrices used in the fit to account for detector effects in each distribution are built considering all the production modes of the Higgs boson. The simulated samples are then combined assuming SM cross-sections, and hence model dependence can be introduced if the matrices vary significantly between production modes. Therefore, a modelling uncertainty is estimated by varying the cross-section of each production mode within its measured uncertainty [144]. The resulting uncertainties are quite small, reaching at most 1% for the highest jet multiplicities.
- **Modelling of the matrix element generator** This uncertainty results from the bias estimated by using an alternative matrix element generator (MadGraph5_aMC@NLO) and using it to unfold the predictions from the nominal matrix element generator (Powheg Box). Both matrix element generators are interfaced with the Pythia 8 parton shower. The response matrices are built using all production modes. The relative difference between the two response matrices is then included in the fit likelihood as a nuisance parameter, resulting in a small uncertainty (1%–2%) in the cross-sections for the high-p_{T} regions and the highest jet multiplicities. In addition, a robustness check was performed by reweighting the default simulation using the EFT model that gives the largest variation (see Section 9.2 for more details), and using the nominal response matrix. This check resulted in negligible non-closure at the level of at most 0.5%.
- **Modelling of the parton shower, underlying event, and hadronisation** This uncertainty arises from the relative change in the response matrices when switching the parton showering algorithm from Pythia 8 to Herwig 7. These uncertainties are typically small, reaching 1.6% for the highest jet multiplicities.

Uncertainties in the response matrix due to the scale or PDF variations are negligible and not considered further. For the total cross-section in the full phase space, an additional uncertainty of 2.9% in the $H \to \gamma\gamma$ branching ratio is included in the measurement.

8 Cross-section results and comparison with theoretical predictions

This section presents the measured fiducial inclusive cross-sections and a subset of the differential cross-sections described in Section 5, following the fit procedure detailed in Section 6.3. The measurements are compared with one or more theoretical predictions, which are described in Section 8.1.

8.1 Theoretical predictions

The measured cross-sections are compared with several theoretical predictions described below, the nominal one being that from the fully simulated MC samples scaled to their latest cross-section calculations, called 'default simulation' in the following. The difference between the nominal prediction and other predictions, except the proVBF predictions used for comparison with the VBF observables, is only in the calculation of the ggF component. The alternative predictions were either provided by their corresponding authors or calculated by using their tools and the set-up recommended by the authors themselves. For the inclusive parton-level predictions, acceptance corrections derived from the default simulation are applied.

Default simulation The default simulated signal samples described in Section 3 are used for the different processes. The uncertainties in the predictions are computed as follows:

- Uncertainties from the choice of the PDF set and α_s are evaluated using the PDF4LHC15 error PDF set, which takes into account 30 variations of NNLO (ggF) or NLO (other modes) PDFs and two variations of α_s, following the PDF4LHC recommendations [47]. The PDF uncertainties are treated as fully correlated across production modes, given that the eigen-variations are completely independent of the physics process.
- Perturbative uncertainties for ggF, VBF, VH, $t\bar{t}H$ are estimated bin-by-bin using the simplified template cross-sections (STXS) stage 1.2 uncertainty scheme [29]. The scheme includes various normalisation and migration uncertainties in fine binning corresponding to the STXS 1.2 granularity. For ggF, the scheme defines 18 sources of uncertainty, which are added in quadrature: two accounting for yield uncertainties related to the total cross-section, two for migration uncertainties related to splitting the phase space by jet multiplicity, one accounting for the treatment of m_t, and the remaining sources account for migrations across the different STXS bin boundaries defined as a function of various observables including the Higgs boson transverse momentum, the Higgs-plus-jet transverse momentum and the dijet invariant mass. The same scheme is also defined for $gg \to ZH$. For the other production modes, a similar set of nuisance parameters accounting for migrations across the different STXS 1.2 bins is used. For $b\bar{b}H$ and tH production modes, the perturbative uncertainties are estimated as an envelope of the scale variations available in Powheg Box.
- The Higgs to diphoton branching ratio uncertainty from Ref. [29] is also included.

In addition to the default simulation, several theory predictions for the various measured cross-sections are compared with data. A summary of the uncertainties in the new predictions is reported in Appendix C. An overview of the different predictions is given below:

MATRIX+RadISH The MATRIX+RadISH interface [145] combines fully differential cross-sections at NNLO accuracy in QCD through MATRIX [146, 147] with all-order resummation through RadISH [148, 149] for various $2 \to 1$ and $2 \to 2$ colour-singlet production processes. MATRIX+RadISH is used to perform the double-differential resummation of the transverse momentum of the colour singlet and of the leading jet at next-to-next-to-leading-logarithm (NNLL) accuracy [134].

RadISH+NNLOjet A prediction for the transverse momentum distribution of the Higgs boson decay products with fiducial cuts has been calculated within the RadISH framework [148, 149], matched to the Higgs + ≥ 1-jet NNLO-accurate QCD calculation at large Higgs boson p_{T} from NNLOjet [150, 151]. The $\mathrm{N^3LL'}$ calculation includes a resummation correction of linear fiducial power terms at the same accuracy with respect to $\mathrm{N^3LL}$ accuracy [152, 153].

Sherpa+MCFM+OpenLoops Sherpa [98] predictions were produced using version 2.2.11. The predictions are accurate to NLO in QCD for Higgs + ≥ 0, ≥ 1, ≥ 2, ≥ 3 jets, with the fourth jet being accurate to leading order (LO) in QCD and subsequent jets produced by the parton shower (with leading-logarithmic accuracy). The Higgs + ≥ 2-jets matrix elements were produced using MCFM [154], and Higgs + ≥ 3-jets matrix elements were calculated using the OpenLoops [100–102] libraries. They are matched with the Sherpa parton shower [103] using the MEPS@NLO prescription [104–107].

Sherpa 2.2.11 uses an improved parton clustering procedure resulting in a reduction in the predicted cross-sections and a reduction in the uncertainties in phase-space regions with multiple jets.

ResBos2 ResBos2 [155, 156] provides predictions for inclusive Higgs production via gluon–gluon fusion calculated at N^3LL+NNLO accuracy [156, 157]. For inclusive Higgs-plus-jet production, the ResBos2 program uses the transverse-momentum-dependent (TMD) resummation formalism as proposed in the Collins 2011 scheme [158]. The prediction is made to NLL+NLO accuracy and matched to the NLO calculation [159]. The jet-veto results for the ResBos2 code are taken as the difference between the inclusive Higgs and Higgs-plus-jet results.

SCETlib::qT Predictions were obtained using the SCETlib::qT module [160–164] including the resummation of logarithms at small $p_{\mathrm{T}} < m_H$ for the usual leading-power in p_{T}/m_H contributions as well as all fiducial power corrections (induced by the fiducial cuts) [162]. SCETlib resummation achieves N^3LL' accuracy, including the complete three-loop corrections in the small-p_{T} limit [163, 165, 166]. For other photonic observables, the required corrections for matching to N^3LO are not available, so they are computed at N^3LL+NNLO accuracy in QCD. Only the dominant top-quark loop contributions are included in the predictions for the differential fiducial cross-sections.

SCETlib::pTj1 The predictions for $p_{\mathrm{T}}^{j_1}$ are obtained using the SCETlib::pTjet module [160, 167, 168]. The predictions are for $gg \to H$ in the narrow-width limit with $m_H = 125.09$ GeV. The $p_{\mathrm{T}}^{j_1}$ spectrum is computed to NNLL′+NNLO accuracy for the dominant top-quark Yukawa coupling y_t^2 contribution in the rescaled EFT limit [167].

SCET+MG5 (NNLL′+NNLO) The predictions are obtained for the 0-jet ggF cross-section using the rapidity-dependent jet veto observable $\tau_{C,j1}$ at NNLL′+NNLO accuracy [169]. The predictions are obtained with a resummation of $p_{\mathrm{T}}^{j_1}/m_H$ with NNLL′ accuracy.

STWZ, BLPTW The perturbative STWZ, BLPTW predictions [167, 170] include NNLL′+NNLO resummation in QCD for the p_{T} of the leading jet , combined with a NLL′+NLO resummation in QCD for the subleading jet. The numerical predictions for $\sqrt{s} = 13$ TeV are taken from Ref. [29]. This prediction is shown for the inclusive zero-, one- and two-jet cross-sections as well as for the exclusive zero- and one-jet cross-sections.

proVBF NNLO The proVBF [171] program calculates the fully differential NNLO corrections to vector-boson fusion Higgs boson production. This is achieved with a ‘projection-to-Born’ method that combines an inclusive NNLO calculation in the structure-function approach with a suitably factorised NLO VBF Higgs plus 3-jet calculation.

GoSam GoSam [172, 173] provides the fixed-order loop contributions accurate at NLO in QCD in the inclusive Higgs + 0, 1, 2, 3 jets regions. The real-emission contributions at fixed order in QCD are provided by Sherpa [98].

8.2 Inclusive fiducial cross-section measurements

The observed $m_{\gamma\gamma}$ distribution in data for the photons passing the selection is shown in Figure 4. The figure also shows the signal-plus-background (S+B) fit of the data with the model described in Section 6 for the measurement of the cross-section in the diphoton fiducial region. Similarly, Figure 5 shows the $m_{\gamma\gamma}$ distribution and the corresponding S+B fit for the events passing the requirements corresponding to the other fiducial regions.

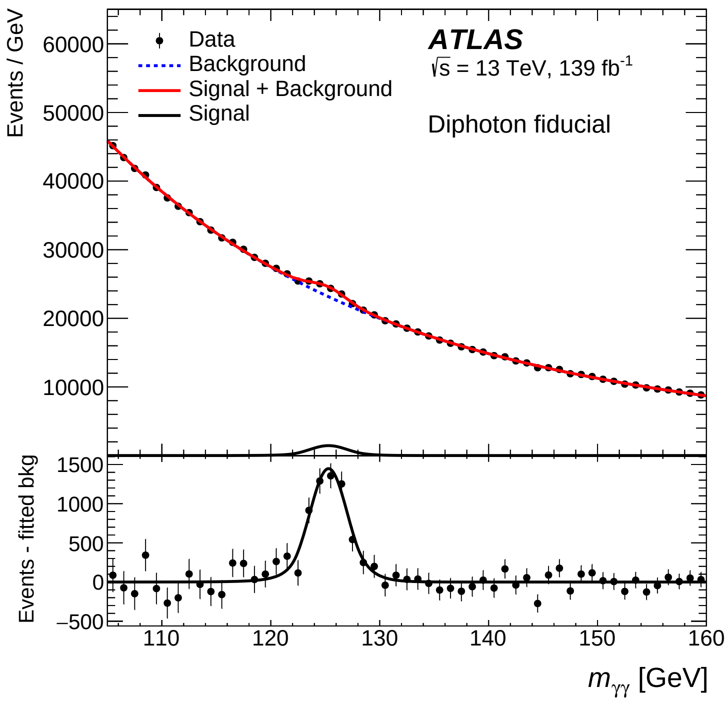

Figure 4: The diphoton invariant mass spectrum of events passing the selection. The solid red curve shows the fitted signal-plus-background model with the Higgs boson mass constrained to 125.09 ± 0.24 GeV. The bottom pad shows the residuals between the data and the background component of the fitted model.

The measured particle-level cross-sections of the $pp \to H \to \gamma\gamma$ process in the fiducial regions defined in Section 5 are summarised in Table 3 and in Figure 6. Upper limits at 95% confidence level (CL) were set on fiducial cross-sections with observed significance below 3σ, using the $\mathrm{CL_s}$ procedure [174]. The cross-section in the inclusive fiducial region is also compared with SCETLIB::qT predictions, where the efficiency of the particle-level photon isolation requirement (98%) is corrected for using the default simulation. SCETLIB::qT directly accounts for the photon kinematic acceptance and relevant resummation corrections, resulting in the most accurate prediction of the cross-section of 64.2 ± 3.4 fb [161], compared to a measured fiducial cross-section of σ_{fid} = 67 ± 5 (stat.) ± 4 (sys.) fb = 67 ± 6 fb.

The total cross-section times branching ratio in the full phase space is also reported. It was computed in the same way as the fiducial cross-sections, from the fit to the inclusive sample of all the selected candidates. In the fit, the full acceptances from the full phase space to the selected one are used to replace those from the fiducial ones. Taking into account the Higgs diphoton branching ratio, the measured total Higgs boson production cross-section is σ_{tot} = 58 ± 4 (stat.) ± 4 (sys.) pb = 58 ± 6 pb compared to the SM prediction of 55.6 ± 2.7 pb.

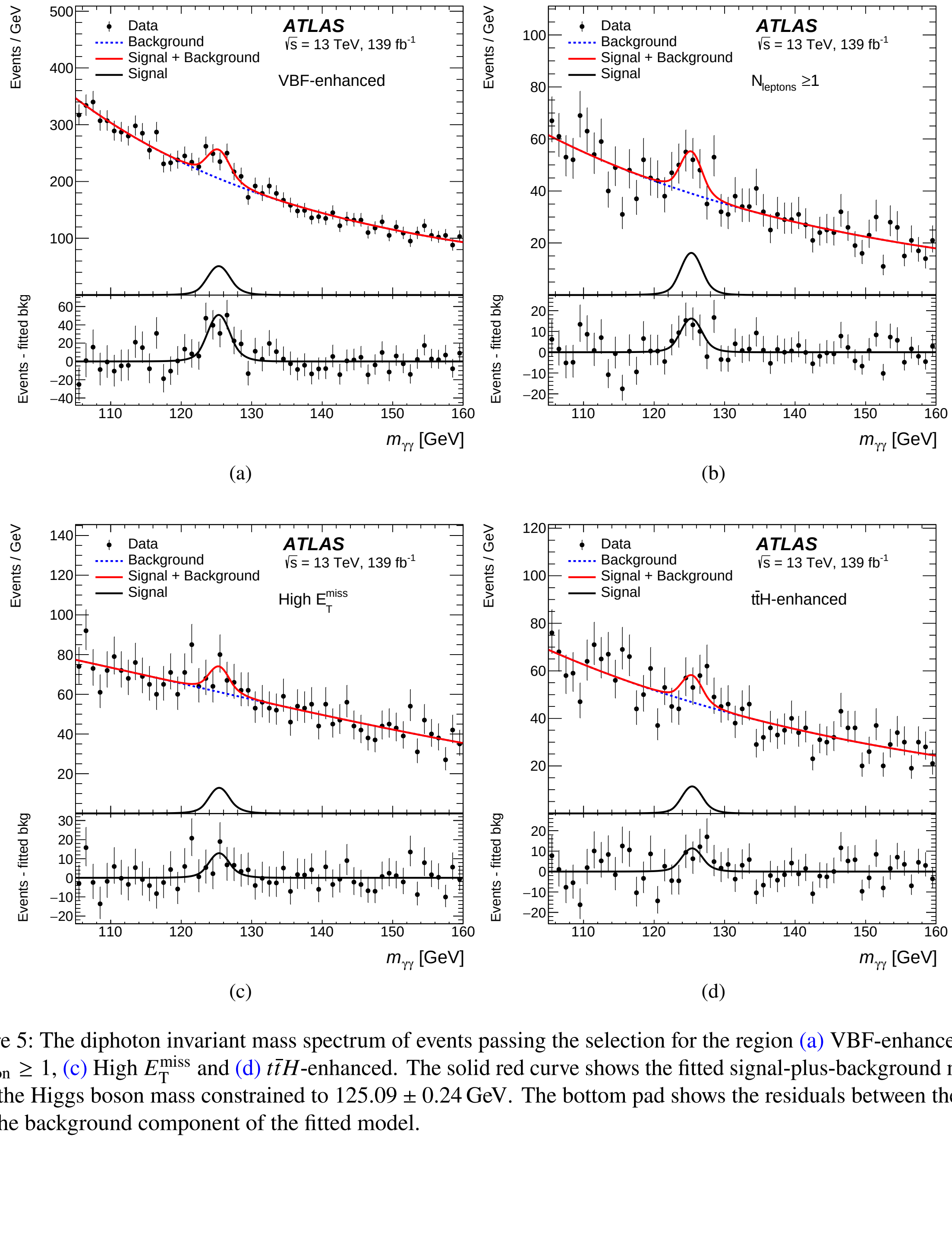

Figure 5: The diphoton invariant mass spectrum of events passing the selection for the region (a) VBF-enhanced, (b) $N_{\text{lepton}} \geq 1$, (c) High $E_{\text{T}}^{\text{miss}}$ and (d) $t\bar{t}H$-enhanced. The solid red curve shows the fitted signal-plus-background model with the Higgs boson mass constrained to 125.09 ± 0.24 GeV. The bottom pad shows the residuals between the data and the background component of the fitted model.

The uncertainty in each measured cross-section is dominated by the statistical component. Usually the spurious signal is the largest source of systematic uncertainty, typically followed by the photon energy resolution uncertainty. For fiducial regions with jet requirements, such as the VBF-enhanced one, jet energy scale and resolution uncertainties are the dominant source of systematic uncertainty, accounting for approximately 40% of the total relative uncertainty, whereas the uncertainty in the $E_{\mathrm{T}}^{\mathrm{miss}}$ reconstruction is important in the measurement of the cross-section of the High $E_{\mathrm{T}}^{\mathrm{miss}}$ fiducial region, accounting for approximately 13% of the total relative uncertainty. Table 4 summarises the systematic uncertainties and shows their relative impact on the inclusive fiducial cross-section.

Table 3: Particle-level cross-sections times branching ratio in the five fiducial regions, together with the total cross-section times branching ratio. The measured values with their statistical and systematic uncertainties are compared with the expected uncertainties and the default SM predictions. Upper-limits at 95% CL are shown for fiducial regions with observed significance below 3σ. The last column shows the probabilities from a χ^2 compatibility test between the fitted cross-sections and the SM prediction. The χ^2 is computed using the full set of uncertainties in the data and in the prediction.

Fiducial region	Measured [fb]	± stat	± sys	SM prediction [fb]	95% $\mathrm{CL_s}$ upper limit [fb]	p-value
Diphoton	67	± 5	± 4	64 ± 4	-	69%
VBF-enhanced	1.8	± 0.5	± 0.3	1.53 ± 0.10	-	64%
$N_{\mathrm{lepton}} \geq 1$	0.81	± 0.23	± 0.06	0.59 ± 0.03	-	36%
High $E_{\mathrm{T}}^{\mathrm{miss}}$	0.28	± 0.27	± 0.07	0.302 ± 0.017	0.85	93%
$t\bar{t}H$-enhanced	0.53	± 0.27	± 0.06	0.60 ± 0.05	1.13	79%
Total	132	± 10	± 8	126 ± 7	-	69%

For each measured cross-section, a χ^2 test is used to evaluate the p-value for compatibility between the measurement and the default SM prediction. The χ^2 is computed using the full set of uncertainties in the fitted cross-section and the theory uncertainties in the default SM prediction. The p-values computed in this way are listed in Table 3, showing good agreement between the measurements and predictions.

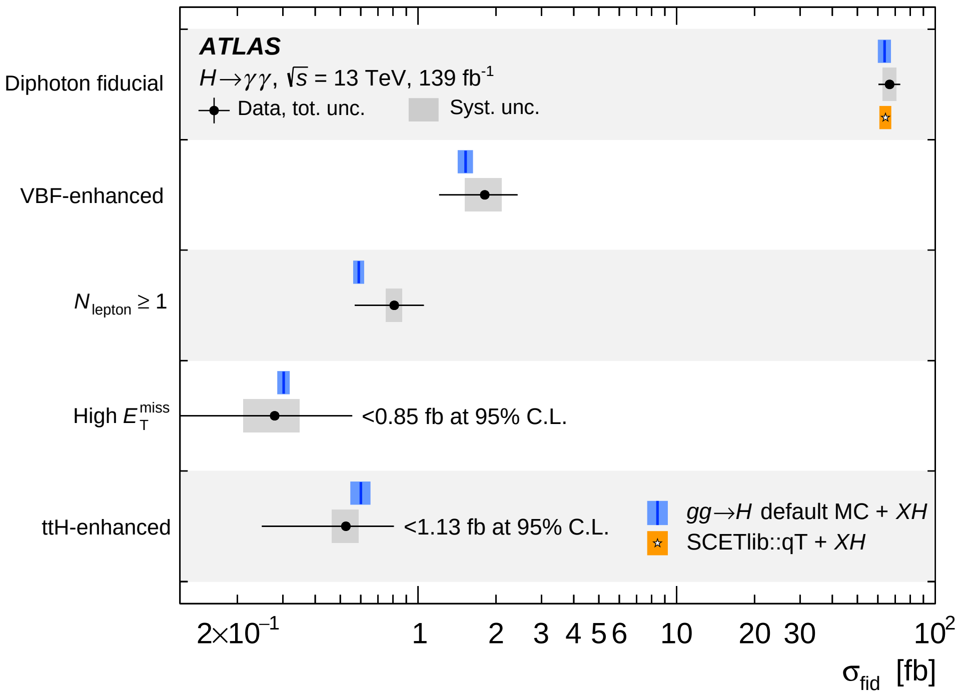

Figure 6: Particle-level cross-sections times branching ratio in the five fiducial regions. The data are shown as filled (black) circles. The error bar on each measured cross-section represents the total uncertainty in the measurement, with the systematic uncertainty shown as a dark grey rectangle. The default prediction with its uncertainty is superimposed. XH indicates all the Higgs production modes except for ggF. Upper limits at 95% CL are shown for fiducial regions with observed significance below 3σ.

Table 4: Breakdown of the uncertainties in the inclusive diphoton fiducial cross-section measurement.

Source	Uncertainty [%]
Statistical uncertainty	7.5
Systematic uncertainties	6.4
Background modelling (spurious signal)	3.8
Photon energy scale & resolution	3.6
Photon selection efficiency	2.6
Luminosity	1.8
Pile-up modelling	1.4
Trigger efficiency	1.0
Theoretical modelling	0.4
Total	9.8

8.3 Differential fiducial cross-section measurements

A subset of the measured differential fiducial cross-sections for the observables under study are reported. The corresponding correlation matrices for these observables are reported in Appendix A. Additional differential cross-section measurements are presented in Appendix B. All the results are compared with the default SM prediction. All differential measurements are limited by the statistical uncertainties. As an example, Figure 7 shows the breakdown of the uncertainties for $p_{\mathrm{T}}^{\gamma\gamma}$ and N_{jet}. The five leading sources of systematic uncertainty are shown in each plot along with the statistical uncertainty. The plots show that the leading systematic uncertainty is from the spurious signal, while important systematic uncertainties also originate from the photon selection efficiency uncertainties for photon observables, and jet energy calibration and selection uncertainties for jet observables.

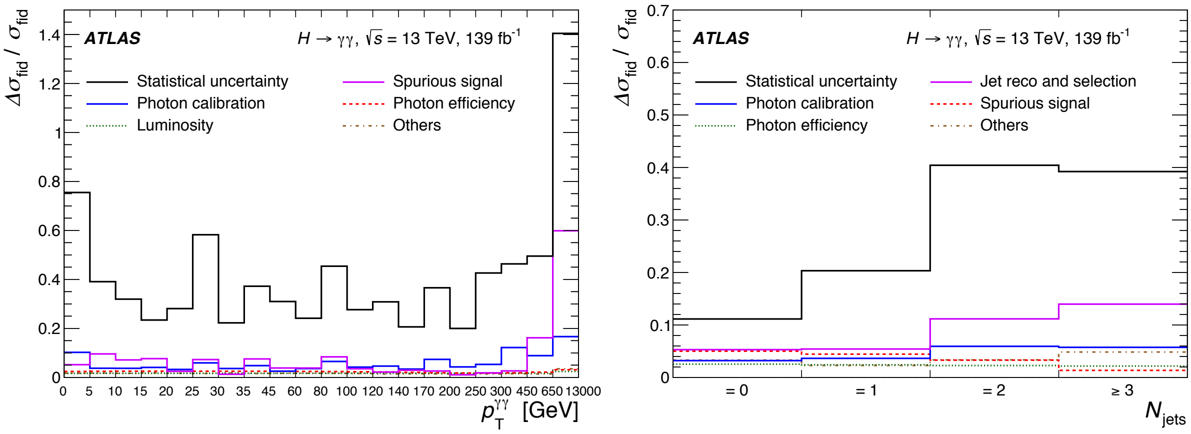

(a) (b)

Figure 7: Summary of the uncertainties in the differential cross-section measurement for (a) $p_{\mathrm{T}}^{\gamma\gamma}$, (b) N_{jet}. The five leading uncertainties are shown separately, while all other uncertainties (labelled as 'Others' in the figures) are summed in quadrature and shown as a single contribution.

Diphoton kinematics differential cross-sections Figure 8 shows the measured differential cross-sections probing $p_{\mathrm{T}}^{\gamma\gamma}$. The measured differential cross-section is in good agreement with the benchmark default simulation, and is statistically limited. The measured differential cross-sections in bins of $p_{\mathrm{T}}^{\gamma\gamma}$ include a new measurement in the boosted region $p_{\mathrm{T}}^{\gamma\gamma} > 350$ GeV using kinematic ranges similar to those used in a search for highly boosted $H \to b\bar{b}$ decays by CMS [175]. This region is of interest given its sensitivity to BSM effects. Our measurement is in agreement with the SM predictions, albeit the large uncertainties for $p_{\mathrm{T}}^{\gamma\gamma} > 650$ GeV. For $p_{\mathrm{T}}^{\gamma\gamma} > 450$ GeV, the measured cross-section is compared to the state-of-the-art predictions from the LHC Higgs Working Group (LHCHWG) [176], which match the predictions from the default simulation but provide an improved estimation of the uncertainties.

Using the $\mathrm{CL_s}$ procedure [174], 95% CL upper limits of 3.1 and 5.8 were set on the ratio $\sigma^{\mathrm{observed}}/\sigma^{\mathrm{SM}}$ for $450 < p_{\mathrm{T}}^{\gamma\gamma} < 650$ GeV and $p_{\mathrm{T}}^{\gamma\gamma} > 650$ GeV, respectively. These correspond to upper limits on the cross-section times branching ratio of 0.18 fb (0.06 fb) for $450 < p_{\mathrm{T}}^{\gamma\gamma} < 650$ GeV ($p_{\mathrm{T}}^{\gamma\gamma} > 650$ GeV). These limits are a significant improvement on the upper limits from measurements in the $H \to b\bar{b}$ channel [177], with the caveat that for $p_T^{\gamma\gamma} > 650$ GeV the photon isolation criteria in the fiducial selection reject events with $p_T^{\gamma\gamma} > 1.25$ TeV.

For the lower p_T range, the measured $p_T^{\gamma\gamma}$ distribution is compared with RadISH+NNLOjet, SCETlib and ResBos2 theoretical predictions. The first two are accurate to N^{3}LL′ in resummation accuracy, whereas ResBos2 is accurate to N^{3}LL, but all are in good agreement with the data within the statistical uncertainty.

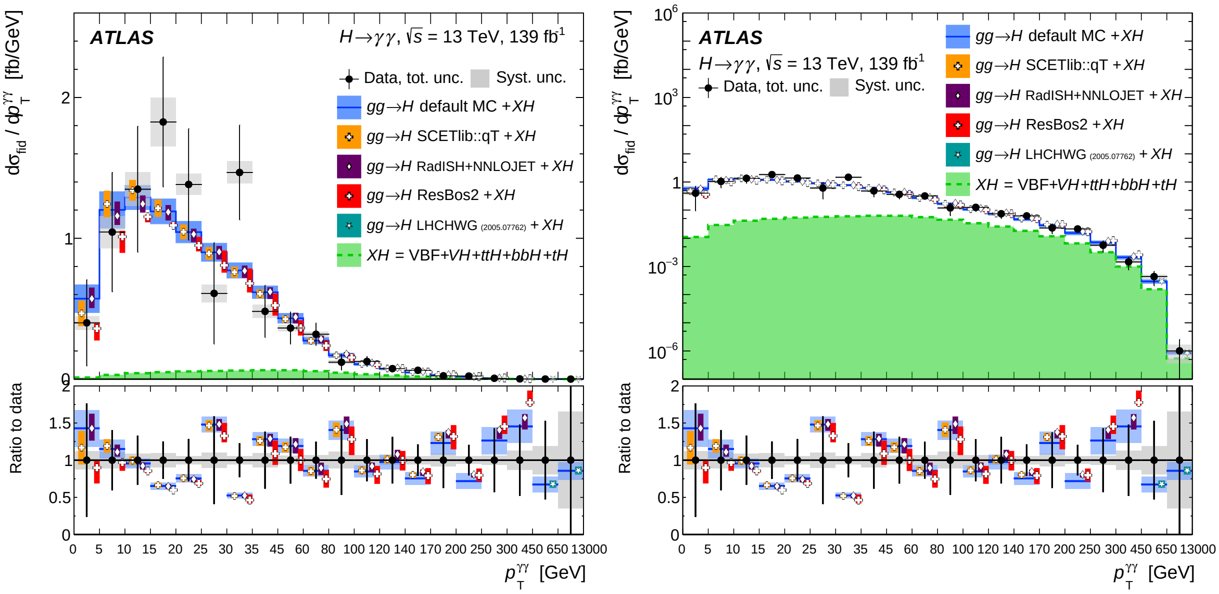

(a) (b)

Figure 8: Particle-level fiducial differential cross-sections times branching ratio for the diphoton variable $p_T^{\gamma\gamma}$ in (a) linear and (b) logarithmic scale. The measured cross-sections are compared with several predictions changing the ggF components as described in the text: the default simulation, SCETlib::qT (up to 200 GeV), RadISH+NNLOjet (up to 450 GeV), ResBos2 (up to 450 GeV) and LHCHWG (for the two highest p_T bins). Total uncertainties are indicated by the error bars on the data points, while the systematic uncertainties are indicated by the boxes. The uncertainties in the predictions are indicated with shaded bands. The bottom panel shows the predicted values from the top panel divided by data.

Jet multiplicities Measured cross-sections with respect to exclusive and inclusive jet multiplicity are shown in Figure 9, while the b-jets multiplicity dependence is shown in Figure 10. The measured cross-sections are compared with various predictions at different orders in QCD accuracy. Good agreement is observed between the measured N_{jets} and $N_{b\text{-jets}}$ distributions and the corresponding predictions. For N_{jets}, the predictions vary significantly in their uncertainties among the different bins since they vary in their order of QCD accuracy. This is most evident for NNLOjet predictions [150, 151] which is an NNLO prediction for $H+ \geq 1$ jet, and hence a leading-order prediction for the ≥ 3-jet bin, yielding a larger uncertainty. The Sherpa+MCFM+OpenLoops and GoSam predictions are at NLO for the different bins with ≥ 1 jet, and hence has a smaller uncertainty for the highest jet multiplicity. The ≥ 3-jet bin from the default simulation is produced solely by the parton shower and thus the uncertainty estimate is unreliable. The uncertainties in the different predictions for the differential cross-sections in bins of exclusive N_{jets} are underestimated as the exclusive-jet requirement results in a severe restriction of the phase space that is not taken into account in the formalism of these predictions.

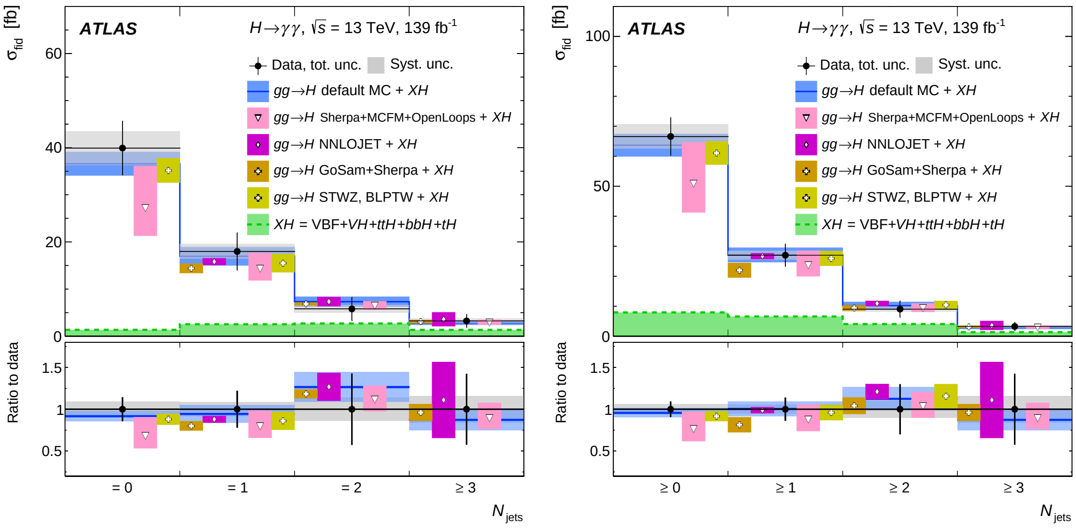

(a) (b)

Figure 9: Particle-level fiducial differential cross-sections times branching ratio for (a) the exclusive jet multiplicity N_{jets} and (b) the inclusive jet multiplicity. The NNLOJET and GoSam+Sherpa predictions are available only for the ≥ 1 jet phase space. The STWZ, BLPTW predictions are available only for the exclusive 0, 1-jet bins and the inclusive ≥ 0, ≥ 1, ≥ 2-jet bins.

≥ 1-jet differential cross-sections Figure 11 shows the measured differential cross-section for $p_{\mathrm{T}}^{j_1}$. The $p_{\mathrm{T}}^{j_1}$ distribution covers the same kinematic range as the Higgs boson $p_{\mathrm{T}}^{\gamma\gamma}$ measurement, but coarser bins were chosen at low p_{T}, with the SCETlib and RadISH+NNLOjet predictions providing the greatest accuracy (NNLO) among the different predictions. Figure 12 shows $p_{\mathrm{T}}^{\gamma\gamma}$ with a jet veto for $p_{\mathrm{T}}^{j} > 30$ GeV. The measured cross-sections are compared with the default Monte Carlo predictions and with the resummed predictions from RadISH+MATRIX and ResBos2, which carry out the jet-veto resummation at NNLL accuracy. The predictions are considered accurate up to 10 GeV above the jet-veto threshold. The current data uncertainty does not allow detailed conclusions to be drawn for various predictions, but future comparisons with improved precision will allow refinements in similar resummation calculations.

≥ 2-jet differential cross-sections Figure 13 shows the differential cross-sections for the variables m_{jj} and $\Delta\phi_{jj}$. The m_{jj} and $\Delta\phi_{jj}$ distributions are compared with Sherpa predictions that are of NLO accuracy for this jet multiplicity, whereas the default simulation is accurate only to leading order. Good agreement is observed between data and the predictions, including the default simulation. In the highest m_{jj} bin, which is more sensitive to VBF production, the data are in agreement with the predictions within the uncertainty of the measurement. The $\Delta\phi_{jj}$ distribution, which has sensitivity to the CP properties of the Higgs boson, is in good agreement with the expected shape in the SM.

Double-differential cross-sections Figure 14 shows the double-differential cross-section for $p_{\mathrm{T}}^{\gamma\gamma}$ vs $|y_{\gamma\gamma}|$. Overall, good agreement is observed between data and predictions, with SCETlib providing a more accurate description than the default simulation.

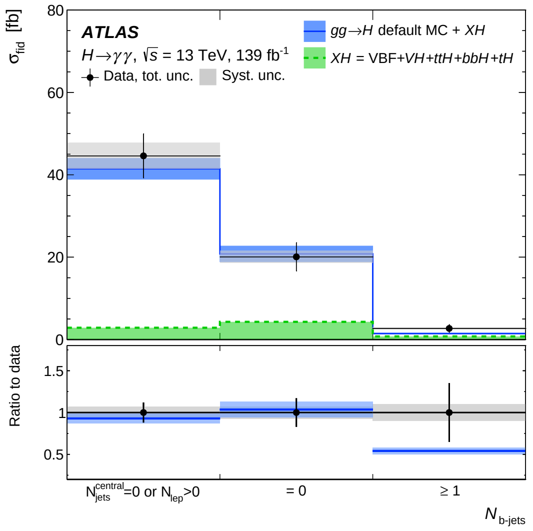

Figure 10: Particle-level fiducial differential cross-sections times branching ratio for the b-jet multiplicities variable $N_{b\text{-jets}}$. The first bin includes events with no central jets or at least one lepton, while the two other bins contain events with zero or at least one b-jet in the remaining part of the diphoton fiducial phase space.

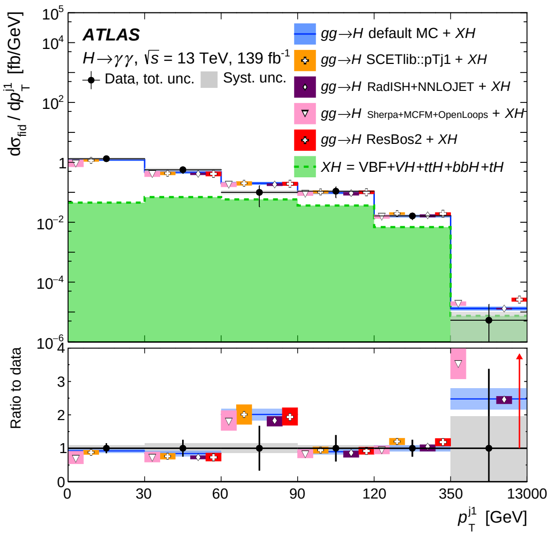

Figure 11: Particle-level fiducial differential cross-sections times branching ratio for $p_{\mathrm{T}}^{j_1}$. The ResBos2 and RadISH+NNLOJET predictions for $p_{\mathrm{T}}^{j_1}$ are available only for $p_{\mathrm{T}}^{j_1} > 30$ GeV, whereas SCETlib is available up to 350 GeV.

Cross-sections in the VBF-enhanced phase space Figure 15 shows the differential cross-section in the VBF-enhanced phase space for $\Delta\phi_{jj}$. Overall, good agreement is observed between the data and the default simulation prediction and the proVBF prediction, which is at higher-order accuracy in QCD.

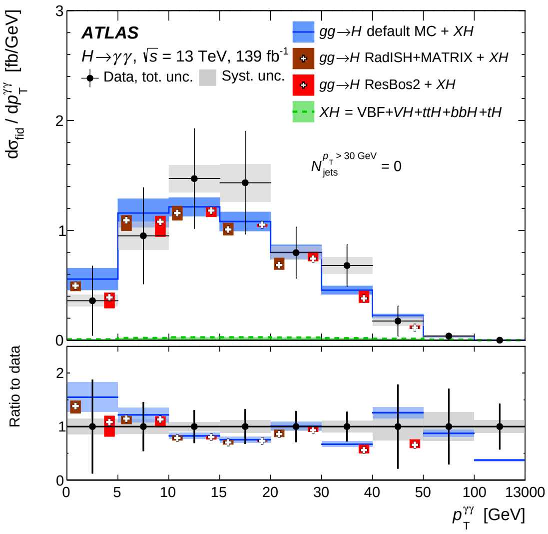

Figure 12: Particle-level fiducial differential cross-sections times branching ratio for $p_T^{\gamma\gamma}$ with a $p_T^j > 30$ GeV jet veto. The ResBos2 predictions are available up to 50 GeV. The RadISH+Matrix predictions are available up to 30 GeV.

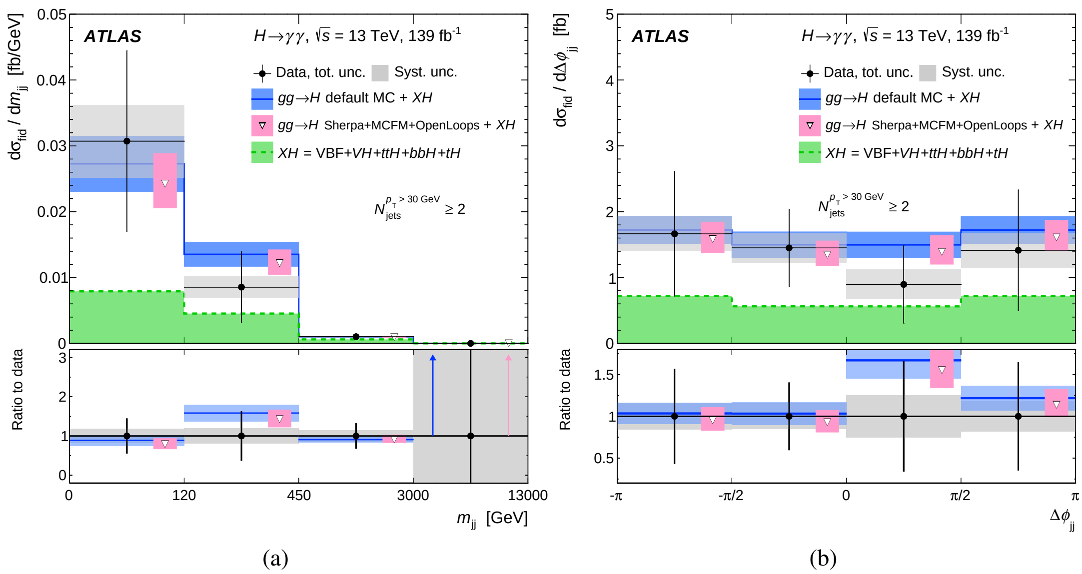

Figure 13: Particle-level fiducial differential cross-sections times branching ratio for the variables (a) m_{jj} and (b) $\Delta\phi_{jj}$ in the diphoton baseline fiducial region.

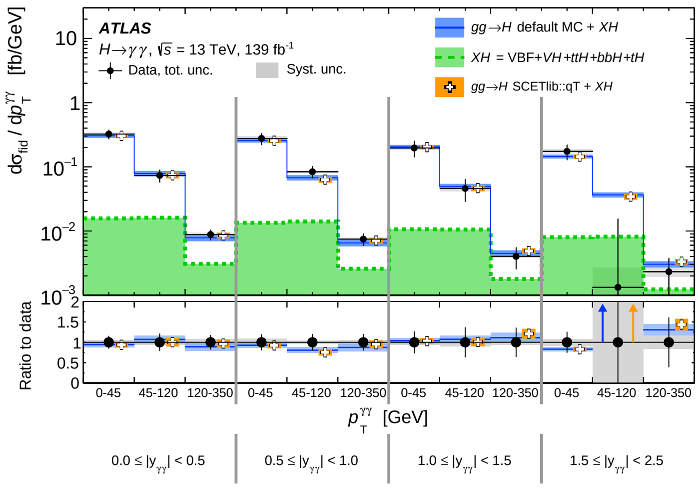

Figure 14: Double-differential particle-level fiducial cross-sections times branching ratio of $p_{\mathrm{T}}^{\gamma\gamma}$ in bins of $|y_{\gamma\gamma}|$.

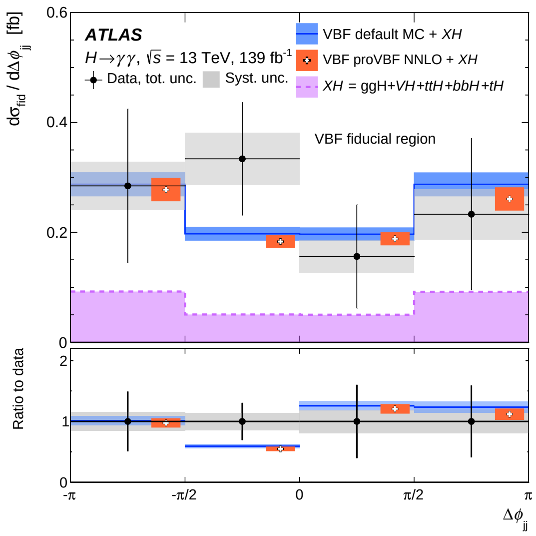

Figure 15: Particle-level fiducial differential cross-sections times branching ratio for $\Delta\phi_{jj}$ in the VBF-enhanced fiducial region.

Similarly to the inclusive cross-sections, a χ^2 test was used to evaluate p-values for the compatibility of the measured differential cross-sections and the predictions. For the uncertainty in the theoretical predictions, the correlation is ignored since it is not available for most of the predictions. Using the default simulation prediction, it was estimated that neglecting this correlation can change the p-value by few percent. As indicated in Table 5, the measurements are compatible with the SM for all the predictions. In addition, it was checked that when fitting different differential cross-sections relative to the same fiducial region the integrals of the signal yields in the bins are compatible.

Table 5: The p-values obtained with a χ^2 compatibility test between the fitted cross-sections and the SM predictions for each differential distribution. The χ^2 is computed using the full set of uncertainties for the data, including their correlation, and for the SM predictions. The correlation of the SM predictions are neglected as most of the predictions are provided without this information.

Variable	p-value									
	default	RadISH NNLOJET	NNLOJet	STWZ BLPTW	MATRIX	Sherpa	GoSam	SCETlib	TAUC	ResBos2	proVBF
$p_T^{\gamma 1}/m_{\gamma\gamma}$	56%	–	–	–	–	–	–	58%	–	32%	–
$p_T^{\gamma 2}/m_{\gamma\gamma}$	93%	–	–	–	–	–	–	49%	–	2%	–
$p_T^{\gamma\gamma}$	86%	68%	–	–	–	–	–	78%	–	54%	–
$\lvert y_{\gamma\gamma}\rvert$	76%	–	–	–	–	–	–	78%	–	66%	–
$p_T^{j_1}$	78%	77%	–	–	–	47%	–	48%	–	38%	–
N_{jets}	95%	–	90%	56%	–	59%	84%	–	–	–	–
$N_{b\text{-jets}}$	60%	–	–	–	–	–	–	–	–	–	–
$p_T^{\gamma\gamma j}$	81%	–	–	–	–	68%	–	–	–	78%	–
$m_{\gamma\gamma j}$	95%	–	–	–	–	95%	–	–	–	–	–
$\tau_{C,j1}$	27%	–	–	–	–	–	–	–	11%	13%	–
$\sum \tau_{C,j}$	39%	–	–	–	–	–	–	–	–	–	–
H_T	46%	–	–	–	–	51%	–	–	–	–	–
m_{jj}	79%	–	–	–	–	81%	–	–	–	–	–
$\Delta\phi_{jj}$	91%	–	–	–	–	95%	–	–	–	–	–
$\lvert\Delta\phi_{\gamma\gamma,jj}\rvert$	83%	–	–	–	–	88%	–	–	–	–	–
$p_{T,\gamma\gamma jj}$	99%	–	–	–	–	100%	–	–	–	–	–
$p_T^{\gamma\gamma\text{ jetveto 30 GeV}}$	84%	–	–	–	83%	–	–	–	–	83%	–
$p_T^{\gamma\gamma\text{ jetveto 40 GeV}}$	95%	–	–	–	45%	–	–	–	–	83%	–
$p_T^{\gamma\gamma\text{ jetveto 50 GeV}}$	88%	–	–	–	35%	–	–	–	–	30%	–
$p_T^{\gamma\gamma\text{ jetveto 60 GeV}}$	67%	–	–	–	52%	–	–	–	–	42%	–
$p_T^{\gamma\gamma}$ vs $\lvert y_{\gamma\gamma}\rvert$	75%	–	–	–	–	–	–	78%	–	–	–
$p_T^{\gamma\gamma}$ vs $\tau_{C,j1}$	39%	–	–	–	–	–	–	–	–	–	–
$p_T^{\gamma\gamma}$ vs $p_T^{\gamma\gamma j}$	96%	–	–	–	–	–	–	–	–	–	–
$(p_T^{\gamma 1} - p_T^{\gamma 2})/m_{\gamma\gamma}$ vs $(p_T^{\gamma 1} + p_T^{\gamma 2})/m_{\gamma\gamma}$	81%	–	–	–	–	–	–	77%	–	–	–
VBF $\lvert\eta^*\rvert$	94%	–	–	–	–	–	–	–	–	–	70%
VBF $\Delta\phi_{jj}$	68%	–	–	–	–	–	–	–	–	–	65%
VBF $p_T^{j_1}$	77%	–	–	–	–	–	–	–	–	–	70%
VBF $p_{T,\gamma\gamma jj}$	89%	–	–	–	–	–	–	–	–	–	74%
VBF $p_T^{j_1}$ vs $\Delta\phi_{jj}$	76%	–	–	–	–	–	–	–	–	–	74%

9 Interpretations of the measured differential cross-sections

The fiducial cross-section measurements, shown in Section 8, are largely model independent. This allows direct comparisons with various theory predictions as well as interpretations in alternative theoretical frameworks. In this section, the measured cross-sections are used to constrain b- and c-quark Yukawa coupling modifiers relative to the SM, κ_b and κ_c, detailed in Section 9.1 and to probe physics beyond the SM via the effective field theory approach, detailed in Section 9.2.

9.1 Limits on the b- and c-quark Yukawa couplings using the Higgs boson p_T spectrum

The Higgs boson p_T spectrum is sensitive to the Yukawa couplings of the Higgs boson to the b- and c-quarks. This sensitivity is driven by quark-initiated ($q\bar{q}$ and qg) production of the Higgs boson and the contributions of b- and c-quarks to the loop-induced ggF production. Direct observations of the Higgs boson coupling to b-quarks [19, 178] provided stringent constraints on its possible modification with respect to the SM, whereas current searches for Higgs boson decays to charm final states [179–181] still allow for a relatively large modification of the c-quark coupling. This paper presents an indirect method [25] to probe the b- and c-coupling modifiers, κ_b and κ_c, through the measured $p_\mathrm{T}^{\gamma\gamma}$ spectrum, which has the advantage of not being limited by the tagging efficiency for jets originating from b- and c-quarks. The current uncertainties from direct searches are approximately 20% for κ_b [144, 182], whereas for κ_c, current limits from direct searches are at $|\kappa_c| < 8.5$ [179].

Modifications of the coupling strength to b- and c-quarks would impact the ggF and quark-initiated production modes, thus resulting in changes in both the normalisation and the shape of the $p_\mathrm{T}^{\gamma\gamma}$ spectrum. In addition, the branching ratio for the $H \to \gamma\gamma$ decay would be affected by changes in the $H \to \gamma\gamma$ decay width and in the total Higgs boson decay width. Two different fitting strategies are presented to provide limits on κ_b and κ_c with an increasing level of model dependency. In the first case, only the shape of the measured $p_\mathrm{T}^{\gamma\gamma}$ spectrum is considered, whereas the second case also considers normalisation changes due to the cross-section variations in addition to the variations of the $H \to \gamma\gamma$ partial decay width and the total Higgs boson width. All the other Higgs boson production modes remain unchanged with κ_b and κ_c variations, and their contributions are taken from the default simulation.

The predictions for κ_b and κ_c modifications of ggF production are computed with SCETLIB [160, 161], detailed in Sections 8.1 and Appendix C, including also the bottom- and charm-quark loop contributions. In all the $p_\mathrm{T}^{\gamma\gamma}$ bins, the dominant contribution to the ggF cross-section is given by the top-quark loop. The interference between the top-quark gluon-fusion loop and the b- and c-quark gluon-fusion loops is comparatively small, but not negligible, and negative for $p_\mathrm{T}^{\gamma\gamma} < 100$ GeV. The contributions of b- and c-quark gluon-fusion processes and the interference between them are found to be very small.

Predictions for quark-initiated $b\bar{b} \to H$ and $c\bar{c} \to H$ production modes are computed with MADGRAPH5_AMC@NLO 2.7.3, including the higher-order contributions $bg \to Hb$ and $cg \to Hc$, using a dedicated PDF set from Ref. [183]. PYTHIA 8 with the A14 tune [51] is used for the simulation of the parton shower, hadronisation and underlying event, as well as the Higgs boson decay. The inclusive $b\bar{b} \to H$ and $c\bar{c} \to H$ cross-sections are then normalised to the state-of-the-art NNLO computations available in Refs. [183, 184]. The uncertainties due to missing higher-order QCD terms are estimated from simultaneous variations of the renormalisation and factorisation scales around their central values by factors of 1/2 and 2. The uncertainty from the choice of the FxFx merging scale is estimated by varying the nominal scale (40 GeV) by factors of 1/2 and 2. Among these variations, only the downward variation has considerable impact on the $p_\mathrm{T}^{\gamma\gamma}$ spectrum. The PDF uncertainty for $c\bar{c} \to H$ production is based on the standard deviation computed using the 100 eigen-variations included in the PDF set, in addition to α_s uncertainties. For b-quark-initiated production, the PDF-induced uncertainty in the $b\bar{b} \to H$ predictions is obtained from variations of the b-quark pole mass and the threshold above which the b-quark PDF is non-zero [183].

Variations in the $H \to \gamma\gamma$ branching ratio from modifications of κ_b and κ_c are estimated using HDECAY [185, 186]. This includes variations in the partial $H \to \gamma\gamma$ decay width, in addition to changes in the total Higgs boson width dominated by decay width modifications from $H \to b\bar{b}$ and $H \to c\bar{c}$.

The statistical interpretation of the $p_{\mathrm{T}}^{\gamma\gamma}$ distribution to set limits on the values of κ_b and κ_c is performed with the profile likelihood method. The measured differential cross-sections in bins of $p_{\mathrm{T}}^{\gamma\gamma}$ is compared with the predictions parameterised as a function of κ_b and κ_c. Limits on the κ coefficients are set by constructing a likelihood function which is defined, up to a constant normalisation factor, as:

$$L = \exp\left[-\frac{1}{2}(\sigma_{\mathrm{obs}} - \sigma_{\mathrm{H}}(\kappa_b, \kappa_c, \theta))^{\mathrm{T}} V^{-1} (\sigma_{\mathrm{obs}} - \sigma_{\mathrm{H}}(\kappa_b, \kappa_c, \theta))\right] \times C(\theta)\,,$$

where σ_{obs} is the vector of the measured cross-sections times branching ratio, V is the covariance matrix using the full uncertainty of the measurement, $\sigma_{\mathrm{H}}(\kappa_b, \kappa_c, \theta)$ is the vector of the predicted cross-sections times branching ratio where θ represents nuisance parameters accounting for the various theoretical uncertainties for the different production modes with κ_b and κ_c variations, and $C(\theta)$ is the constraint term of these nuisance parameters. The 95% CL limits are computed using a test statistic based on a ratio of profiled likelihoods [187]. The measured differential cross-section is used in the range of $p_{\mathrm{T}}^{\gamma\gamma}$ up to 200 GeV, which is the region most sensitive to variations of κ_b and κ_c. The fits were performed with the Higgs boson coupling to the top quark fixed to the SM value ($\kappa_t = 1$). All other Higgs boson couplings are assumed to have SM values ($\kappa = 1$). The observed and expected 95% confidence intervals are shown in Table 6 for the different fitting strategies. The table shows that stricter limits can be computed by including both shape and normalisation variations. The limits on a given κ parameter are determined while fixing the other one to its SM value $\kappa = 1$. The shape-only limits on κ_b are more stringent than those on κ_c, due to the larger contribution from $b\bar{b}$-initiated process and the κ_b term in the ggF loop. The limits on κ_c are mostly driven by $c\bar{c}$-initiated processes. Figures 16 and 17 show data compared with predictions for two values of κ_b and κ_c corresponding to the upper and lower limits at 95% CL from the different fitting strategies. In addition, two-dimensional limits are derived by simultaneously varying κ_b and κ_c, and the contours for these limits are shown in Figure 18. In this case the goodness of the fit was computed with a χ^2 test, resulting in a p-value of 0.70 when using only the shape and 0.66 when also using the normalisation.

The observed κ_b and κ_c limits are comparable with the limits reported in Ref. [14], which follows a similar approach when interpreting the Higgs boson differential cross-sections but uses multiple decay channels. When also using the normalisation information, the observed κ_b limits are comparable with those from the direct searches. The observed constraints on κ_c are stronger than those from direct searches. In addition to the limits reported below, an additional check was performed by allowing κ_t to float in the fit within the limits of the latest $H \to \gamma\gamma$ couplings measurement [3]. This had a negligible effect on the shape-only limits on κ_b and κ_c, whereas the absolute values of the shape-plus-normalisation limits on κ_b and κ_c increased considerably (up to 40%). If the full likelihood of the measurements is used, instead of the cross section values and their covariance matrix, the limit on κ_b is improved by about 3%, that on κ_c is degraded by about 5%.

9.2 Limits on anomalous Higgs boson interactions using the Effective Field Theory approach

The strength and tensor structure of the Higgs boson interactions are investigated following an effective field theory approach. In this approach, an effective Lagrangian [188] is defined by the SM Lagrangian,

Table 6: Observed and expected allowed ranges at 95% CL of modifications of the b- and c-quark Yukawa couplings to the Higgs boson, κ_b and κ_c. The limits on a given κ parameter are computed while fixing the other one to its SM value ($\kappa = 1$). The table shows the confidence intervals for κ_b and κ_c using shape-only and using shape and normalisation variations of the SM expectation.

Fit set-up	κ	Observed 95% CL	Expected 95% CL
Shape-only	κ_c	$[-13.0,\ 18.9]$	$[-10.1,\ 17.3]$
	κ_b	$[-3.7,\ 10.4]$	$[-2.6, 8.1]$
Shape+normalisation (with branching ratio variations)	κ_c	$[-2.7,\ 2.6]$	$[-3.1,\ 3.2]$
	κ_b	$[-1.2,\ -0.8] \cup [0.8,\ 1.1]$	$[-1.2,\ -0.9] \cup [0.8,\ 1.2]$

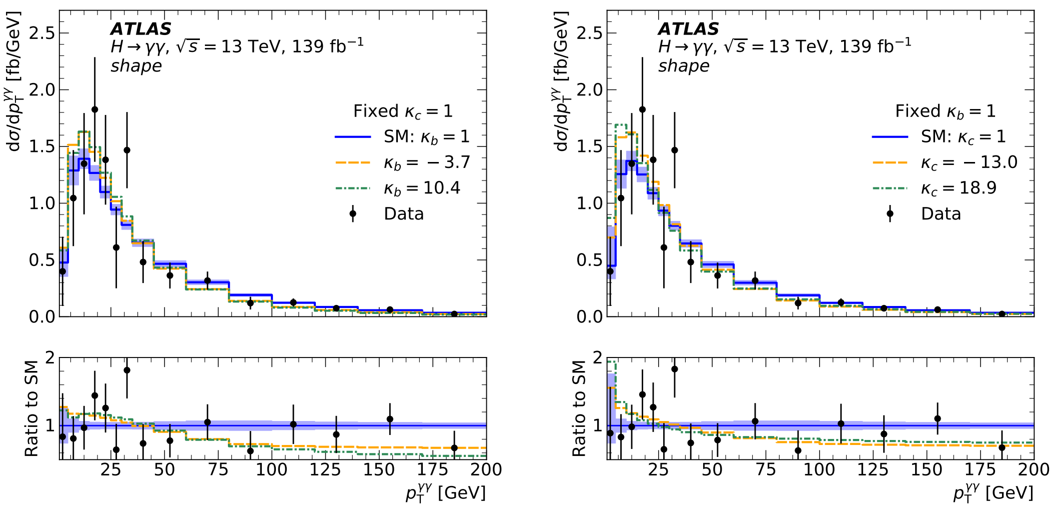

(a) (b)

Figure 16: The observed fiducial differential cross-section times branching ratio for $p_T^{\gamma\gamma}$ compared with the predictions for different values of (a) κ_b and (b) κ_c corresponding to the upper (in green) and lower (in orange) limits at 95% CL for the shape-only fitting strategy. The SM prediction is shown as a blue line with the theoretical uncertainties of the SM prediction as a filled area. The bottom panels show the ratios of the data and the different predictions to the SM prediction.

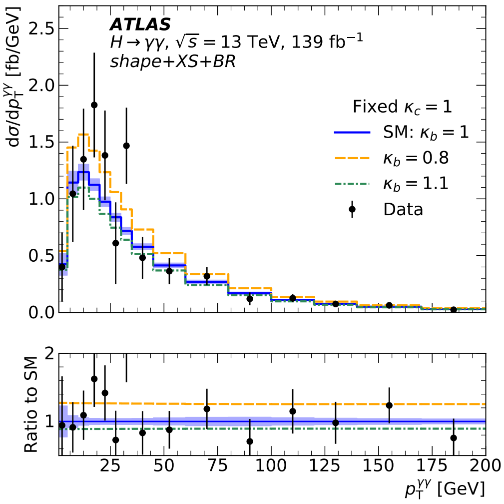

(a)

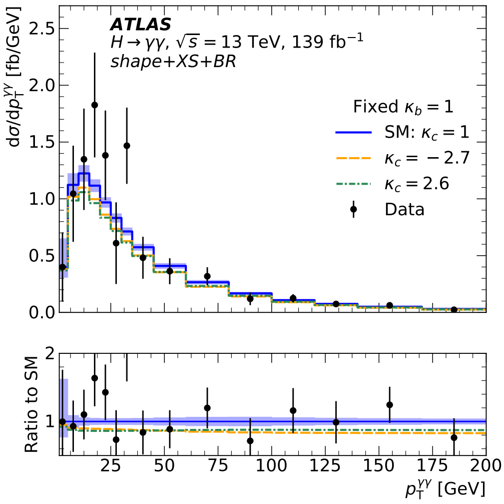

(b)

Figure 17: The observed fiducial differential cross-section times branching ratio for $p_T^{\gamma\gamma}$ compared with the predictions for different values of (a) κ_b and (b) κ_c corresponding to the upper (in green) and lower (in orange) limits at 95% CL for the shape and normalisation fitting strategy (with 'XS+BR' denoting 'cross-section and branching ratio'). The SM prediction is shown as a blue line with the theoretical uncertainties of the SM prediction as a filled area. The bottom panels show the ratios of the data and the different predictions to the SM prediction.

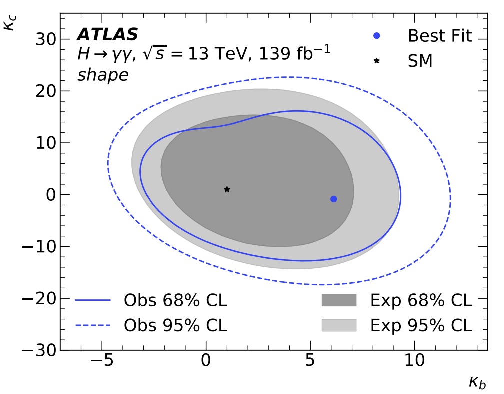

(a)

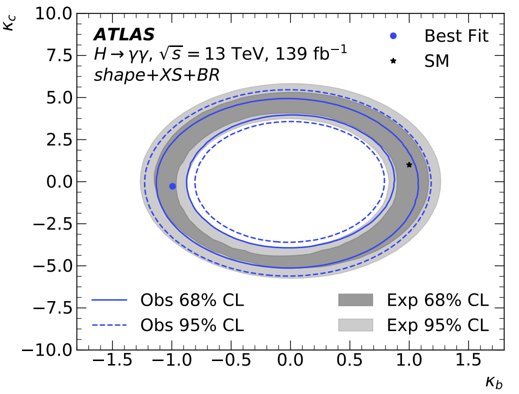

(b)

Figure 18: Observed and expected 2D limits on κ_b and κ_c when considering modifications of (a) the shape and (b) the shape and normalisation (with 'XS+BR' denoting 'cross-section and branching ratio') at 68% and 95% CL.

$\mathcal{L}_{\text{SM}}$ supplemented by additional dimension-6 operators, $O_i^{(6)}$ specified by

$$\mathcal{L}_{\text{EFT}} = \mathcal{L}_{\text{SM}} + \sum_i \frac{c_i}{\Lambda^2} O_i^{(6)},$$

where the c_i specify the strengths of the new interactions and are known as the *Wilson coefficients*, and Λ is the scale of new physics. Contributions from new physics to the differential cross-sections are then probed as non-zero values of the Wilson coefficients of the dimension-6 operators. Non-zero values of these Wilson coefficients can modify the event rates and the kinematic properties of the Higgs boson, and associated jet spectra, from those predicted by the SM.

Contributions from dimension-5 and dimension-7 operators are excluded by assuming lepton and baryon number conservation. Operators with dimension-8 or higher are neglected as their effects are suppressed by at least $1/\Lambda^2$ relative to dimension-6 operators. From the available bases for parameterising the dimension-6 operators, the Warsaw basis of the Standard Model EFT (SMEFT) Lagrangian [189, 190] is used to probe Higgs boson interactions with gauge bosons.

Limits on the Wilson coefficients are obtained using a simultaneous fit to five measured fiducial differential cross-sections, including their correlations, in the following variables: $p_{\text{T}}^{\gamma\gamma}$, N_{jets}, m_{jj}, $\Delta\phi_{jj}$ and $p_{\text{T}}^{j_1}$.

In the SMEFT formulation, the following operators are considered:

$$\begin{aligned}\mathcal{L}_{\text{eff}}^{\text{SMEFT}} \supset \quad & c_{HG} O'_g + c_{HW} O'_{HW} + c_{HB} O'_{HB} + c_{HWB} O'_{HWB} \\ & + c_{H\widetilde{G}} \widetilde{O}'_g + c_{H\widetilde{W}} \widetilde{O}'_{HW} + c_{H\widetilde{B}} \widetilde{O}'_{HB} + c_{H\widetilde{W}B} \widetilde{O}'_{HWB},\end{aligned}$$

The coefficient c_{HG} and its CP-odd counterpart $c_{H\widetilde{G}}$ determine the strength of operators that affect ggF production, while c_{HW}, c_{HB}, c_{HWB} and their corresponding CP-odd counterparts, $c_{H\widetilde{W}}$, $c_{H\widetilde{B}}$, $c_{H\widetilde{W}B}$, correspond to operators that impact VBF and VH production and the Higgs boson decay to photons.

The effective Lagrangian is implemented in FeynRules [191] within the SMEFTsim package [192]. The implementation uses $U(3)^5$ flavour symmetry with non-SM CP-violating phases and the α scheme that uses α_{EW}, m_Z, and G_{F} as the input parameters for the electroweak sector. Event generation was performed using MadGraph 2.7.3 [48] for ggF, VBF and VH production modes with leading-order matrix elements. The event generation was performed with the BSM scale set to $\Lambda = 1$ TeV. The ggF Higgs boson events were generated with up to two additional partons in the final state and were merged using the MLM matching scheme to create the full final state [193]. The remaining Higgs boson production modes, i.e. $t\bar{t}H$ and $b\bar{b}H$, are fixed to their SM expectation.

For each production mode, events were generated using the NNPDF2.3lo PDF set [89] and the A14 tune [51]. The parton-level events were then passed to Pythia 8 for parton showering, hadronisation and underlying-event simulation. The analysis Rivet [194] routine is used to apply the fiducial selections and calculate the observables to obtain the differential cross-section predictions.

It is assumed that higher-order QCD and electroweak corrections are the same for leading-order SM predictions and leading-order predictions that contain contributions from new physics. Therefore, to obtain predictions at a given value of the Wilson coefficient, c_i, the following formula is used:

$$\left(\frac{\mathrm{d}\sigma}{\mathrm{d}X}\right)_{c_i} = \sum_j \left(\frac{\mathrm{d}\sigma_j}{\mathrm{d}X}\right)^{\text{SM}} \times \left(\frac{\mathrm{d}\sigma_j}{\mathrm{d}X}\right)^{\text{MG5}}_{c_i} \Bigg/ \left(\frac{\mathrm{d}\sigma_j}{\mathrm{d}X}\right)^{\text{MG5}}_{c_i=0},$$

where the summation j is over the different Higgs boson production mechanisms, 'MG5' labels the MadGraph predictions and 'SM' labels the default SM predictions. The 'MG5' cross-sections at any given value of the Wilson coefficients are obtained using a multidimensional interpolation with the Professor method [195]. The interpolation relies on BSM predictions generated at benchmark non-zero Wilson coefficients. The 'MG5' cross-section at a given value of a Wilson coefficient can be separated into three components:

$$\sigma \propto |\mathcal{M}_{\text{EFT}}|^2 = |\mathcal{M}_{\text{SM}}|^2 + 2Re(\mathcal{M}^*_{\text{SM}}\mathcal{M}_{\text{d6}}) + |\mathcal{M}_{\text{d6}}|^2 \ ,$$

where the first term is the dimension-4 squared matrix element for the SM, independent of the Wilson coefficients c_i, the second term represents the interference between the SM operators and the dimension-6 operators, which is of order c_i/Λ^2 and therefore linear in c_i, and the last term is the squared matrix element for the dimension-6 operators, which is of order c_i^2/Λ^4 and thus quadratic in c_i. For small values of the Wilson coefficients, the interference term, $\sim c_i/\Lambda^2$, is the dominant BSM contribution to the cross-section. For CP-odd operators, the separation of the SM–BSM interference components from the pure BSM components allows purely CP-violating effects to be probed. Samples of approximately 400 000 events were generated for each production mode for different values of each Wilson coefficient and used to derive the parameterisation of the observables as a function of c_i.

Non-zero values of the Wilson coefficients cause changes in the $H \to \gamma\gamma$ partial width and the Higgs boson total decay width, and therefore in the $H \to \gamma\gamma$ branching ratio. The modifications of the $H \to \gamma\gamma$ partial width and the Higgs boson total decay width, including both the interference-only and the interference-plus-quadratic terms, were computed using MadGraph. It was verified that when neglecting quadratic terms the results agree with those obtained using the linear coefficients of the interference term provided in Ref. [196].

The combined effect of the modifications induced by the Wilson coefficients c_i in both the cross-section and the branching ratio (B) leads to the following expansion, as a function of c_i/Λ^2, of the product $\sigma \times B$:

$$\sigma \times B = \sigma_{\text{SM}}B_{\text{SM}} + (\sigma_{\text{SM}}B_{\text{INT}} + \sigma_{\text{INT}}B_{\text{SM}}) + (\sigma_{\text{SM}}B_{\text{BSM}} + \sigma_{\text{BSM}}B_{\text{SM}}) + O(c_i^3/\Lambda^6),$$

where the product $\sigma_{\text{SM}}B_{\text{SM}}$ of the SM cross-sections and branching ratio, independent of c_i, is modified by the first term in parentheses, linear in c_i, which results from the SM–BSM interference effects on either the cross-section (σ_{INT}) or the branching ratio (B_{INT}), and by the second term in parentheses, quadratic in c_i, arising from the product of the SM cross-section and the BSM term of the branching ratio and vice versa. Following the recommendations from the authors of Ref. [196], quadratic terms of the form $\sigma_{\text{INT}}B_{\text{INT}}$ are excluded, since otherwise contributions from dimension-8 operators would need to be included as well in order to guarantee to the renormalisability of the processes under study.

Figure 19 shows modifications of the differential cross-sections used for benchmark non-zero values of SMEFT Wilson coefficients. The coefficient c_{HG} and its CP-odd counterpart $c_{H\tilde{G}}$ affect ggF production while c_{HB}, c_{HW}, c_{HWB} and their CP-odd counterparts affect VBF+VH production. The main effect of c_{HB}, c_{HW} and also c_{HWB}, however, is on the $H \to \gamma\gamma$ decay rate, impacting the overall normalisation. The CP-odd coefficients, as seen in Figure 19, exhibit sensitivity only to the $\Delta\phi_{jj}$ observable when only the interference term is considered [197].

Statistical interpretation Limits on Wilson coefficients are set by constructing a likelihood function which is defined, up to a constant normalisation factor, as

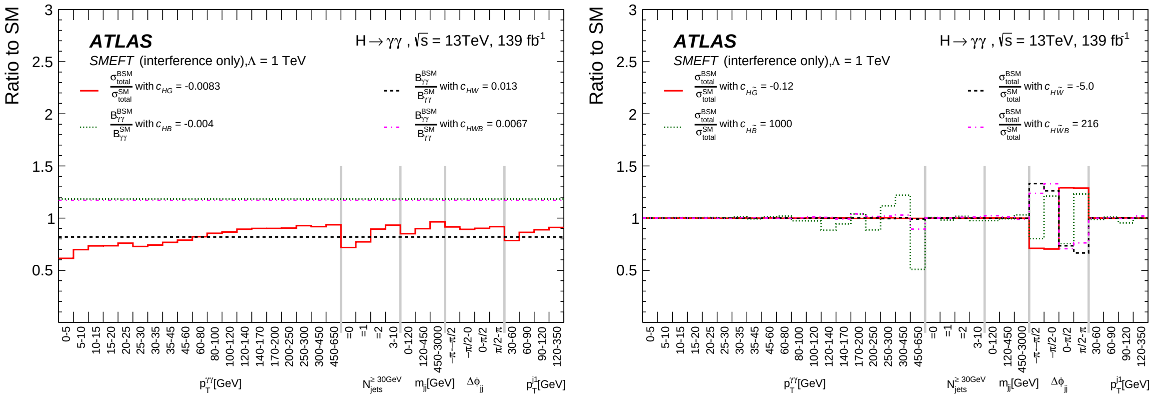

(a)

(b)

Figure 19: The effect on the five differential distributions used in the analysis of (a) the CP-even coefficients c_{HG}, c_{HB}, c_{HW}, c_{HWB} and (b) the CP-odd coefficients $c_{H\widetilde{G}}$, $c_{H\widetilde{B}}$, $c_{H\widetilde{W}}$, $c_{H\widetilde{W}B}$ of the SMEFT effective Lagrangian for values of the coefficients close to the expected limits. The c_{HB}, c_{HW}, c_{HWB} variations at the expected limits affect mainly the $H \rightarrow \gamma\gamma$ branching ratio with negligible effects on the cross-section. The effect is shown at a new-physics scale $\Lambda = 1$ TeV.

$$L = \exp\left[-\frac{1}{2}\left(\sigma_{\text{obs}} - \sigma_{\text{pred}}\right)^{\text{T}} C^{-1}\left(\sigma_{\text{obs}} - \sigma_{\text{pred}}\right)\right],$$

where σ_{obs} and σ_{pred} are k-dimensional vectors from the measured and predicted differential cross-sections of the five analysed observables, with $k = 34$ equal to the total number of bins of the five distributions used in the fit, $C = C_{\text{stat}} + C_{\text{syst}} + C_{\text{theo}}$ is the $k \times k$ total covariance matrix defined as the sum of the statistical, systematic and theoretical covariances. The overflow bins for $p_{\text{T}}^{\gamma\gamma}$, m_{jj} and $p_{\text{T}}^{j_1}$ are not used in the limit-setting fit as they extend beyond the assumed new-physics scale $\Lambda = 1$ TeV.

The statistical covariance matrix is obtained with a bootstrapping technique and the resulting correlation matrix shown in Figure 20. The matrix provides a measure of the statistical correlations between cross-section bins because the same events in data will populate the different observables used in the fit.

The covariance matrices for systematic and theoretical uncertainties are constructed from the uncertainties listed in Section 7. Theoretical uncertainties are considered for the different production modes using the default SM MC simulation to estimate the effect of QCD scale and PDF variations, detailed in Section 8.1, and are considered to be independent of new physics. Identical sources are assumed to be fully correlated across bins and variables. In addition, nuisance parameters are included in the fit to account for limited MC sample size, typically affecting the highest $p_{\text{T}}^{\gamma\gamma}$ and m_{jj} bins. In what follows, the likelihood function is numerically maximised to determine L_{max} and confidence intervals for one or several Wilson coefficients are determined via

$$1 - \text{CL} = \int_{-2\ln L(c_i)+2\ln L_{\text{max}}}^{\infty} \mathrm{d}x\, f(x),$$

with $L(c_i)$ denoting the likelihood value evaluated for a given Wilson coefficient value c_i, and $f(x)$ denoting the distribution of the test statistic, $-2\log(L(c_i)/L_{\text{max}})$. The coverage of 68% and 95% CL limits using the likelihood ratio scan was validated using pseudo-experiments.

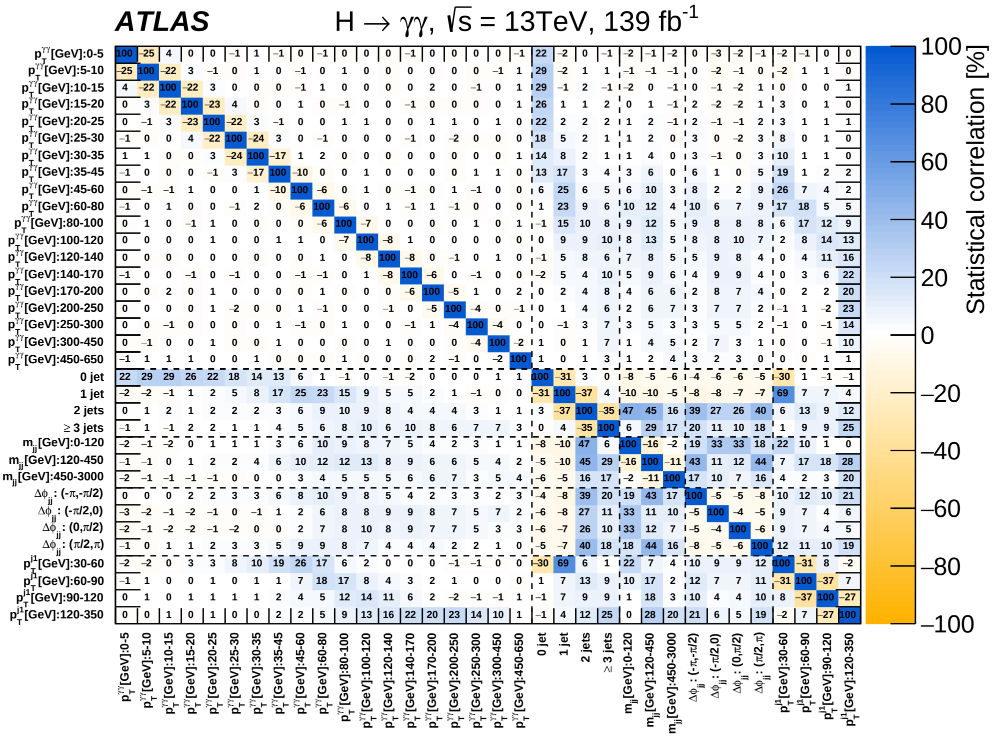

Figure 20: The observed statistical correlations, evaluated with a bootstrapping technique, between $p_{\mathrm{T}}^{\gamma\gamma}$, N_{jets}, m_{jj}, $\Delta\phi_{jj}$ and $p_{\mathrm{T}}^{j_1}$ are shown

In Table 7, the observed 95% CL limits are shown for the considered Wilson coefficients. The limits are also summarised in Figure 21. The limits are obtained assuming that all Wilson coefficients other than the one quoted are zero. The limits are provided for two scenarios, one where predictions are obtained using only the interference term, and the other where both the interference term and the quadratic term are included. Since the interference terms dominate the predicted cross-sections, the limits in the two approaches are very similar for coefficients of CP-even operators. Significant differences emerge for the CP-odd ones, for which the interference term cross-section vanishes for CP-even observables, and the sensitivity to pure CP-violating effects is obtained through the $\Delta\phi_{jj}$ observable. The results place stringent limits on all CP-even operators, as they affect mainly the normalisation of the five distributions through either the production cross-section, as for c_{HG}, or the $H \to \gamma\gamma$ branching ratio, as for c_{HW}, c_{HB} and c_{HWB}. The results show that the current $\Delta\phi_{jj}$ measurement can only constrain the $c_{H\widetilde{G}}$ and $c_{H\widetilde{W}}$ coefficients, as the cross-section is dominated by ggF and VBF (which is dominated by WW fusion). In contrast, the very loose limits on $c_{H\widetilde{B}}$ and $c_{H\widetilde{W}B}$ indicate a breakdown of the EFT regime and unitarity constraints, and the lack of sensitivity to these coefficients at the current measurement accuracy. In addition, two-dimensional limits are derived, allowing two Wilson coefficients (a CP-even coefficient and its CP-odd counterpart) to vary simultaneously, using the interference-only cross-section and including the quadratic dimension-6 cross-section, and these are shown in Appendix D.

Table 7: The 95% CL observed limits on the c_{HG}, c_{HW}, c_{HB}, c_{HWB} Wilson coefficients of the SMEFT basis and their CP-odd counterparts using interference-only terms and using both the interference and quadratic terms. Limits are derived by fitting one Wilson coefficient at a time while setting the other coefficients to zero. The limits are computed at a new-physics scale $\Lambda = 1$ TeV.

Coefficient	95% CL, interference-only terms	95% CL, interference and quadratic terms
c_{HG}	$[-6.1, 11.0] \times 10^{-3}$	$[-6.5, 10.2] \times 10^{-3}$
$c_{H\widetilde{G}}$	$[-0.12, 0.23]$	$[-3.1, 3.5] \times 10^{-2}$
c_{HW}	$[-1.9, 0.9] \times 10^{-2}$	$[-1.8, 1.0] \times 10^{-2} \cup [0.28, 0.30]$
$c_{H\widetilde{W}}$	$[-10.2, 5.2]$	$[-7.3, 7.3] \times 10^{-2}$
c_{HB}	$[-5.8, 2.8] \times 10^{-3}$	$[-5.5, 3.0] \times 10^{-3} \cup [8.4, 9.3] \times 10^{-2}$
$c_{H\widetilde{B}}$	$[-21.8, 5.7] \times 10^{2}$	$[-2.3, 2.3] \times 10^{-2}$
c_{HWB}	$[-5.2, 10.7] \times 10^{-3}$	$[-0.17, -0.15] \cup [-5.5, 9.8] \times 10^{-3}$
$c_{H\widetilde{W}B}$	$[-2.5, 4.0] \times 10^{2}$	$[-4.0, 4.0] \times 10^{-2}$

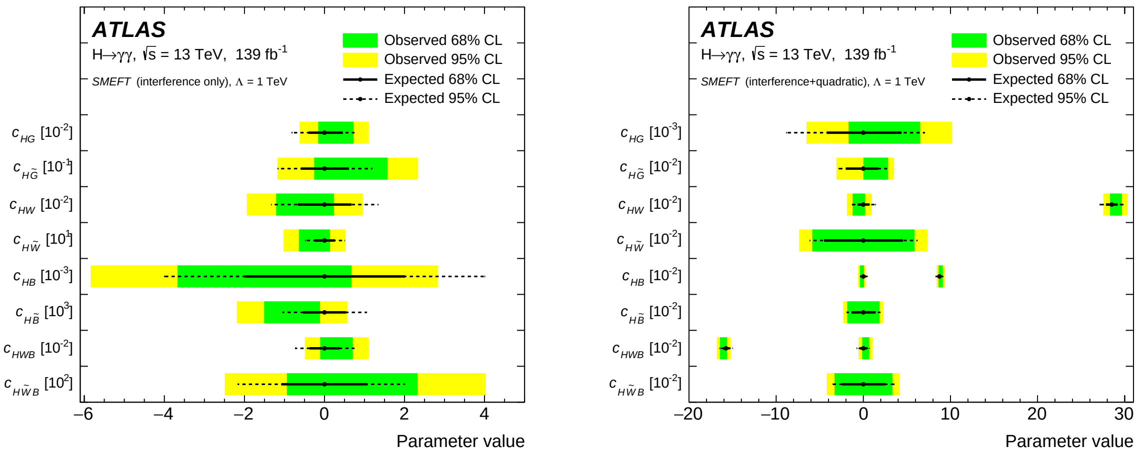

(a)

(b)

Figure 21: Observed and expected 68% and 95% CL limits on SMEFT Wilson coefficients using (a) SM and dimension-6 operators interference-only terms and (b) including quadratic dimension-6 terms. Limits are derived by fitting one Wilson coefficient at a time while setting the other coefficients to zero. The limits are computed at a new-physics scale $\Lambda = 1$ TeV.

10 Summary and conclusions

Measurements of Higgs boson fiducial cross-sections in the diphoton decay channel are performed using pp collision data recorded by the ATLAS experiment at the LHC, assuming the Higgs boson mass to be 125.09 GeV. The data were taken at a centre-of-mass energy of $\sqrt{s} = 13$ TeV and correspond to the full Run 2 data set with an integrated luminosity of 139 fb^{-1}.

The measurements are performed in a diphoton fiducial region requiring two isolated photons with transverse momentum greater than 35% and 25% of the diphoton invariant mass, and with $|\eta| < 2.37$, excluding the region of $1.37 < |\eta| < 1.52$. The inclusive fiducial cross-section times branching ratio is measured to be

$$\sigma_{\text{fid}} = 67 \pm 5\ (\text{stat.}) \pm 4\ (\text{sys.})\ \text{fb},$$

which is in agreement with the Standard Model prediction of 64 ± 4 fb. The measurement has a total relative uncertainty of 10% with nearly equal contributions from the statistical and the systematic uncertainties. The inclusive fiducial cross-section is also extrapolated to the full phase space, leading to a total Higgs production cross-section of 58 ± 4 (stat.) ± 4 (sys.) pb, in agreement with the SM prediction of 55.6 ± 2.7 pb.

In addition, cross-section measurements are reported in various fiducial regions probing Higgs boson production from vector-boson fusion or associated with large missing transverse momentum, leptons or top quarks. The measured cross-sections times branching ratio for the these fiducial regions are:

$$\begin{aligned}
\sigma_{\text{VBF-enhanced}} &= 1.8\ \ \pm 0.5\ \ (\text{stat.}) \pm 0.3\ \ (\text{sys.})\ \text{fb},\\
\sigma_{N_{\text{lepton}\geq 1}} &= 0.81 \pm 0.23\ (\text{stat.}) \pm 0.06\ (\text{sys.})\ \text{fb},\\
\sigma_{\text{High}\ E_{\text{T}}^{\text{miss}}} &= 0.28 \pm 0.27\ (\text{stat.}) \pm 0.07\ (\text{sys.})\ \text{fb},\\
\sigma_{t\bar{t}H\text{-enhanced}} &= 0.53 \pm 0.27\ (\text{stat.}) \pm 0.06\ (\text{sys.})\ \text{fb},
\end{aligned}$$

which show no significant deviation from the Standard Model predictions. The fiducial cross-sections for different inclusive and exclusive jet multiplicities are also measured and compared with different state-of-the-art Standard Model predictions.

Twenty differential cross-sections and four double-differential cross-sections are reported for events belonging to the inclusive diphoton fiducial region, as a function of kinematic variables of the diphoton system or of jets produced in association with the Higgs boson. These cross-sections are sensitive to the different Higgs boson production kinematics, jet kinematics, spin, and CP quantum numbers of the Higgs boson. Among the measured cross-sections is a new measurement of the cross-section in the high Higgs boson transverse momentum region, providing the strongest limits to date for the Higgs boson production cross-section above 450 GeV. The reported cross-sections include new measurements in regions of the phase space probing jet-veto resummation effects. In addition, four differential cross-sections and one double-differential cross-section were measured for events belonging to the VBF-enhanced region, probing VBF kinematics and CP properties. All the measured differential cross-sections are compared with various Standard Model predictions, and do not exhibit significant deviations from them.

The measured differential cross-sections as a function of $p_{\text{T}}^{\gamma\gamma}$ were used to derive limits on the bottom- and charm-quark Yukawa coupling modifiers, κ_b and κ_c. These limits were derived using $p_{\text{T}}^{\gamma\gamma}$ distribution shape and normalisation variations. This analysis sets a 95% CL allowed range $[-3.7,\ 10.4]$ for κ_b, and

[−13.0, 18.9] for κ_c, using only the shape of the $p_T^{\gamma\gamma}$ distribution. More stringent constraints were derived using shape-and-normalisation information.

The strength and tensor structure of the Higgs boson interactions was investigated using five measured differential cross-sections as functions of $p_T^{\gamma\gamma}$, N_{jets}, m_{jj}, $\Delta\phi_{jj}$ and $p_T^{j_1}$ in the effective field theory framework. In this framework, the SM Lagrangian is complemented with additional CP-even and CP-odd dimension-6 operators in the SMEFT Warsaw basis. Given the level of agreement between the measured cross-sections and the SM predictions, stringent limits were placed on the CP-even Wilson coefficients. Looser limits were placed on the CP-odd Wilson coefficients that only cause shape modifications of the CP-sensitive $\Delta\phi_{jj}$ distribution.

Acknowledgements

We thank CERN for the very successful operation of the LHC, as well as the support staff from our institutions without whom ATLAS could not be operated efficiently.

We acknowledge the support of ANPCyT, Argentina; YerPhI, Armenia; ARC, Australia; BMWFW and FWF, Austria; ANAS, Azerbaijan; SSTC, Belarus; CNPq and FAPESP, Brazil; NSERC, NRC and CFI, Canada; CERN; ANID, Chile; CAS, MOST and NSFC, China; Minciencias, Colombia; MEYS CR, Czech Republic; DNRF and DNSRC, Denmark; IN2P3-CNRS and CEA-DRF/IRFU, France; SRNSFG, Georgia; BMBF, HGF and MPG, Germany; GSRI, Greece; RGC and Hong Kong SAR, China; ISF and Benoziyo Center, Israel; INFN, Italy; MEXT and JSPS, Japan; CNRST, Morocco; NWO, Netherlands; RCN, Norway; MEiN, Poland; FCT, Portugal; MNE/IFA, Romania; JINR; MES of Russia and NRC KI, Russian Federation; MESTD, Serbia; MSSR, Slovakia; ARRS and MIZŠ, Slovenia; DSI/NRF, South Africa; MICINN, Spain; SRC and Wallenberg Foundation, Sweden; SERI, SNSF and Cantons of Bern and Geneva, Switzerland; MOST, Taiwan; TAEK, Turkey; STFC, United Kingdom; DOE and NSF, United States of America. In addition, individual groups and members have received support from BCKDF, CANARIE, Compute Canada and CRC, Canada; COST, ERC, ERDF, Horizon 2020 and Marie Skłodowska-Curie Actions, European Union; Investissements d'Avenir Labex, Investissements d'Avenir Idex and ANR, France; DFG and AvH Foundation, Germany; Herakleitos, Thales and Aristeia programmes co-financed by EU-ESF and the Greek NSRF, Greece; BSF-NSF and GIF, Israel; Norwegian Financial Mechanism 2014-2021, Norway; NCN and NAWA, Poland; La Caixa Banking Foundation, CERCA Programme Generalitat de Catalunya and PROMETEO and GenT Programmes Generalitat Valenciana, Spain; Göran Gustafssons Stiftelse, Sweden; The Royal Society and Leverhulme Trust, United Kingdom.

The crucial computing support from all WLCG partners is acknowledged gratefully, in particular from CERN, the ATLAS Tier-1 facilities at TRIUMF (Canada), NDGF (Denmark, Norway, Sweden), CC-IN2P3 (France), KIT/GridKA (Germany), INFN-CNAF (Italy), NL-T1 (Netherlands), PIC (Spain), ASGC (Taiwan), RAL (UK) and BNL (USA), the Tier-2 facilities worldwide and large non-WLCG resource providers. Major contributors of computing resources are listed in Ref. [198].

Appendix

A Correlation matrices for differential cross-section measurements

In this section, the correlation matrices for the differential cross-section measurements presented in Section 8 are shown.

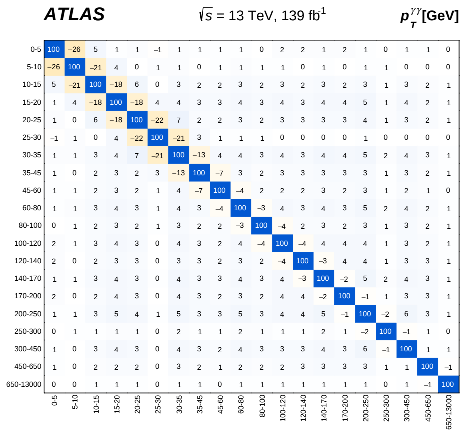

(a)

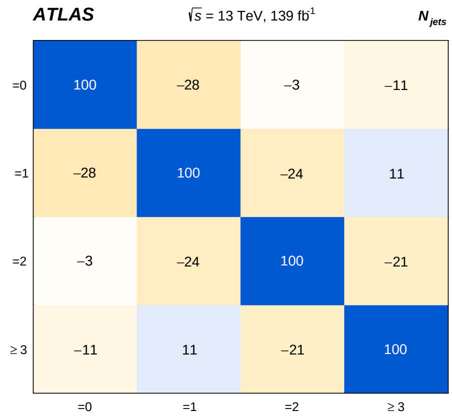

(b)

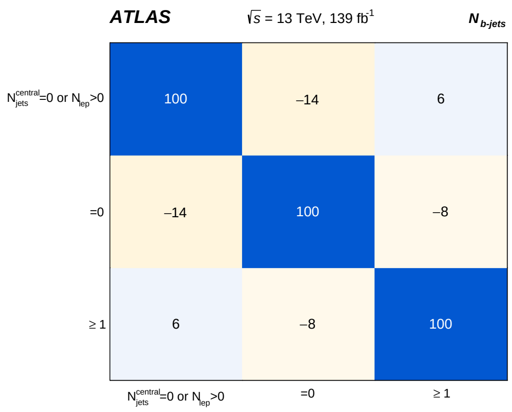

(c)

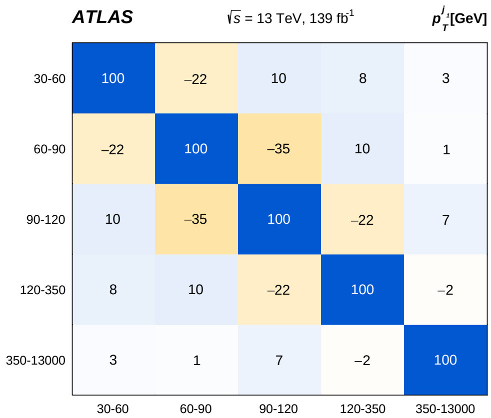

(d)

Figure 22: Correlation matrices for the differential cross-section variables: (a) $p_T^{\gamma\gamma}$, (b) exclusive N_{jets} distributions for all jets with $p_T^j > 30$ GeV, (c) b-jets multiplicity variable $N_{b\text{-jets}}$ (see caption of Figure 10 for more details) and (d) $p_T^{j_1}$.

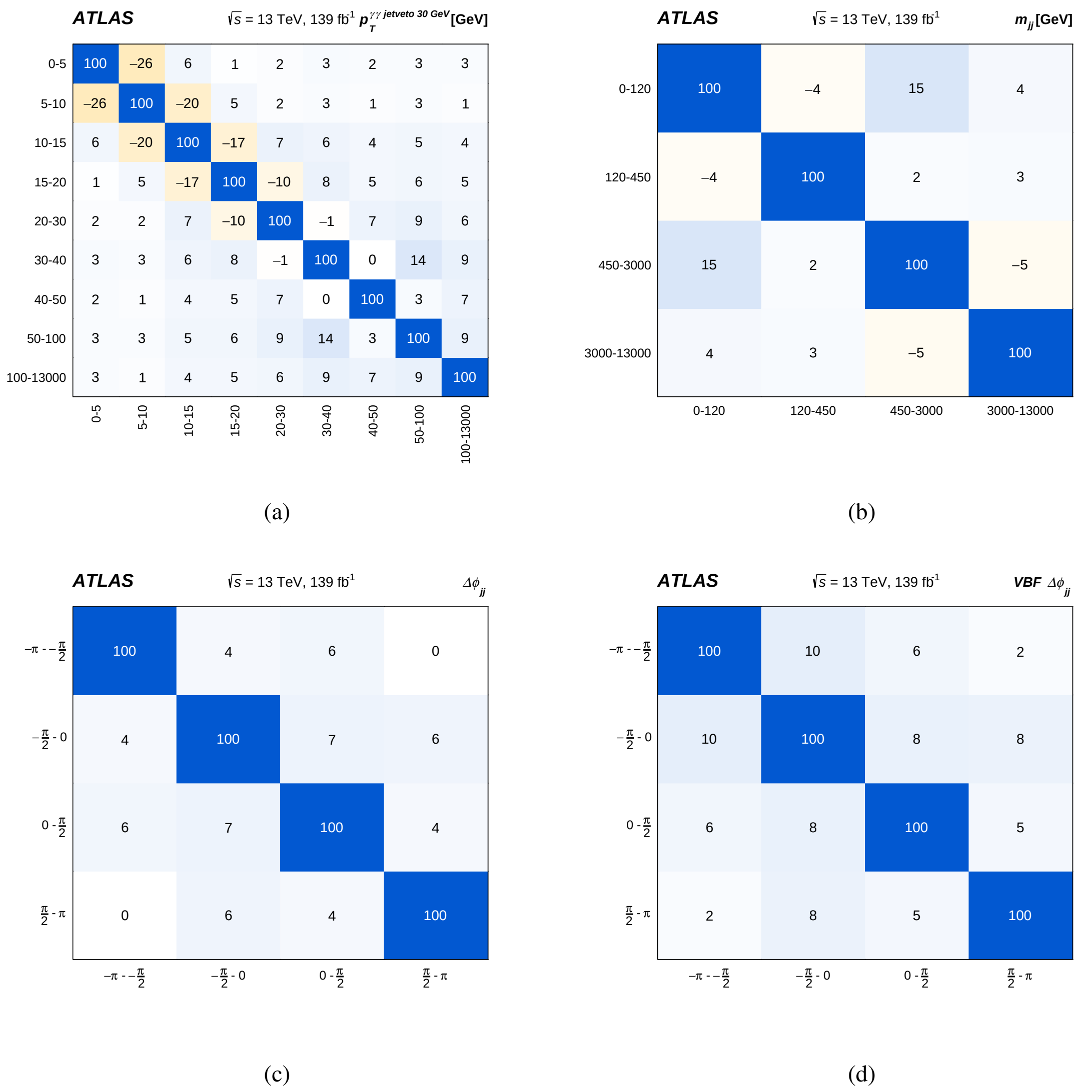

Figure 23: Correlation matrices for the differential cross-sections variables: (a) $p_{\mathrm{T}}^{\gamma\gamma}$ with a 30 GeV jet veto, (b) m_{jj}, (c) $\Delta\phi_{jj}$ and (d) VBF-enhanced $\Delta\phi_{jj}$.

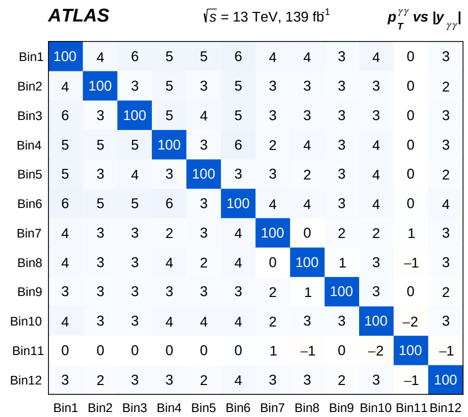

Figure 24: Correlation matrix for the double-differential distribution $p_{\mathrm{T}}^{\gamma\gamma}$ vs $|y_{\gamma\gamma}|$. The order of the bins in the correlation plots is the same as in the plots with the values of the cross-sections.

B Additional differential cross-section measurements

Diphoton kinematics differential cross-sections Figures 25 and 26 show the measured differential cross-sections probing the Higgs kinematic variables: $p_{\mathrm{T}}^{\gamma 1}/m_{\gamma\gamma}$, $p_{\mathrm{T}}^{\gamma 2}/m_{\gamma\gamma}$ and $|y_{\gamma\gamma}|$. The measurements are statistically limited, and show good agreement between data and the default simulation, with shape differences at the higher ends of $p_{\mathrm{T}}^{\gamma 1}/m_{\gamma\gamma}$ and $p_{\mathrm{T}}^{\gamma 2}/m_{\gamma\gamma}$ distributions between the additional theoretical predictions and the default simulation. For the $|y_{\gamma\gamma}|$ distribution, similarly good agreement is observed in the full range.

≥ 1-jet differential cross-sections Figures 27 and 28 show the measured differential cross-sections for the variables: $m_{\gamma\gamma j}$, $p_{\mathrm{T}}^{\gamma\gamma j}$ and H_{T}. Figure 29 shows the variables $\tau_{C,j1}$ and $\sum \tau_{C,j}$. Figures 30 and 31 show $p_{\mathrm{T}}^{\gamma\gamma}$ with different jet vetoes. All predictions agree well with the data within uncertainties for the different predictions.

≥ 2-jet differential cross-sections Figure 32 shows the differential cross-section for the variables $\pi - |\Delta\phi_{\gamma\gamma,jj}|$ and $p_{\mathrm{T},\gamma\gamma jj}$.

Double-differential cross-sections Figures 33 and 34 show the double-differential cross-sections for the variables: $p_{\mathrm{T}}^{\gamma\gamma}$ vs $p_{\mathrm{T}}^{\gamma\gamma j}$, $p_{\mathrm{T}}^{\gamma\gamma}$ vs $\tau_{C,j1}$ and $(p_{\mathrm{T}}^{\gamma 1} + p_{\mathrm{T}}^{\gamma 2})/m_{\gamma\gamma}$ vs $(p_{\mathrm{T}}^{\gamma 1} - p_{\mathrm{T}}^{\gamma 2})/m_{\gamma\gamma}$. Overall, good agreement is observed for the double-differential cross-sections for the photon variables, with SCETLIB providing a more accurate description. Slight shape differences between data and the default simulation are observed for some bins in the double-differential cross-sections with an additional jet, namely for $p_{\mathrm{T}}^{\gamma\gamma}$ vs $\tau_{C,j1}$.

Cross-sections in the VBF-enhanced phase space Figures 35 and 36 show the differential cross-sections in the VBF-enhanced phase space for the variables $|\eta^*|$, $p_{\mathrm{T},\gamma\gamma jj}$, and $p_{\mathrm{T}}^{j_1}$, and the double-differential

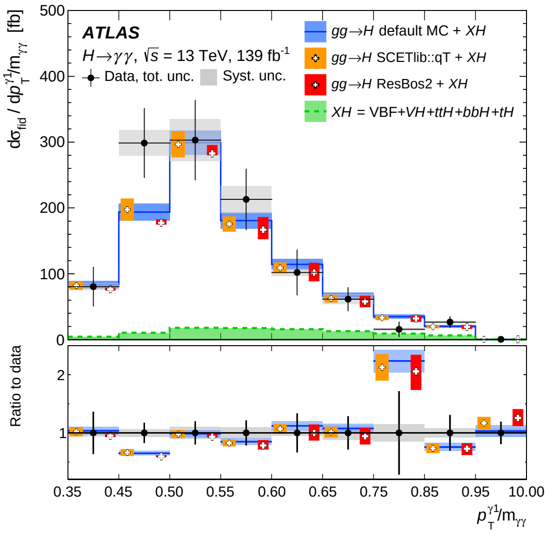

(a)

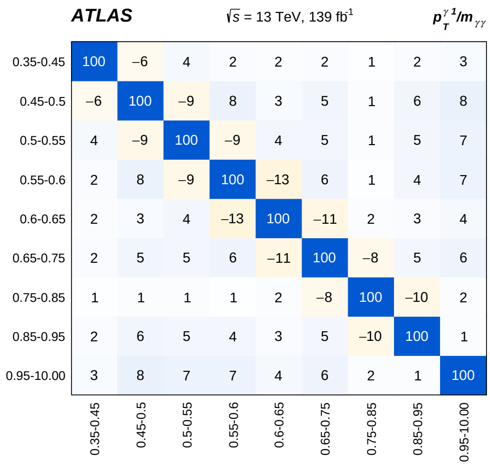

(b)

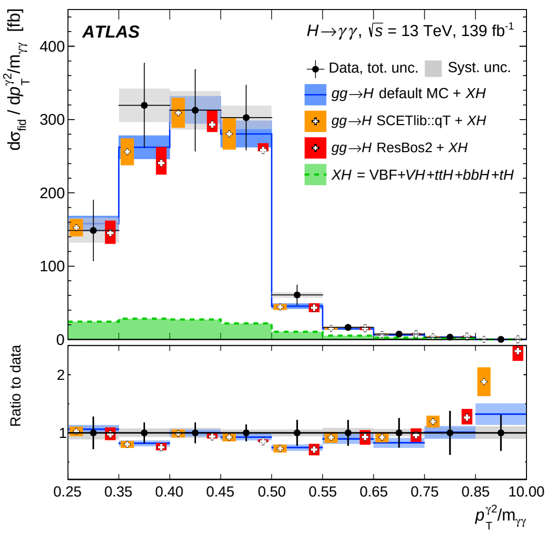

(c)

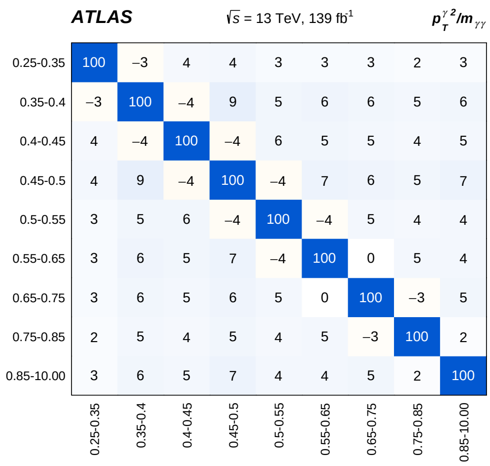

(d)

Figure 25: Particle-level fiducial differential cross-sections times branching ratio for the photon variables (a) $p_{\mathrm{T}}^{\gamma 1}/m_{\gamma\gamma}$ and (c) $p_{\mathrm{T}}^{\gamma 2}/m_{\gamma\gamma}$ together with the corresponding correlation matrices ((b) and (d)).

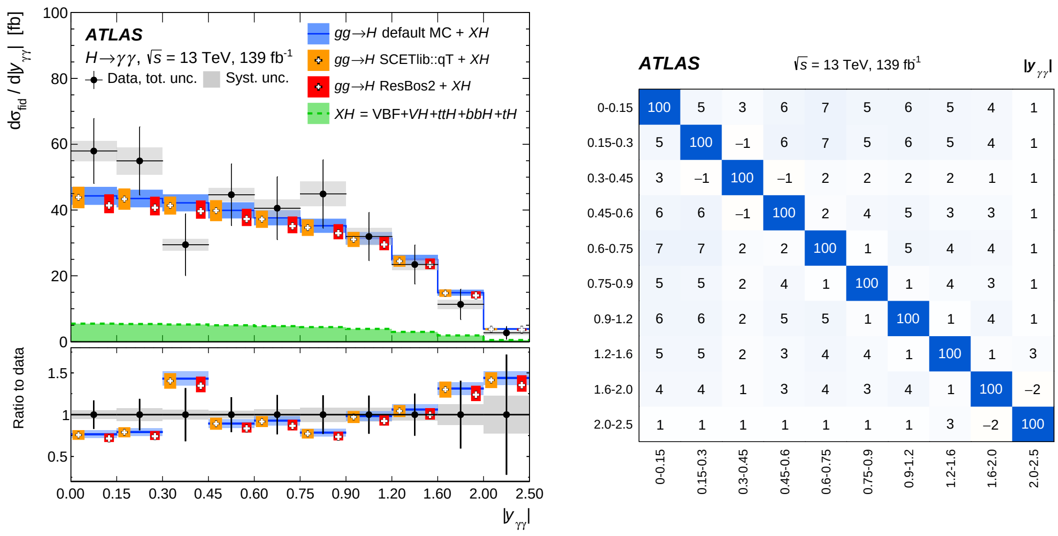

(a) (b)

Figure 26: (a) Particle-level fiducial differential cross-sections times branching ratio for the diphoton rapidity $|y_{\gamma\gamma}|$ together with (b) the corresponding correlation matrix.

cross-section for $p_{\mathrm{T}}^{j_1}$ vs $\Delta\phi_{jj}$ The coarser binning for these measurements reflects the current statistical precision in the VBF-enhanced region.

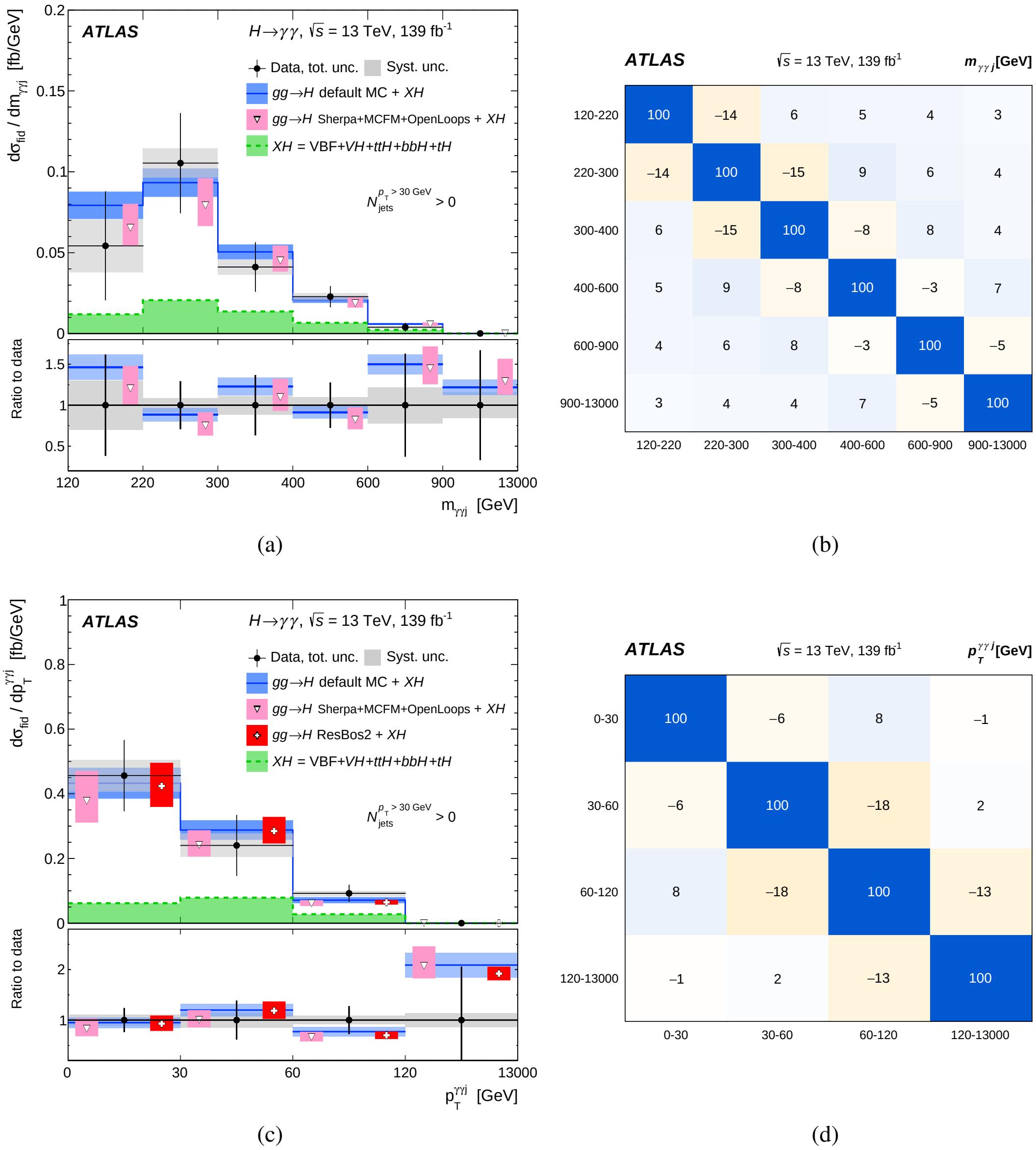

Figure 27: Particle-level fiducial differential cross-sections times branching ratio for the variables: (a) $m_{\gamma\gamma j}$ and (c) $p_{\mathrm{T}}^{\gamma\gamma j}$ together with the corresponding correlation matrices ((b) and (d)).

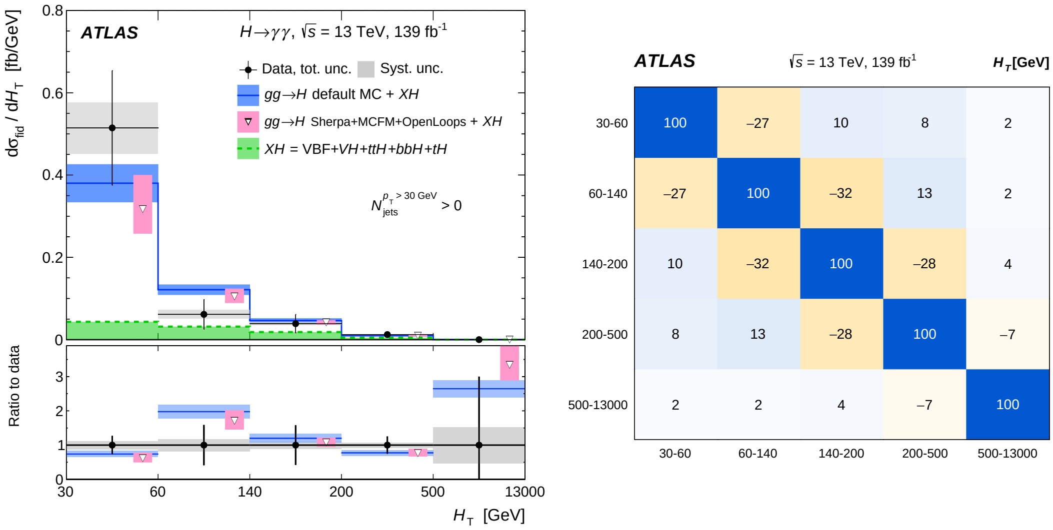

(a) (b)

Figure 28: Particle-level fiducial differential cross-sections times branching ratio for (a) H_{T} together with the corresponding correlation matrix (b).

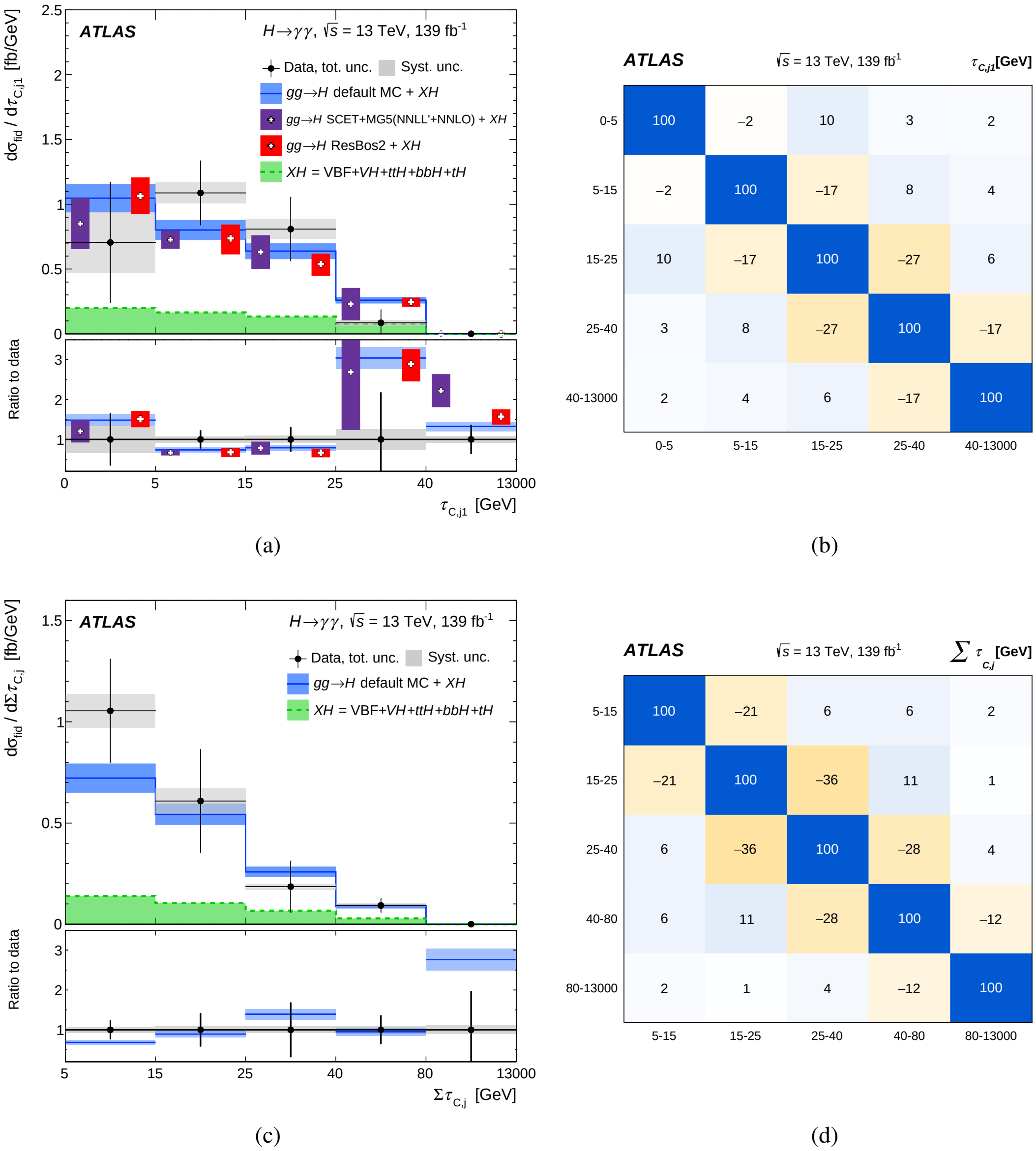

Figure 29: Particle-level fiducial differential cross-sections times branching ratio for the variables: (a) $\tau_{C,j1}$ and (c) $\sum\tau_{C,j}$ together with the corresponding correlation matrices ((b) and (d)).

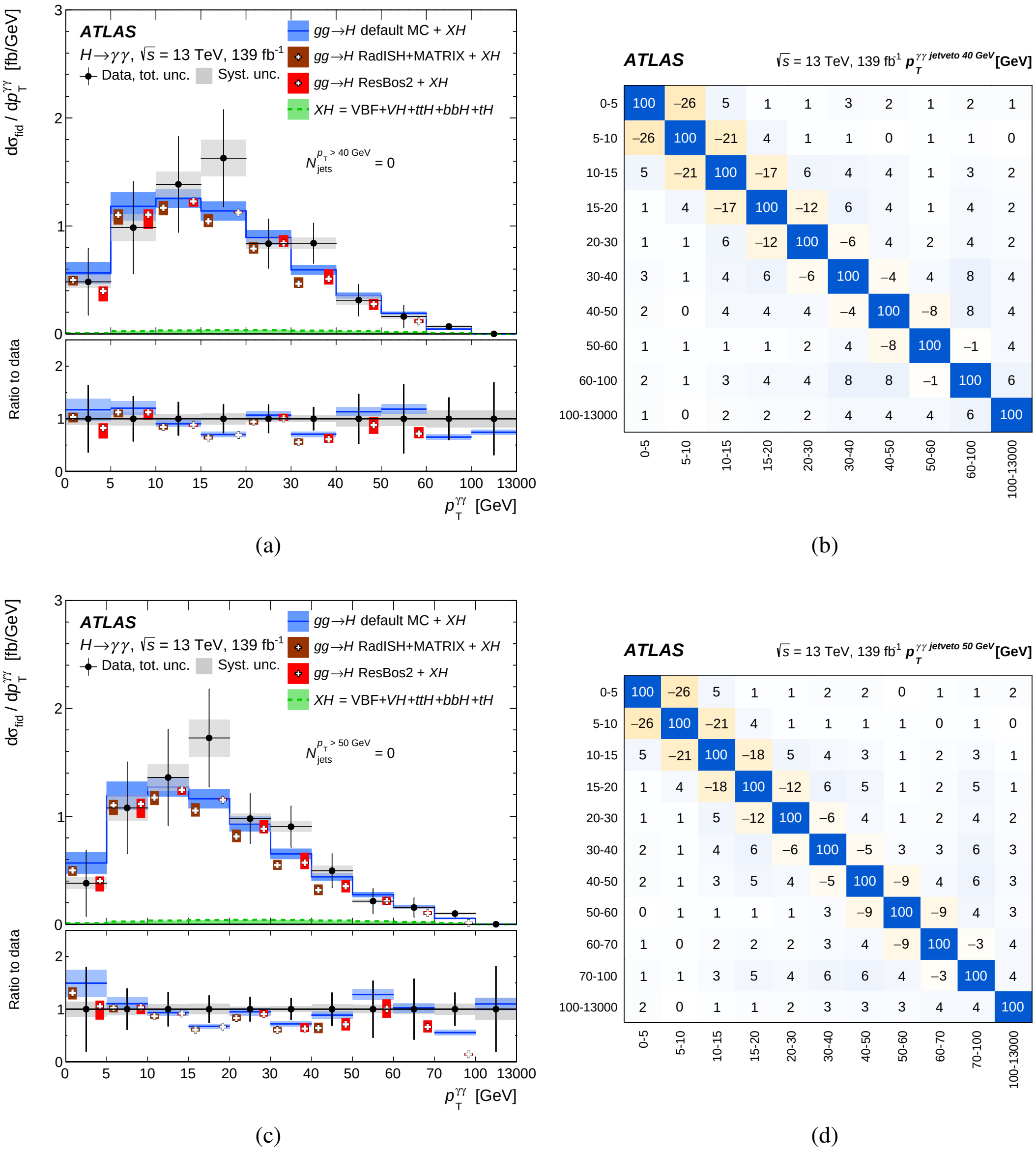

Figure 30: Particle-level fiducial differential cross-sections times branching ratio for $p_T^{\gamma\gamma}$ with a jet veto at (a) 40 GeV and (c) 50 GeV together with the corresponding correlation matrices ((b) and (d)). The ResBos2 predictions are available up to 60 GeV (100 GeV) for $p_T^{\gamma\gamma}$ with a 40 GeV (50 GeV) jet veto. The RadISH+Matrix predictions are available up to 40 GeV (50 GeV) for $p_T^{\gamma\gamma}$ with a 40 GeV (50 GeV) jet veto.

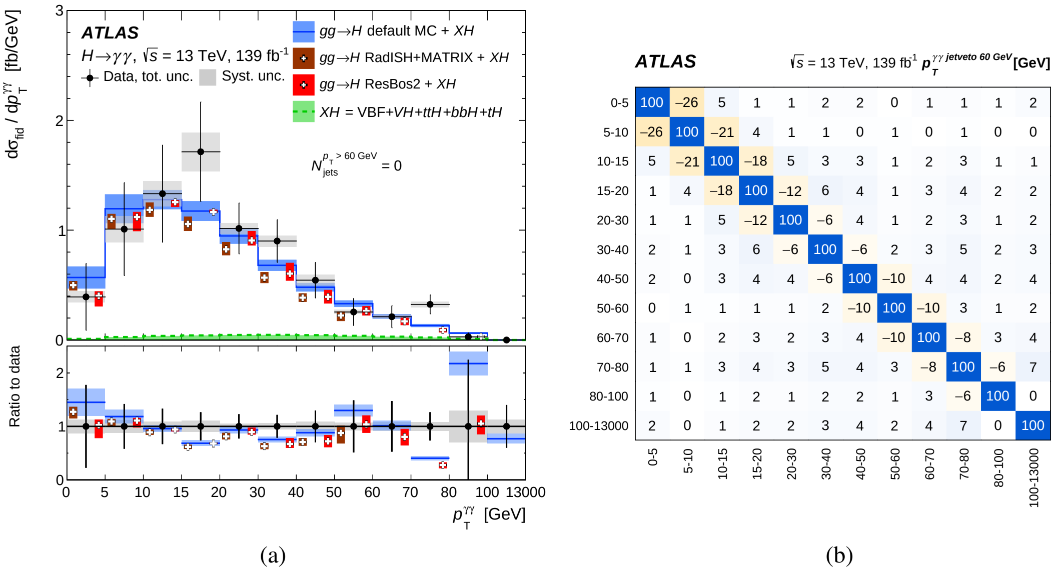

Figure 31: Particle-level fiducial differential cross-sections times branching ratio for $p_{\mathrm{T}}^{\gamma\gamma}$ with a 60 GeV jet veto (a) and the corresponding correlation matrix (b). The ResBos2 predictions are available up to 100 GeV. The RadISH+Matrix predictions are available up to 60 GeV.

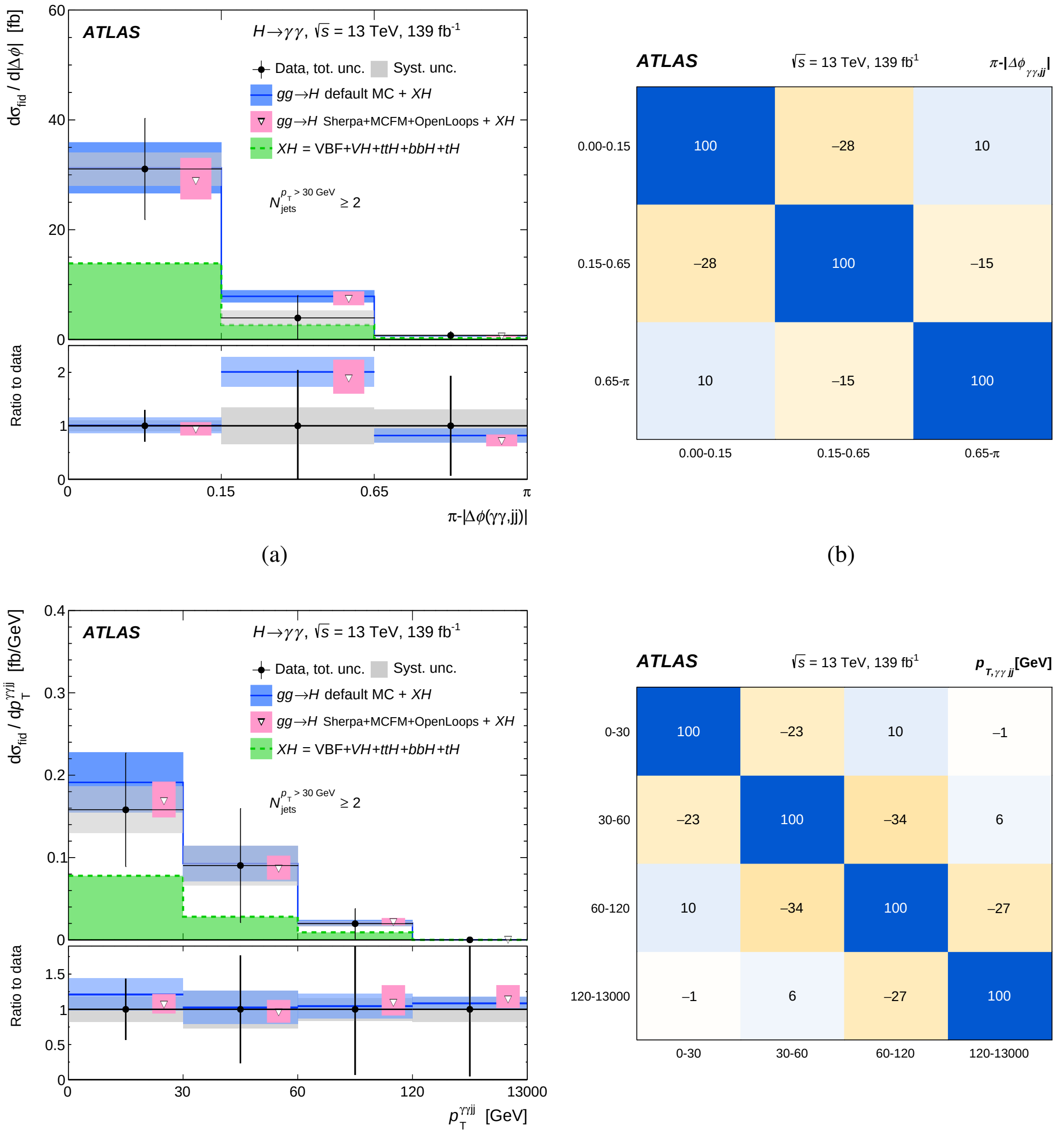

Figure 32: Particle-level fiducial differential cross-sections times branching ratio for the variables (a) $\pi - |\Delta\phi_{\gamma\gamma,jj}|$ and (c) $p_{\mathrm{T},\gamma\gamma jj}$ together with the corresponding correlation matrices ((b) and (d)).

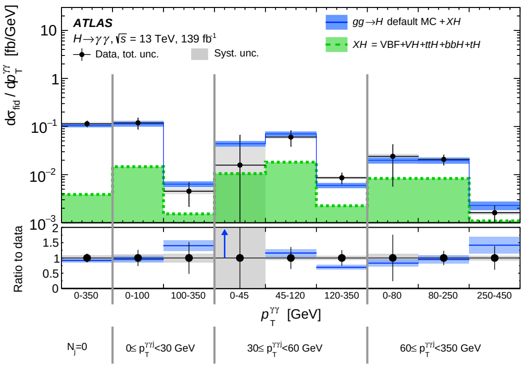

(a)

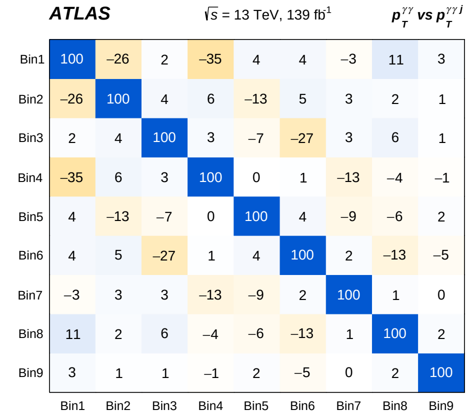

(b)

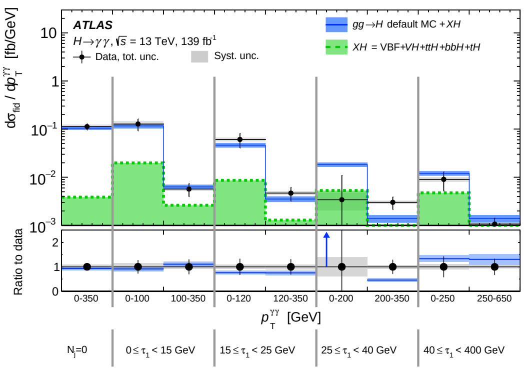

(c)

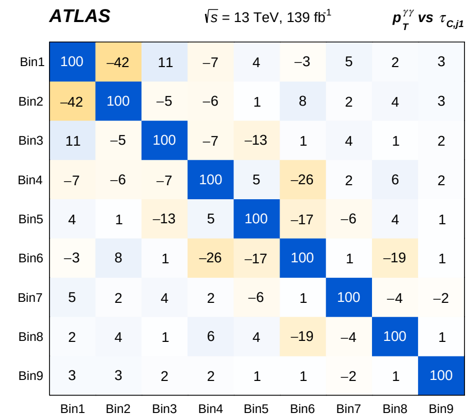

(d)

Figure 33: Double-differential particle-level fiducial cross-sections times branching ratio of (a) $p_T^{\gamma\gamma}$ in bins of $p_T^{\gamma\gamma j}$ and (c) $p_T^{\gamma\gamma}$ in bins $\tau_{C,j1}$ together with the corresponding correlation matrices ((b) and (d)). The first bin corresponds to the case of $N_{\text{jet}} = 0$. The order of the bins in the correlation plots is the same as in the plots with the values of the cross-sections.

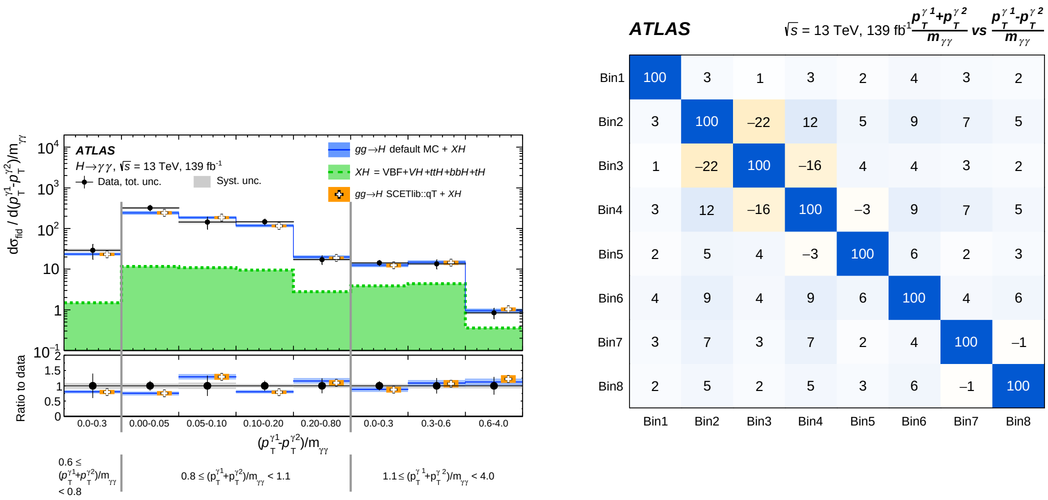

(a) (b)

Figure 34: Double-differential particle-level fiducial cross-sections times branching ratio of (a) $(p_{\mathrm{T}}^{\gamma 1} - p_{\mathrm{T}}^{\gamma 2})/m_{\gamma\gamma}$ in bins of $(p_{\mathrm{T}}^{\gamma 1} + p_{\mathrm{T}}^{\gamma 2})/m_{\gamma\gamma}$ together with the corresponding correlation matrix (b). The order of the bins in the correlation plots is the same as in the plots with the values of the cross-sections.

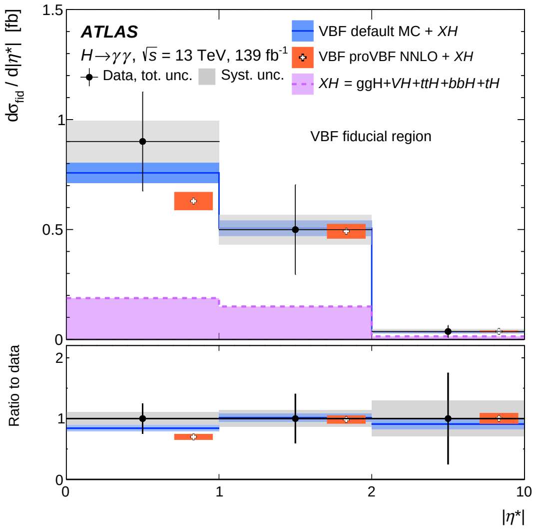

(a)

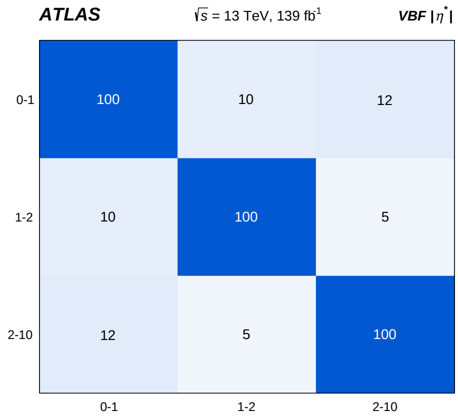

(b)

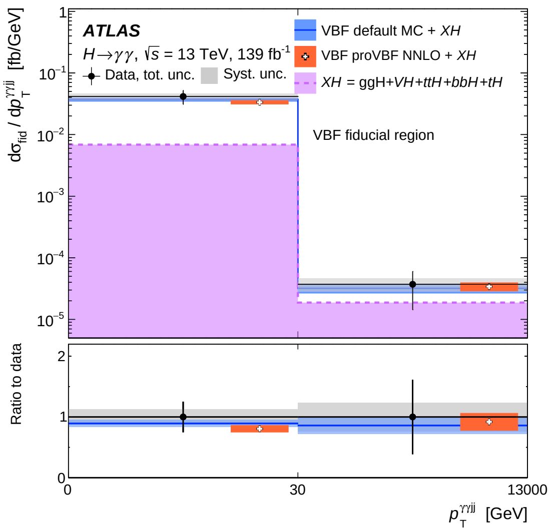

(c)

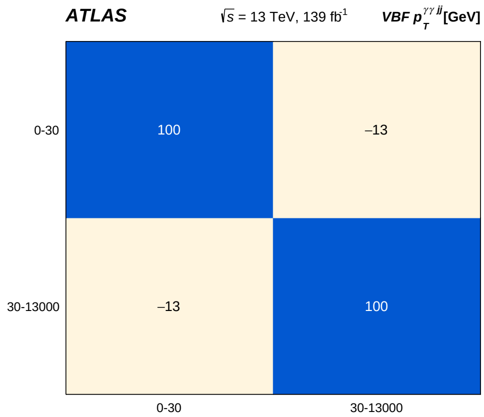

(d)

Figure 35: Particle-level fiducial differential cross-sections times branching ratio for the variables (a) $|\eta^*|$ and (c) $p_{\mathrm{T},\gamma\gamma jj}$ together with the corresponding correlation matrices ((b) and (d)) in the VBF-enhanced fiducial region.

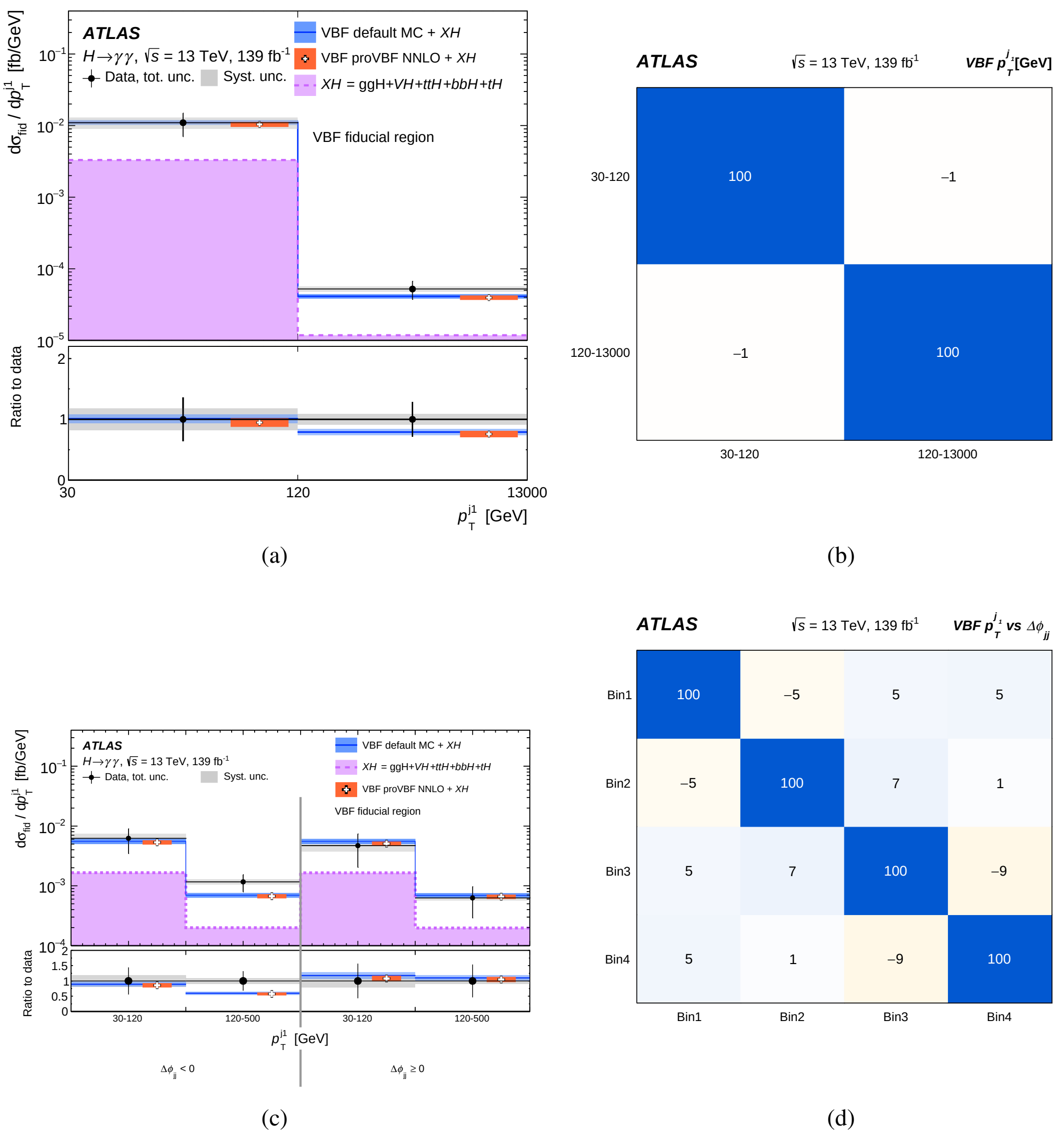

Figure 36: Particle-level fiducial differential cross-section times branching ratio for the variable (a) $p_T^{j_1}$ together with the corresponding correlation matrix in the VBF-enhanced fiducial region (b). Double-differential particle-level fiducial cross-sections times branching ratio of (c) $p_T^{j_1}$ in bins of $\Delta\phi_{jj}$ together with the (d) corresponding correlation matrices in the VBF-enhanced fiducial region. The order of the bins in the correlation plot is the same as in the plot with the values of the cross-sections.

C Uncertainties in additional theory predictions

In this section the uncertainties in the new additional theory predictions are summarised, along with the different scales used to produce them. For the inclusive predictions, the Higgs to diphoton branching ratio uncertainty from Ref. [29] is included.

MATRIX+RadISH predictions These predictions use the NNPDF3.1 PDF [199] set with $\alpha_s(m_Z) = 0.118$. The normalisation and factorisation scales were set to m_H and the resummation scale to $m_H/2$. All scales were varied by a factor of 2 around their central values (but with the restriction $1/2 \leq \mu_r/\mu_f \leq 2$). This calculation was used to predict the fiducial differential cross-sections as a function of the diphoton transverse momentum in events passing a jet veto. The theoretical uncertainty is of the order of 10% for $p_T^H \leq p_T^{JV}$, where p_T^{JV} is the p_T used to define the jet veto.

RadISH+NNLOjet predictions These predictions use the PDF4LHC15NNLO PDF set and the normalisation, factorisation, and resummation scales were set to $m_H/2$. In addition, predictions for $p_T^{j_1}$ are made at NNLL+NNLO QCD accuracy using RadISH+NNLOjet following Refs. [200, 201]. In this case, the results are obtained for a stable Higgs boson and an acceptance correction is applied to account for the fiducial selection. These predictions use the NNPDF3.1 PDF set, the normalisation and factorisation scales were set to m_H and the resummation scale to $m_H/2$. In both cases, all scales were varied by a factor of 2 around the central values (but with the restriction $1/2 \leq \mu_r/\mu_f \leq 2$). In addition, finite top-quark mass corrections derived from the default simulation were applied to the RadISH+NNLOjet predictions.

Sherpa 2.2.11 The Sherpa predictions were produced using the PDF4LHC15NLO PDF set [47]. The uncertainties in the predictions are estimated from the six $1/2 \leq \mu_r, \mu_f \leq 2$ scale variations (with the restriction $1/2 \leq \mu_r/\mu_f \leq 2$) and the 30 PDF eigen-variations.

ResBos2 For the inclusive calculation, the renormalisation and factorisation scales were varied by a factor of 2 around the central value of $m_H/2$ with the usual the restriction $1/2 \leq \mu_r/\mu_f \leq 2$. In addition, the resummation scale is set to be the same as the renormalisation scale. Furthermore, finite top-quark mass corrections derived from the default simulation were applied to the inclusive Higgs production ResBos2 predictions. In the Higgs-plus-jet calculation, the resummation scale is fixed to be the jet transverse momentum as suggested in Ref. [159], and the renormalisation and factorisation scales are varied by a factor of two around the central value of $m_H/2$ (with the restriction $1/2 \leq \mu_r/\mu_f \leq 2$).

SCETlib The predictions are computed using the PDF4LHC15NNLO PDF set. All required contributions for matching to fixed-order NNLO calculations are included directly in SCETlib. The matching to N^{3}LO calculations uses as inputs the known N^{3}LO$_0$ correction to the total inclusive cross-section [202] and existing NNLOjet results for the NNLO$_1$ corrections to the p_T spectrum from Refs. [152, 203].

The top-quark Yukawa coupling y_t^2 contributions at N^{3}LL$'$+N^{3}LO accuracy are computed in the rEFT limit, i.e. in the $m_t \to \infty$ limit rescaled with the exact LO m_t-dependence. This approximation is valid up to around $p_T = 200$ GeV. In addition, SCETlib predictions were provided including the y_t^2, $y_t y_b$, $y_t y_c$, y_b^2, y_c^2, $y_b y_c$ contributions for the $gg \to H$ p_T spectrum to NNLL+NLO accuracy with the exact dependencies on m_t, m_b, m_c, and are used for the bottom- and charm-quark Yukawa coupling interpretations detailed in Section 9.1.

Perturbative uncertainties from several sources were estimated through appropriately chosen variations following Refs. [162, 167, 204]. These include: (i) resummation uncertainties estimated as the maximum envelope of 36 combinations of upward/downward variations of the four involved resummation scales, resulting in a 15% uncertainty for the lowest $p_T^{\gamma\gamma}$ bins, decreasing with increasing $p_T^{\gamma\gamma}$; (ii) a matching uncertainty corresponding to the ambiguity in carrying out the matching to fixed order; (iii) a fixed-order uncertainty which estimates the effect of missing higher-order corrections by varying the overall fixed-order scale μ_{FO} by a factor of 2; this uncertainty dominates for $p_T^{\gamma\gamma} > 45$ GeV and reaches 8%; (iv) a non-perturbative uncertainty due to the sensitivity to non-perturbative effects below $p_T \sim 1$ GeV.

SCETlib predictions for $p_T^{j_1}$ The predictions are made using the PDF4LHC15NNLO PDF set with $\alpha_s(m_Z) = 0.118$. All fiducial requirements are applied when performing the calculation, except for the photon isolation requirement, for which a dedicated correction computed from the full-simulation MC samples is applied.

proVBF predictions The renormalisation and factorisation scale were varied to estimate the residual theoretical uncertainties. A three-point scale variation $\mu_r = \mu_f$ with $\mu_r/\mu_f = \{\frac{1}{2}, 1, 2\}\mu_0$ was used to estimate the uncertainties, where μ_0 is the p_T-dependent scale described in Ref. [171]. The predictions were made using NNPDF3.0 PDF set. Corrections were applied to the predictions to account for the fiducial acceptance corrections obtained from the default simulation.

D Two-dimensional limits on the Effective Field Theory couplings

In addition to the one-dimensional limits on EFT Wilson coefficients presented in Section 9.2, two-dimensional limits are derived, allowing two Wilson coefficients (a CP-even coefficient and its CP-odd counterpart) to vary simultaneously using the interference-only cross-section, shown in Figure 37, and including the quadratic dimension-6 cross-section, shown in Figure 38. The shape difference between the interference-only 2D limits and the interference-plus-quadratic limits is due to the fact that the interference-plus-quadratic cross-section affects the $H \to \gamma\gamma$ branching-ratio for the both CP-even and CP-odd operators. This is represented by the ring shape centred around zero for the CP-odd coefficient in the interference-plus-quadratic limits, since the interference-only cross-section vanishes for inclusive observables. In contrast, the interference-only cross-section for CP-odd operators affects only the shape of the $\Delta\phi_{jj}$ distribution. The 2D limits are compatible with the 1D limits due to the absence of significant correlation between the CP-even and CP-odd operators.

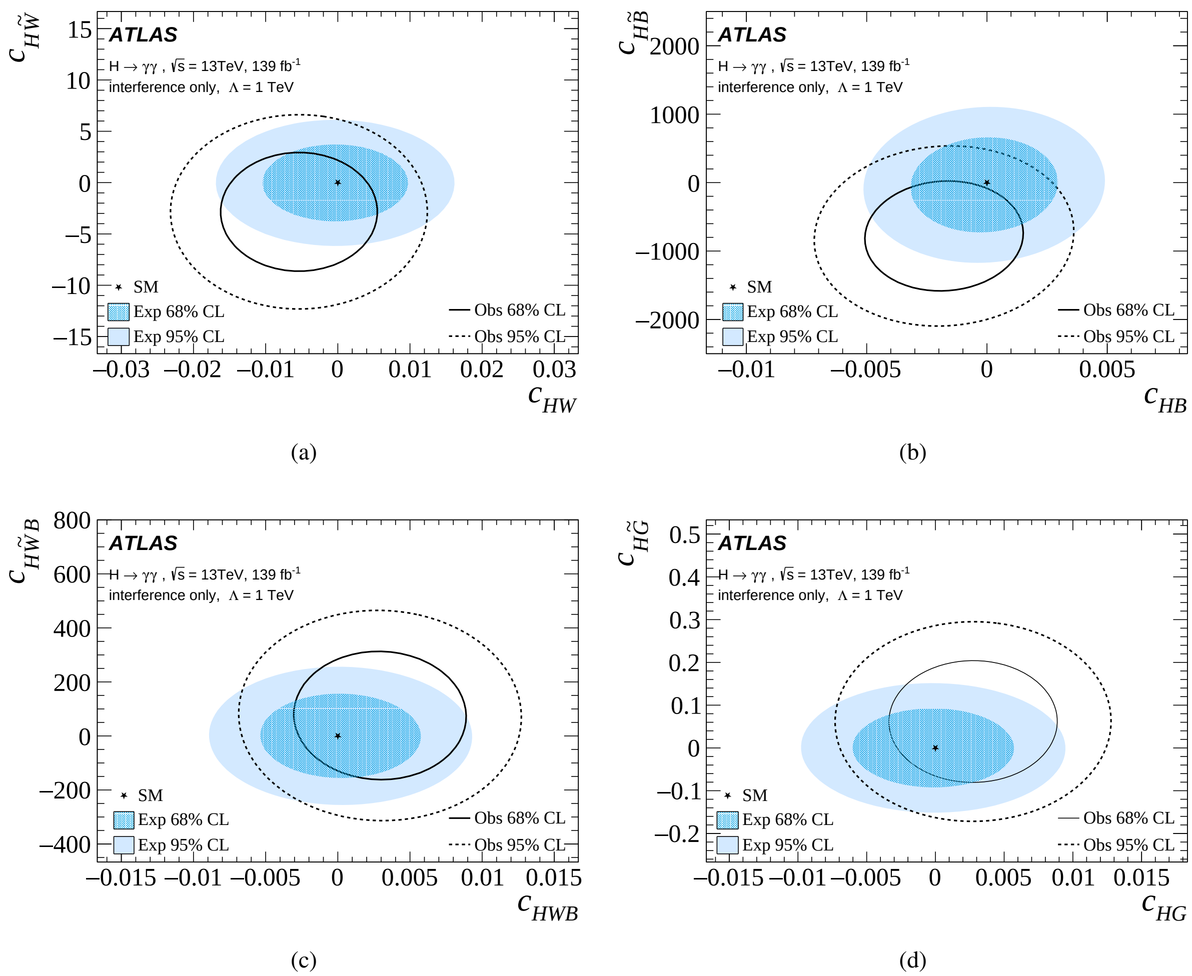

Figure 37: Plots showing the 2D 68% and 95% observed and expected limits obtained from various combinations of two Wilson coefficients using only the SM–dimension-6 interference in the SMEFT basis: (a) c_{HW} vs $c_{H\widetilde{W}}$, (b) c_{HB} vs $c_{H\widetilde{B}}$, (c) c_{HWB} vs $c_{H\widetilde{W}B}$, (d) c_{HG} vs $c_{H\widetilde{G}}$. The limits are computed at a new-physics scale $\Lambda = 1$ TeV.

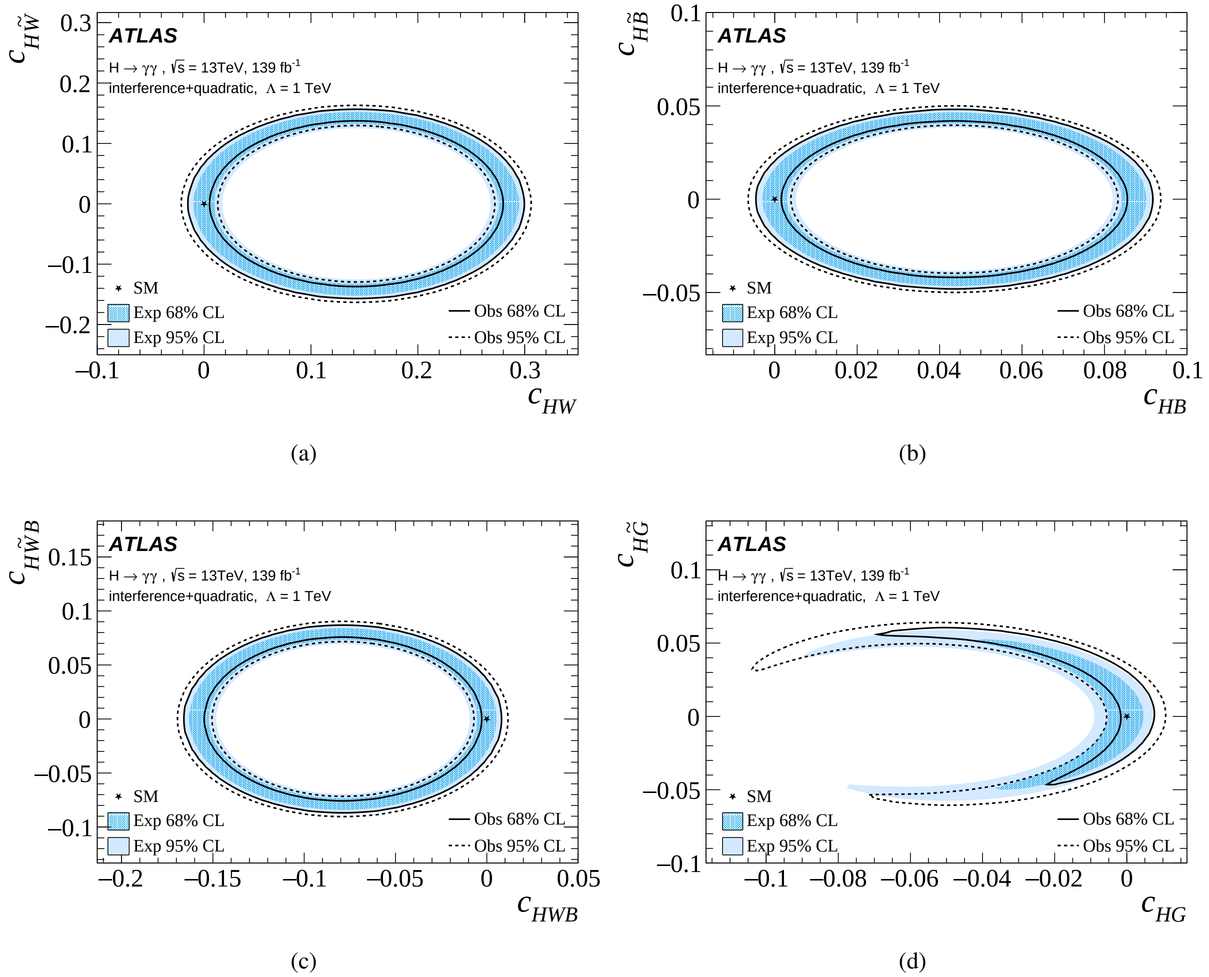

Figure 38: Plots showing the 2D 68% and 95% observed and expected limits obtained from various combinations of two Wilson coefficients including both the SM–dimension-6 interference and the quadratic dimension-6 terms in the SMEFT basis: (a) c_{HW} vs $c_{H\widetilde{W}}$, (b) c_{HB} vs $c_{H\widetilde{B}}$, (c) c_{HWB} vs $c_{H\widetilde{W}B}$, (d) c_{HG} vs $c_{H\widetilde{G}}$. The limits are computed at a new-physics scale $\Lambda = 1$ TeV.

References

[1] ATLAS Collaboration, *Observation of a new particle in the search for the Standard Model Higgs boson with the ATLAS detector at the LHC*, Phys. Lett. B **716** (2012) 1, arXiv: 1207.7214 [hep-ex].

[2] CMS Collaboration, *Observation of a new boson at a mass of 125 GeV with the CMS experiment at the LHC*, Phys. Lett. B **716** (2012) 30, arXiv: 1207.7235 [hep-ex].

[3] ATLAS Collaboration, *Measurements of the Higgs boson production and decay rates and coupling strengths using pp collision data at $\sqrt{s} = 7$ and 8 TeV in the ATLAS experiment*, Eur. Phys. J. C **76** (2016) 6, arXiv: 1507.04548 [hep-ex].

[4] CMS Collaboration, *Precise determination of the mass of the Higgs boson and tests of compatibility of its couplings with the standard model predictions using proton collisions at 7 and 8 TeV*, Eur. Phys. J. C **75** (2015) 212, arXiv: 1412.8662 [hep-ex].

[5] ATLAS and CMS Collaborations, *Measurements of the Higgs boson production and decay rates and constraints on its couplings from a combined ATLAS and CMS analysis of the LHC pp collision data at $\sqrt{s} = 7$ and 8 TeV*, JHEP **08** (2016) 045, arXiv: 1606.02266 [hep-ex].

[6] ATLAS Collaboration, *Measurement of inclusive and differential cross sections in the $H \to ZZ^* \to 4\ell$ decay channel in pp collisions at $\sqrt{s} = 13$ TeV with the ATLAS detector*, JHEP **10** (2017) 132, arXiv: 1708.02810 [hep-ex].

[7] ATLAS Collaboration, *Measurement of the Higgs boson coupling properties in the $H \to ZZ^* \to 4\ell$ decay channel at $\sqrt{s} = 13$ TeV with the ATLAS detector*, JHEP **03** (2018) 095, arXiv: 1712.02304 [hep-ex].

[8] ATLAS Collaboration, *Evidence for the $H \to b\bar{b}$ decay with the ATLAS detector*, JHEP **12** (2017) 024, arXiv: 1708.03299 [hep-ex].

[9] ATLAS Collaboration, *Evidence for the associated production of the Higgs boson and a top quark pair with the ATLAS detector*, Phys. Rev. D **97** (2018) 072003, arXiv: 1712.08891 [hep-ex].

[10] ATLAS and CMS Collaborations, *Combined Measurement of the Higgs Boson Mass in pp Collisions at $\sqrt{s} = 7$ and 8 TeV with the ATLAS and CMS Experiments*, Phys. Rev. Lett. **114** (2015) 191803, arXiv: 1503.07589 [hep-ex].

[11] ATLAS Collaboration, *Measurements of Higgs boson properties in the diphoton decay channel with 36 fb^{-1} of pp collision data at $\sqrt{s} = 13$ TeV with the ATLAS detector*, Phys. Rev. D **98** (2018) 052005, arXiv: 1802.04146 [hep-ex].

[12] CMS Collaboration, *Measurements of properties of the Higgs boson decaying into the four-lepton final state in pp collisions at $\sqrt{s} = 13$ TeV*, JHEP **11** (2017) 047, arXiv: 1706.09936 [hep-ex].

[13] CMS Collaboration, *Constraints on anomalous Higgs boson couplings using production and decay information in the four-lepton final state*, Phys. Lett. B **775** (2017) 1, arXiv: 1707.00541 [hep-ex].

[14] CMS Collaboration, *Measurement and interpretation of differential cross sections for Higgs boson production at $\sqrt{s} = 13$ TeV*, Phys. Lett. B **792** (2019) 369, arXiv: 1812.06504 [hep-ex].

[15] ATLAS Collaboration,
Measurement of the production cross section for a Higgs boson in association with a vector boson in the $H \to WW^* \to \ell\nu\ell\nu$ channel in pp collisions at $\sqrt{s} = 13$ TeV with the ATLAS detector, Phys. Lett. B **798** (2019) 134949, arXiv: 1903.10052 [hep-ex].

[16] ATLAS Collaboration, *Measurement of the four-lepton invariant mass spectrum in 13 TeV proton–proton collisions with the ATLAS detector*, JHEP **04** (2019) 048, arXiv: 1902.05892 [hep-ex].

[17] ATLAS Collaboration, *Cross-section measurements of the Higgs boson decaying into a pair of τ-leptons in proton–proton collisions at $\sqrt{s} = 13$ TeV with the ATLAS detector*, Phys. Rev. D **99** (2019) 072001, arXiv: 1811.08856 [hep-ex].

[18] ATLAS Collaboration, *Measurements of gluon-gluon fusion and vector-boson fusion Higgs boson production cross-sections in the $H \to WW^* \to e\nu\mu\nu$ decay channel in pp collisions at $\sqrt{s} = 13$ TeV with the ATLAS detector*, Phys. Lett. B **789** (2019) 508, arXiv: 1808.09054 [hep-ex].

[19] ATLAS Collaboration,
Observation of $H \to b\bar{b}$ decays and VH production with the ATLAS detector, Phys. Lett. B **786** (2018) 59, arXiv: 1808.08238 [hep-ex].

[20] ATLAS Collaboration, *Constraints on off-shell Higgs boson production and the Higgs boson total width in $ZZ \to 4\ell$ and $ZZ \to 2\ell 2\nu$ final states with the ATLAS detector*, Phys. Lett. B **786** (2018) 223, arXiv: 1808.01191 [hep-ex].

[21] ATLAS Collaboration, *Observation of Higgs boson production in association with a top quark pair at the LHC with the ATLAS detector*, Phys. Lett. B **784** (2018) 173, arXiv: 1806.00425 [hep-ex].

[22] ATLAS Collaboration, *Measurement of the Higgs boson mass in the $H \to ZZ^* \to 4\ell$ and $H \to \gamma\gamma$ channels with $\sqrt{s} = 13$ TeV pp collisions using the ATLAS detector*, Phys. Lett. B **784** (2018) 345, arXiv: 1806.00242 [hep-ex].

[23] ATLAS Collaboration, *Combined measurement of differential and total cross sections in the $H \to \gamma\gamma$ and the $H \to ZZ^* \to 4\ell$ decay channels at $\sqrt{s} = 13$ TeV with the ATLAS detector*, Phys. Lett. B **786** (2018) 114, arXiv: 1805.10197 [hep-ex].

[24] CMS Collaboration, *Measurements of Higgs boson production cross sections and couplings in the diphoton decay channel at $\sqrt{s} = 13$ TeV*, JHEP **07** (2021) 027, arXiv: 2103.06956 [hep-ex].

[25] ATLAS Collaboration, *Measurements of the Higgs boson inclusive and differential fiducial cross sections in the 4ℓ decay channel at $\sqrt{s} = 13$ TeV*, Eur. Phys. J. C **80** (2020) 942, arXiv: 2004.03969 [hep-ex].

[26] ATLAS Collaboration,
Study of the spin and parity of the Higgs boson in diboson decays with the ATLAS detector, Eur. Phys. J. C **75** (2015) 476, arXiv: 1506.05669 [hep-ex], Erratum: Eur. Phys. J. C **76** (2016) 152.

[27] CMS Collaboration, *Constraints on the spin-parity and anomalous HVV couplings of the Higgs boson in proton collisions at 7 and 8 TeV*, Phys. Rev. D **92** (2015) 012004, arXiv: 1411.3441 [hep-ex].

[28] ATLAS and CMS Collaborations, *Combined Measurement of the Higgs Boson Mass in pp Collisions at $\sqrt{s} = 7$ and 8 TeV with the ATLAS and CMS Experiments*, Phys. Rev. Lett. **114** (2015) 191803, arXiv: 1503.07589 [hep-ex].

[29] D. de Florian et al., *Handbook of LHC Higgs Cross Sections: 4. Deciphering the Nature of the Higgs Sector*, (2016), arXiv: 1610.07922 [hep-ph].

[30] ATLAS Collaboration, *Measurements of fiducial and differential cross sections for Higgs boson production in the diphoton decay channel at $\sqrt{s} = 8$ TeV with ATLAS*, JHEP **09** (2014) 112, arXiv: 1407.4222 [hep-ex].

[31] ATLAS Collaboration, *The ATLAS Experiment at the CERN Large Hadron Collider*, JINST **3** (2008) S08003.

[32] ATLAS Collaboration, *ATLAS Insertable B-Layer Technical Design Report*, ATLAS-TDR-19; CERN-LHCC-2010-013, 2010, URL: https://cds.cern.ch/record/1291633, Addendum: ATLAS-TDR-19-ADD-1; CERN-LHCC-2012-009, 2012, URL: https://cds.cern.ch/record/1451888.

[33] B. Abbott et al., *Production and integration of the ATLAS Insertable B-Layer*, JINST **13** (2018) T05008, arXiv: 1803.00844 [physics.ins-det].

[34] ATLAS Collaboration, *Performance of the ATLAS trigger system in 2015*, Eur. Phys. J. C **77** (2017) 317, arXiv: 1611.09661 [hep-ex].

[35] ATLAS Collaboration, *The ATLAS Collaboration Software and Firmware*, ATL-SOFT-PUB-2021-001, 2021, URL: https://cds.cern.ch/record/2767187.

[36] ATLAS Collaboration, *ATLAS data quality operations and performance for 2015–2018 data-taking*, JINST **15** (2020) P04003, arXiv: 1911.04632 [physics.ins-det].

[37] ATLAS Collaboration, *Performance of electron and photon triggers in ATLAS during LHC Run 2*, Eur. Phys. J. C **80** (2020) 47, arXiv: 1909.00761 [hep-ex].

[38] A. Djouadi, J. Kalinowski and M. Spira, *HDECAY: A program for Higgs boson decays in the Standard Model and its supersymmetric extension*, Comput. Phys. Commun. **108** (1998) 56, arXiv: hep-ph/9704448.

[39] M. Spira, *QCD Effects in Higgs Physics*, Fortsch. Phys. **46** (1998) 203, arXiv: hep-ph/9705337.

[40] A. Djouadi, M. M. Mühlleitner and M. Spira, *Decays of Supersymmetric particles: The Program SUSY-HIT (SUspect-SdecaY-Hdecay-InTerface)*, Acta Phys. Polon. B **38** (2007) 635, arXiv: hep-ph/0609292.

[41] A. Bredenstein, A. Denner, S. Dittmaier and M. M. Weber, *Radiative corrections to the semileptonic and hadronic Higgs-boson decays $H \to WW/ZZ \to 4$ fermions*, JHEP **02** (2007) 080, arXiv: hep-ph/0611234.

[42] A. Bredenstein, A. Denner, S. Dittmaier and M. M. Weber, *Precise predictions for the Higgs-boson decay $H \to WW/ZZ \to 4$ leptons*, Phys. Rev. D **74** (2006) 013004, arXiv: hep-ph/0604011 [hep-ph].

[43] A. Bredenstein, A. Denner, S. Dittmaier and M. M. Weber, *Precision calculations for the Higgs decays $H \to ZZ/WW \to 4$ leptons*, Nucl. Phys. Proc. Suppl. **160** (2006) 131, arXiv: hep-ph/0607060 [hep-ph].

[44] S. Alioli, P. Nason, C. Oleari and E. Re, *A general framework for implementing NLO calculations in shower Monte Carlo programs: the POWHEG BOX*, JHEP **06** (2010) 043, arXiv: 1002.2581 [hep-ph].

[45] P. Nason, *A new method for combining NLO QCD with shower Monte Carlo algorithms*, JHEP **11** (2004) 040, arXiv: hep-ph/0409146.

[46] S. Frixione, P. Nason and C. Oleari, *Matching NLO QCD computations with parton shower simulations: the POWHEG method*, JHEP **11** (2007) 070, arXiv: 0709.2092 [hep-ph].

[47] J. Butterworth et al., *PDF4LHC recommendations for LHC Run II*, J. Phys. G **43** (2016) 023001, arXiv: 1510.03865 [hep-ph].

[48] J. Alwall et al., *The automated computation of tree-level and next-to-leading order differential cross sections, and their matching to parton shower simulations*, JHEP **07** (2014) 079, arXiv: 1405.0301 [hep-ph].

[49] T. Sjöstrand et al., *An introduction to PYTHIA 8.2*, Comput. Phys. Commun. **191** (2015) 159, arXiv: 1410.3012 [hep-ph].

[50] ATLAS Collaboration, *Measurement of the Z/γ^* boson transverse momentum distribution in pp collisions at $\sqrt{s}$ = 7 TeV with the ATLAS detector*, JHEP **09** (2014) 145, arXiv: 1406.3660 [hep-ex].

[51] ATLAS Collaboration, *ATLAS Pythia 8 tunes to 7 TeV data*, ATL-PHYS-PUB-2014-021, 2014, URL: https://cds.cern.ch/record/1966419.

[52] K. Hamilton, P. Nason, E. Re and G. Zanderighi, *NNLOPS simulation of Higgs boson production*, JHEP **10** (2013) 222, arXiv: 1309.0017 [hep-ph].

[53] K. Hamilton, P. Nason and G. Zanderighi, *Finite quark-mass effects in the NNLOPS POWHEG+MiNLO Higgs generator*, JHEP **05** (2015) 140, arXiv: 1501.04637 [hep-ph].

[54] K. Hamilton, P. Nason and G. Zanderighi, *MINLO: multi-scale improved NLO*, JHEP **10** (2012) 155, arXiv: 1206.3572 [hep-ph].

[55] J. M. Campbell et al., *NLO Higgs boson production plus one and two jets using the POWHEG BOX, MadGraph4 and MCFM*, JHEP **07** (2012) 092, arXiv: 1202.5475 [hep-ph].

[56] K. Hamilton, P. Nason, C. Oleari and G. Zanderighi, *Merging H/W/Z + 0 and 1 jet at NLO with no merging scale: a path to parton shower + NNLO matching*, JHEP **05** (2013) 082, arXiv: 1212.4504 [hep-ph].

[57] S. Catani and M. Grazzini, *Next-to-Next-to-Leading-Order Subtraction Formalism in Hadron Collisions and its Application to Higgs-boson Production at the Large Hadron Collider*, Phys. Rev. Lett. **98** (2007) 222002, arXiv: hep-ph/0703012 [hep-ph].

[58] C. Anastasiou et al., *High precision determination of the gluon fusion Higgs boson cross-section at the LHC*, JHEP **05** (2016) 058, arXiv: 1602.00695 [hep-ph].

[59] C. Anastasiou, C. Duhr, F. Dulat, F. Herzog and B. Mistlberger, *Higgs Boson Gluon-Fusion Production in QCD at Three Loops*, Phys. Rev. Lett. **114** (2015) 212001, arXiv: 1503.06056 [hep-ph].

[60] F. Dulat, A. Lazopoulos and B. Mistlberger, *iHixs 2 – Inclusive Higgs cross sections*, Comput. Phys. Commun. **233** (2018) 243, arXiv: 1802.00827 [hep-ph].

[61] R. V. Harlander and K. J. Ozeren, *Finite top mass effects for hadronic Higgs production at next-to-next-to-leading order*, JHEP **11** (2009) 088, arXiv: 0909.3420 [hep-ph].

[62] R. V. Harlander and K. J. Ozeren, *Top mass effects in Higgs production at next-to-next-to-leading order QCD: Virtual corrections*, Phys. Lett. B **679** (2009) 467, arXiv: 0907.2997 [hep-ph].

[63] R. V. Harlander, H. Mantler, S. Marzani and K. J. Ozeren, *Higgs production in gluon fusion at next-to-next-to-leading order QCD for finite top mass*, Eur. Phys. J. C **66** (2010) 359, arXiv: 0912.2104 [hep-ph].

[64] A. Pak, M. Rogal and M. Steinhauser, *Finite top quark mass effects in NNLO Higgs boson production at LHC*, JHEP **02** (2010) 025, arXiv: 0911.4662 [hep-ph].

[65] S. Actis, G. Passarino, C. Sturm and S. Uccirati, *NLO electroweak corrections to Higgs boson production at hadron colliders*, Phys. Lett. B **670** (2008) 12, arXiv: 0809.1301 [hep-ph].

[66] S. Actis, G. Passarino, C. Sturm and S. Uccirati, *NNLO computational techniques: The cases $H \to \gamma\gamma$ and $H \to gg$*, Nucl. Phys. B **811** (2009) 182, arXiv: 0809.3667 [hep-ph].

[67] M. Bonetti, K. Melnikov and L. Tancredi, *Higher order corrections to mixed QCD-EW contributions to Higgs boson production in gluon fusion*, Phys. Rev. D **97** (2018) 056017, arXiv: 1801.10403 [hep-ph], Erratum: Phys. Rev. D **97** (2018) 099906.

[68] P. Nason and C. Oleari, *NLO Higgs boson production via vector-boson fusion matched with shower in POWHEG*, JHEP **02** (2010) 037, arXiv: 0911.5299 [hep-ph].

[69] M. Ciccolini, A. Denner and S. Dittmaier, *Strong and Electroweak Corrections to the Production of a Higgs Boson + 2 Jets via Weak Interactions at the Large Hadron Collider*, Phys. Rev. Lett. **99** (2007) 161803, arXiv: 0707.0381 [hep-ph].

[70] M. Ciccolini, A. Denner and S. Dittmaier, *Electroweak and QCD corrections to Higgs production via vector-boson fusion at the CERN LHC*, Phys. Rev. D **77** (2008) 013002, arXiv: 0710.4749 [hep-ph].

[71] P. Bolzoni, F. Maltoni, S.-O. Moch and M. Zaro, *Higgs Boson Production via Vector-Boson Fusion at Next-to-Next-to-Leading Order in QCD*, Phys. Rev. Lett. **105** (2010) 011801, arXiv: 1003.4451 [hep-ph].

[72] M. L. Ciccolini, S. Dittmaier and M. Krämer, *Electroweak radiative corrections to associated WH and ZH production at hadron colliders*, Phys. Rev. D **68** (2003) 073003, arXiv: hep-ph/0306234 [hep-ph].

[73] O. Brein, A. Djouadi and R. Harlander, *NNLO QCD corrections to the Higgs-strahlung processes at hadron colliders*, Phys. Lett. B **579** (2004) 149, arXiv: hep-ph/0307206.

[74] O. Brein, R. Harlander, M. Wiesemann and T. Zirke,
Top-quark mediated effects in hadronic Higgs-Strahlung, Eur. Phys. J. C **72** (2012) 1868,
arXiv: 1111.0761 [hep-ph].

[75] L. Altenkamp, S. Dittmaier, R. V. Harlander, H. Rzehak and T. J. E. Zirke,
Gluon-induced Higgs-strahlung at next-to-leading order QCD, JHEP **02** (2013) 078,
arXiv: 1211.5015 [hep-ph].

[76] A. Denner, S. Dittmaier, S. Kallweit and A. Mück, *HAWK 2.0: A Monte Carlo program for Higgs production in vector-boson fusion and Higgs strahlung at hadron colliders*,
Comput. Phys. Commun. **195** (2015) 161, arXiv: 1412.5390 [hep-ph].

[77] O. Brein, R. V. Harlander and T. J. E. Zirke, *vh@nnlo – Higgs Strahlung at hadron colliders*,
Comput. Phys. Commun. **184** (2013) 998, arXiv: 1210.5347 [hep-ph].

[78] R. V. Harlander, A. Kulesza, V. Theeuwes and T. Zirke,
Soft gluon resummation for gluon-induced Higgs Strahlung, JHEP **11** (2014) 082,
arXiv: 1410.0217 [hep-ph].

[79] S. Frixione, G. Ridolfi and P. Nason,
A positive-weight next-to-leading-order Monte Carlo for heavy flavour hadroproduction,
JHEP **09** (2007) 126, arXiv: 0707.3088 [hep-ph].

[80] H. B. Hartanto, B. Jäger, L. Reina and D. Wackeroth,
Higgs boson production in association with top quarks in the POWHEG BOX,
Phys. Rev. D **91** (2015) 094003, arXiv: 1501.04498 [hep-ph].

[81] D. J. Lange, *The EvtGen particle decay simulation package*,
Nucl. Instrum. Meth. A **462** (2001) 152.

[82] S. Frixione, E. Laenen, P. Motylinski, C. White and B. R. Webber,
Single-top hadroproduction in association with a W boson, JHEP **07** (2008) 029,
arXiv: 0805.3067 [hep-ph].

[83] F. Demartin, B. Maier, F. Maltoni, K. Mawatari and M. Zaro,
tWH associated production at the LHC, Eur. Phys. J. C **77** (2017) 34,
arXiv: 1607.05862 [hep-ph].

[84] W. Beenakker et al., *NLO QCD corrections to $t\bar{t}H$ production in hadron collisions*,
Nucl. Phys. B **653** (2003) 151, arXiv: hep-ph/0211352.

[85] S. Dawson, C. Jackson, L. H. Orr, L. Reina and D. Wackeroth, *Associated Higgs boson production with top quarks at the CERN Large Hadron Collider: NLO QCD corrections*,
Phys. Rev. D **68** (2003) 034022, arXiv: hep-ph/0305087.

[86] Y. Zhang, W.-G. Ma, R.-Y. Zhang, C. Chen and L. Guo,
QCD NLO and EW NLO corrections to $t\bar{t}H$ production with top quark decays at hadron collider,
Phys. Lett. B **738** (2014) 1, arXiv: 1407.1110 [hep-ph].

[87] S. Frixione, V. Hirschi, D. Pagani, H. S. Shao and M. Zaro,
Weak corrections to Higgs hadroproduction in association with a top-quark pair,
JHEP **09** (2014) 065, arXiv: 1407.0823 [hep-ph].

[88] F. Demartin, F. Maltoni, K. Mawatari and M. Zaro,
Higgs production in association with a single top quark at the LHC, Eur. Phys. J. C **75** (2015) 267,
arXiv: 1504.00611 [hep-ph].

[89] R. D. Ball et al., *Parton distributions for the LHC run II*, JHEP **04** (2015) 040, arXiv: 1410.8849 [hep-ph].

[90] S. Dawson, C. B. Jackson, L. Reina and D. Wackeroth, *Exclusive Higgs boson production with bottom quarks at hadron colliders*, Phys. Rev. D **69** (2004) 074027, arXiv: hep-ph/0311067.

[91] S. Dittmaier, M. Krämer and M. Spira, *Higgs radiation off bottom quarks at the Fermilab Tevatron and the CERN LHC*, Phys. Rev. D **70** (2004) 074010, arXiv: hep-ph/0309204.

[92] R. Harlander, M. Kramer and M. Schumacher, *Bottom-quark associated Higgs-boson production: reconciling the four- and five-flavour scheme approach*, (2011), arXiv: 1112.3478 [hep-ph].

[93] M. Bähr et al., *Herwig++ physics and manual*, Eur. Phys. J. C **58** (2008) 639, arXiv: 0803.0883 [hep-ph].

[94] J. Bellm et al., *Herwig 7.0/Herwig++ 3.0 release note*, Eur. Phys. J. C **76** (2016) 196, arXiv: 1512.01178 [hep-ph].

[95] R. Frederix and S. Frixione, *Merging meets matching in MC@NLO*, JHEP **12** (2012) 061, arXiv: 1209.6215 [hep-ph].

[96] GEANT4 Collaboration, S. Agostinelli et al., *Geant4 – a simulation toolkit*, Nucl. Instrum. Meth. A **506** (2003) 250.

[97] ATLAS Collaboration, *The ATLAS Simulation Infrastructure*, Eur. Phys. J. C **70** (2010) 823, arXiv: 1005.4568 [physics.ins-det].

[98] E. Bothmann et al., *Event generation with Sherpa 2.2*, SciPost Phys. **7** (2019) 034, arXiv: 1905.09127 [hep-ph].

[99] T. Gleisberg and S. Höche, *Comix, a new matrix element generator*, JHEP **12** (2008) 039, arXiv: 0808.3674 [hep-ph].

[100] F. Buccioni et al., *OpenLoops 2*, Eur. Phys. J. C **79** (2019) 866, arXiv: 1907.13071 [hep-ph].

[101] F. Cascioli, P. Maierhöfer and S. Pozzorini, *Scattering Amplitudes with Open Loops*, Phys. Rev. Lett. **108** (2012) 111601, arXiv: 1111.5206 [hep-ph].

[102] A. Denner, S. Dittmaier and L. Hofer, *Collier: A fortran-based complex one-loop library in extended regularizations*, Comput. Phys. Commun. **212** (2017) 220, arXiv: 1604.06792 [hep-ph].

[103] S. Schumann and F. Krauss, *A parton shower algorithm based on Catani–Seymour dipole factorisation*, JHEP **03** (2008) 038, arXiv: 0709.1027 [hep-ph].

[104] S. Höche, F. Krauss, M. Schönherr and F. Siegert, *A critical appraisal of NLO+PS matching methods*, JHEP **09** (2012) 049, arXiv: 1111.1220 [hep-ph].

[105] S. Höche, F. Krauss, M. Schönherr and F. Siegert, *QCD matrix elements + parton showers. The NLO case*, JHEP **04** (2013) 027, arXiv: 1207.5030 [hep-ph].

[106] S. Catani, F. Krauss, B. R. Webber and R. Kuhn, *QCD Matrix Elements + Parton Showers*, JHEP **11** (2001) 063, arXiv: hep-ph/0109231.

[107] S. Höche, F. Krauss, S. Schumann and F. Siegert, *QCD matrix elements and truncated showers*, JHEP **05** (2009) 053, arXiv: 0903.1219 [hep-ph].

[108] F. Siegert, *A practical guide to event generation for prompt photon production with Sherpa*, J. Phys. G **44** (2017) 044007, arXiv: 1611.07226 [hep-ph].

[109] S. Frixione, *Isolated photons in perturbative QCD*, Phys. Lett. B **429** (1998) 369, arXiv: hep-ph/9801442.

[110] ATLAS Collaboration, *Electron and photon reconstruction and performance in ATLAS using a dynamical, topological cell clustering-based approach*, ATL-PHYS-PUB-2017-022, 2017, URL: https://cds.cern.ch/record/2298955.

[111] ATLAS Collaboration, *Electron and photon energy calibration with the ATLAS detector using 2015–2016 LHC proton–proton collision data*, JINST **14** (2019) P03017, arXiv: 1812.03848 [hep-ex].

[112] ATLAS Collaboration, *Measurement of the photon identification efficiencies with the ATLAS detector using LHC Run 2 data collected in 2015 and 2016*, Eur. Phys. J. C **79** (2019) 205, arXiv: 1810.05087 [hep-ex].

[113] M. Cacciari, G. P. Salam and G. Soyez, *The catchment area of jets*, JHEP **04** (2008) 005, arXiv: 0802.1188 [hep-ph].

[114] M. Cacciari, G. P. Salam and S. Sapeta, *On the characterisation of the underlying event*, JHEP **04** (2010) 065, arXiv: 0912.4926 [hep-ph].

[115] ATLAS Collaboration, *Measurement of the photon identification efficiencies with the ATLAS detector using LHC Run-1 data*, Eur. Phys. J. C **76** (2016) 666, arXiv: 1606.01813 [hep-ex].

[116] ATLAS Collaboration, *Measurement of the inclusive isolated prompt photon cross section in pp collisions at $\sqrt{s} = 7$ TeV with the ATLAS detector*, Phys. Rev. D **83** (2011) 052005, arXiv: 1012.4389 [hep-ex].

[117] ATLAS Collaboration, *Electron and photon performance measurements with the ATLAS detector using the 2015–2017 LHC proton–proton collision data*, JINST **14** (2019) P12006, arXiv: 1908.00005 [hep-ex].

[118] ATLAS Collaboration, *Measurement of Higgs boson production in the diphoton decay channel in pp collisions at center-of-mass energies of 7 and 8 TeV with the ATLAS detector*, Phys. Rev. D **90** (2014) 112015, arXiv: 1408.7084 [hep-ex].

[119] M. Cacciari, G. P. Salam and G. Soyez, *The anti-k_t jet clustering algorithm*, JHEP **04** (2008) 063, arXiv: 0802.1189 [hep-ph].

[120] M. Cacciari, G. P. Salam and G. Soyez, *FastJet user manual*, Eur. Phys. J. C **72** (2012) 1896, arXiv: 1111.6097 [hep-ph].

[121] ATLAS Collaboration, *Jet reconstruction and performance using particle flow with the ATLAS Detector*, Eur. Phys. J. C **77** (2017) 466, arXiv: 1703.10485 [hep-ex].

[122] ATLAS Collaboration, *Performance of pile-up mitigation techniques for jets in pp collisions at $\sqrt{s} = 8$ TeV using the ATLAS detector*, Eur. Phys. J. C **76** (2016) 581, arXiv: 1510.03823 [hep-ex].

[123] ATLAS Collaboration, *ATLAS b-jet identification performance and efficiency measurement with $t\bar{t}$ events in pp collisions at $\sqrt{s} = 13$ TeV*, Eur. Phys. J. C **79** (2019) 970, arXiv: 1907.05120 [hep-ex].

[124] ATLAS Collaboration, *Muon reconstruction and identification efficiency in ATLAS using the full Run 2 pp collision data set at $\sqrt{s} = 13$ TeV*, Eur. Phys. J. C **81** (2021) 578, arXiv: 2012.00578 [hep-ex].

[125] ATLAS Collaboration, *Performance of missing transverse momentum reconstruction with the ATLAS detector using proton–proton collisions at $\sqrt{s} = 13$ TeV*, Eur. Phys. J. C **78** (2018) 903, arXiv: 1802.08168 [hep-ex].

[126] F. Bishara, U. Haisch, P. F. Monni and E. Re, *Constraining Light-Quark Yukawa Couplings from Higgs Distributions*, Phys. Rev. Lett. **118** (2017) 121801, arXiv: 1606.09253 [hep-ph].

[127] C. Grojean, E. Salvioni, M. Schlaffer and A. Weiler, *Very boosted Higgs in gluon fusion*, JHEP **05** (2014) 022, arXiv: 1312.3317 [hep-ph].

[128] A. Biekötter, A. Knochel, M. Krämer, D. Liu and F. Riva, *Vices and virtues of Higgs effective field theories at large energy*, Phys. Rev. D **91** (2015) 055029, arXiv: 1406.7320 [hep-ph].

[129] K. Mimasu, V. Sanz and C. Williams, *Higher order QCD predictions for associated Higgs production with anomalous couplings to gauge bosons*, JHEP **08** (2016) 039, arXiv: 1512.02572 [hep-ph].

[130] M. Grazzini, A. Ilnicka, M. Spira and M. Wiesemann, *Modeling BSM effects on the Higgs transverse-momentum spectrum in an EFT approach*, JHEP **03** (2017) 115, arXiv: 1612.00283 [hep-ph].

[131] A. Banfi, A. Bond, A. Martin and V. Sanz, *Digging for top squarks from Higgs data: from signal strengths to differential distributions*, JHEP **11** (2018) 171, arXiv: 1806.05598 [hep-ph].

[132] Y. Soreq, H. X. Zhu and J. Zupan, *Light quark Yukawa couplings from Higgs kinematics*, JHEP **12** (2016) 045, arXiv: 1606.09621 [hep-ph].

[133] I. W. Stewart, F. J. Tackmann and W. J. Waalewijn, *Factorization at the LHC: From parton distribution functions to initial state jets*, Phys. Rev. D **81** (2010) 094035, arXiv: 0910.0467 [hep-ph].

[134] P. F. Monni, L. Rottoli and P. Torrielli, *Higgs Transverse Momentum with a Jet Veto: A Double-Differential Resummation*, Phys. Rev. Lett. **124** (2020) 252001, arXiv: 1909.04704 [hep-ph].

[135] G. Klämke and D. Zeppenfeld, *Higgs plus two jet production via gluon fusion as a signal at the CERN LHC*, JHEP **04** (2007) 052, arXiv: hep-ph/0703202.

[136] T. Plehn, D. L. Rainwater and D. Zeppenfeld, *Determining the Structure of Higgs Couplings at the CERN Large Hadron Collider*, Phys. Rev. Lett. **88** (2002) 051801, arXiv: hep-ph/0105325.

[137] ATLAS Collaboration, *Measurement of the isolated diphoton cross section in pp collisions at $\sqrt{s} = 7$ TeV with the ATLAS detector*, Phys. Rev. D **85** (2012) 012003, arXiv: 1107.0581 [hep-ex].

[138] M. Frate, K. Cranmer, S. Kalia, A. Vandenberg-Rodes and D. Whiteson, *Modeling Smooth Backgrounds and Generic Localized Signals with Gaussian Processes*, (2017), arXiv: 1709.05681 [physics.data-an].

[139] ATLAS Collaboration, *Luminosity determination in pp collisions at $\sqrt{s} = 8$ TeV using the ATLAS detector at the LHC*, Eur. Phys. J. C **76** (2016) 653, arXiv: 1608.03953 [hep-ex].

[140] G. Avoni et al., *The new LUCID-2 detector for luminosity measurement and monitoring in ATLAS*, JINST **13** (2018) P07017.

[141] ATLAS Collaboration, *Evidence for Higgs boson decays to a low-mass dilepton system and a photon in pp collisions at $\sqrt{s} = 13$ TeV with the ATLAS detector*, Phys. Lett. B **819** (2021) 136412, arXiv: 2103.10322 [hep-ex].

[142] ATLAS Collaboration, *Jet energy scale and resolution measured in proton–proton collisions at $\sqrt{s} = 13$ TeV with the ATLAS detector*, Eur. Phys. J. C **81** (2020) 689, arXiv: 2007.02645 [hep-ex].

[143] ATLAS Collaboration, *Measurements of b-jet tagging efficiency with the ATLAS detector using $t\bar{t}$ events at $\sqrt{s} = 13$ TeV*, JHEP **08** (2018) 089, arXiv: 1805.01845 [hep-ex].

[144] ATLAS Collaboration, *Combined measurements of Higgs boson production and decay using up to 80 fb^{-1} of proton–proton collision data at $\sqrt{s} = 13$ TeV collected with the ATLAS experiment*, Phys. Rev. D **101** (2020) 012002, arXiv: 1909.02845 [hep-ex].

[145] S. Kallweit, E. Re, L. Rottoli and M. Wiesemann, *Accurate single- and double-differential resummation of colour-singlet processes with MATRIX+RADISH: W^+W^- production at the LHC*, JHEP **12** (2020) 147, arXiv: 2004.07720 [hep-ph].

[146] M. Grazzini, S. Kallweit and M. Wiesemann, *Fully differential NNLO computations with MATRIX*, Eur. Phys. J. C **78** (2018) 537, arXiv: 1711.06631 [hep-ph].

[147] M. Grazzini, S. Kallweit, D. Rathlev and M. Wiesemann, *Transverse-momentum resummation for vector-boson pair production at NNLL+NNLO*, JHEP **08** (2015) 154, arXiv: 1507.02565 [hep-ph].

[148] P. F. Monni, E. Re and P. Torrielli, *Higgs Transverse-Momentum Resummation in Direct Space*, Phys. Rev. Lett. **116** (2016) 242001, arXiv: 1604.02191 [hep-ph].

[149] W. Bizoń, P. F. Monni, E. Re, L. Rottoli and P. Torrielli, *Momentum-space resummation for transverse observables and the Higgs $p_\perp$ at N^3LL+NNLO*, JHEP **02** (2018) 108, arXiv: 1705.09127 [hep-ph].

[150] X. Chen, J. Cruz-Martinez, T. Gehrmann, E. W. N. Glover and M. Jaquier, *NNLO QCD corrections to Higgs boson production at large transverse momentum*, JHEP **10** (2016) 066, arXiv: 1607.08817 [hep-ph].

[151] X. Chen, T. Gehrmann, E. W. N. Glover and M. Jaquier, *Precise QCD predictions for the production of Higgs + jet final states*, Phys. Lett. B **740** (2015) 147, arXiv: 1408.5325 [hep-ph].

[152] W. Bizoń et al., *Fiducial distributions in Higgs and Drell-Yan production at N^3LL+NNLO*, JHEP **12** (2018) 132, arXiv: 1805.05916 [hep-ph].

[153] E. Re, L. Rottoli and P. Torrielli, *Fiducial Higgs and Drell-Yan distributions at N^3LL'+NNLO with RadISH*, JHEP **09** (2021) 108, arXiv: 2104.07509 [hep-ph].

[154] J. M. Campbell and R. K. Ellis, *MCFM for the Tevatron and the LHC*, Nucl. Phys. B Proc. Suppl. **205-206** (2010) 10, arXiv: 1007.3492 [hep-ph].

[155] C. Balázs and C.-P. Yuan, *Soft gluon effects on lepton pairs at hadron colliders*, Phys. Rev. D **56** (1997) 5558, arXiv: hep-ph/9704258.

[156] J. Wang, C. S. Li, H. T. Li, Z. Li and C.-P. Yuan, *Improved resummation prediction on Higgs boson production at hadron colliders*, Phys. Rev. D **86** (2012) 094026, arXiv: 1205.4311 [hep-ph].

[157] C. J. Glosser and C. R. Schmidt, *Next-to-leading Corrections to the Higgs Boson Transverse Momentum Spectrum in Gluon Fusion*, JHEP **12** (2002) 016, arXiv: hep-ph/0209248.

[158] J. Collins, *Foundations of Perturbative QCD*, vol. 32, Cambridge University Press, 2013, ISBN: 978-1-107-64525-7, 978-1-107-64525-7, 978-0-521-85533-4, 978-1-139-09782-6.

[159] P. Sun, J. Isaacson, C.-P. Yuan and F. Yuan, *Resummation of high order corrections in Higgs boson plus jet production at the LHC*, Phys. Lett. B **769** (2017) 57, arXiv: 1602.08133 [hep-ph].

[160] M. A. Ebert, J. K. L. Michel, F. J. Tackmann et al., *SCETlib: A C++ Package for Numerical Calculations in QCD and Soft-Collinear Effective Theory*, DESY-17-099 (2018), webpage: http://scetlib.desy.de.

[161] G. Billis, B. Dehnadi, M. A. Ebert, J. K. L. Michel and F. J. Tackmann, *Higgs p_T Spectrum and Total Cross Section with Fiducial Cuts at Third Resummed and Fixed Order in QCD*, Phys. Rev. Lett. **127** (7 2021) 072001, arXiv: 2102.08039 [hep-ph].

[162] M. A. Ebert, J. K. Michel, I. W. Stewart and F. J. Tackmann, *Drell-Yan q_T resummation of fiducial power corrections at N^3LL*, JHEP **04** (2021) 102, arXiv: 2006.11382 [hep-ph].

[163] G. Billis, M. A. Ebert, J. K. L. Michel and F. J. Tackmann, *A toolbox for q_T and 0-jettiness subtractions at N^3LO*, Eur. Phys. J. C **136** (2021) 214, arXiv: 1909.00811 [hep-ph].

[164] M. A. Ebert, J. K. L. Michel and F. J. Tackmann, *Resummation improved rapidity spectrum for gluon fusion Higgs production*, JHEP **05** (2017) 088, arXiv: 1702.00794 [hep-ph].

[165] Y. Li and H. X. Zhu, *Bootstrapping Rapidity Anomalous Dimensions for Transverse-Momentum Resummation*, Phys. Rev. Lett. **118** (2017) 022004, arXiv: 1604.01404 [hep-ph].

[166] M. A. Ebert, B. Mistlberger and G. Vita, *Transverse momentum dependent PDFs at N^3LO*, JHEP **09** (2020) 146, arXiv: 2006.05329 [hep-ph].

[167] I. W. Stewart, F. J. Tackmann, J. R. Walsh and S. Zuberi, *Jet p_T resummation in Higgs production at $NNLL' + NNLO$*, Phys. Rev. D **89** (2014) 054001, arXiv: 1307.1808 [hep-ph].

[168] J. K. L. Michel, P. Pietrulewicz and F. J. Tackmann, *Jet veto resummation with jet rapidity cuts*, JHEP **04** (2019) 142, arXiv: 1810.12911 [hep-ph].

[169] S. Gangal, J. R. Gaunt, F. J. Tackmann and E. Vryonidou, *Higgs production at NNLL'+NNLO using rapidity dependent jet vetoes*, JHEP **05** (2020) 054, arXiv: 2003.04323 [hep-ph].

[170] R. Boughezal, X. Liu, F. Petriello, F. J. Tackmann and J. R. Walsh, *Combining resummed Higgs predictions across jet bins*, Phys. Rev. D **89** (2014) 074044, arXiv: 1312.4535 [hep-ph].

[171] M. Cacciari, F. A. Dreyer, A. Karlberg, G. P. Salam and G. Zanderighi, *Fully Differential Vector-Boson-Fusion Higgs Production at Next-to-Next-to-Leading Order*, Phys. Rev. Lett. **115** (2015) 082002, [Erratum: Phys.Rev.Lett. 120, 139901 (2018)].

[172] G. Cullen et al., *Automated one-loop calculations with GoSam*, Eur. Phys. J. C **72** (2012) 1889, arXiv: 1111.2034 [hep-ph].

[173] G. Cullen et al., *GoSam-2.0: a tool for automated one-loop calculations within the Standard Model and beyond*, Eur. Phys. J. C **74** (2014) 3001, arXiv: 1404.7096 [hep-ph].

[174] A. L. Read, *Presentation of search results: the CL_S technique*, J. Phys. G **28** (2002) 2693.

[175] CMS Collaboration, *Inclusive search for highly boosted Higgs bosons decaying to bottom quark-antiquark pairs in proton–proton collisions at $\sqrt{s} = 13$ TeV*, JHEP **12** (2020) 085, arXiv: 2006.13251 [hep-ex].

[176] K. Becker et al., *Precise predictions for boosted Higgs production*, 2021, arXiv: 2005.07762 [hep-ph].

[177] ATLAS Collaboration, *Constraints on Higgs boson production with large transverse momentum using $H \to b\bar{b}$ decays in the ATLAS detector*, (2021), arXiv: 2111.08340 [hep-ex].

[178] CMS Collaboration, *Observation of Higgs Boson Decay to Bottom Quarks*, Phys. Rev. Lett. **121** (2018) 121801, arXiv: 1808.08242 [hep-ex].

[179] ATLAS Collaboration, *Direct constraint on the Higgs–charm coupling from a search for Higgs boson decays into charm quarks with the ATLAS detector*, CERN-EP-2021-251, 2022, arXiv: 2201.11428 [hep-ex].

[180] ATLAS Collaboration, *Searches for exclusive Higgs and Z boson decays into $J/\psi\gamma$, $\psi(2S)\gamma$, and $\Upsilon(nS)\gamma$ at $\sqrt{s} = 13$ TeV with the ATLAS detector*, Phys. Lett. B **786** (2018) 134, arXiv: 1807.00802 [hep-ex].

[181] CMS Collaboration, *A search for the standard model Higgs boson decaying to charm quarks*, JHEP **03** (2020) 131, arXiv: 1912.01662 [hep-ex].

[182] CMS Collaboration, *Combined measurements of Higgs boson couplings in proton–proton collisions at $\sqrt{s} = 13$ TeV*, Eur. Phys. J. C **79** (2019) 421, arXiv: 1809.10733 [hep-ex].

[183] M. Bonvini, A. S. Papanastasiou and F. J. Tackmann, *Matched predictions for the $b\bar{b}H$ cross section at the 13 TeV LHC*, JHEP **10** (2016) 053, arXiv: 1605.01733 [hep-ph].

[184] R. V. Harlander, *Higgs production in heavy-quark annihilation through next-to-next-to-leading order QCD*, Eur. Phys. J. C **76** (2016) 252, arXiv: 1512.04901 [hep-ph].

[185] A. Djouadi, J. Kalinowski and M. Spira, *HDECAY: a program for Higgs boson decays in the Standard Model and its supersymmetric extension*, Comput. Phys. Commun. **108** (1998) 56, arXiv: hep-ph/9704448.

[186] A. Djouadi, J. Kalinowski, M. Mühlleitner and M. Spira, *HDECAY: Twenty++ years after*, Comput. Phys. Commun. **238** (2019) 214, arXiv: 1801.09506 [hep-ph].

[187] G. Cowan, K. Cranmer, E. Gross and O. Vitells, *Asymptotic formulae for likelihood-based tests of new physics*, Eur. Phys. J. C **71** (2011) 1554, arXiv: 1007.1727 [physics.data-an], Erratum: Eur. Phys. J. C **73** (2013) 2501.

[188] R. Contino, M. Ghezzi, C. Grojean, M. Mühlleitner and M. Spira, *Effective Lagrangian for a light Higgs-like scalar*, JHEP **07** (2013) 035, arXiv: 1303.3876 [hep-ph].

[189] B. Grzadkowski, M. Iskrzynski, M. Misiak and J. Rosiek, *Dimension-six terms in the Standard Model Lagrangian*, JHEP **10** (2010) 085, arXiv: 1008.4884 [hep-ph].

[190] I. Brivio and M. Trott, *The standard model as an effective field theory*, Phys. Rept. **793** (2019) 1, arXiv: 1706.08945 [hep-ph].

[191] A. Alloul, B. Fuks and V. Sanz, *Phenomenology of the Higgs effective Lagrangian via FeynRules*, JHEP **04** (2014) 110, arXiv: 1310.5150 [hep-ph].

[192] I. Brivio, Y. Jiang and M. Trott, *The SMEFTsim package, theory and tools*, JHEP **12** (2017) 070, arXiv: 1709.06492 [hep-ph].

[193] M. L. Mangano, M. Moretti, F. Piccinini and M. Treccani, *Matching matrix elements and shower evolution for top-pair production in hadronic collisions*, JHEP **01** (2007) 013, arXiv: hep-ph/0611129.

[194] A. Buckley et al., *Rivet user manual*, Comput. Phys. Commun. **184** (2013) 2803, arXiv: 1003.0694 [hep-ph].

[195] A. Buckley, H. Hoeth, H. Lacker, H. Schulz and J. E. von Seggern, *Systematic event generator tuning for the LHC*, Eur. Phys. J. C **65** (2010) 331, arXiv: 0907.2973 [hep-ph].

[196] I. Brivio, T. Corbett and M. Trott, *The Higgs width in the SMEFT*, JHEP **10** (2019) 056, arXiv: 1906.06949 [hep-ph].

[197] A. Azatov, R. Contino, C. S. Machado and F. Riva, *Helicity selection rules and noninterference for BSM amplitudes*, Phys. Rev. D **95** (2017) 065014, arXiv: 1607.05236 [hep-ph].

[198] ATLAS Collaboration, *ATLAS Computing Acknowledgements*, ATL-SOFT-PUB-2021-003, URL: https://cds.cern.ch/record/2776662.

[199] R. D. Ball et al., *Parton distributions from high-precision collider data*, Eur. Phys. J. C **77** (2017) 663, arXiv: 1706.00428 [hep-ph].

[200] A. Banfi, P. F. Monni, G. P. Salam and G. Zanderighi, *Higgs and Z-boson Production with a Jet Veto*, Phys. Rev. Lett. **109** (2012) 202001, arXiv: 1206.4998 [hep-ph].

[201] A. Banfi et al., *Jet-vetoed Higgs cross section in gluon fusion at N^3LO+NNLL with small-R resummation*, JHEP **04** (2016) 049, arXiv: 1511.02886 [hep-ph].

[202] B. Mistlberger, *Higgs boson production at hadron colliders at N^3LO in QCD*, JHEP **05** (2018) 028, arXiv: 1802.00833 [hep-ph].

[203] X. Chen et al., *Precise QCD description of the Higgs boson transverse momentum spectrum*, Phys. Lett. B **788** (2019) 425, arXiv: 1805.00736 [hep-ph].

[204] G. Lustermans, J. K. L. Michel, F. J. Tackmann and W. J. Waalewijn, *Joint two-dimensional resummation in q_T and 0-jettiness at NNLL*, JHEP **03** (2019) 124, arXiv: 1901.03331 [hep-ph].

The ATLAS Collaboration

G. Aad[99], B. Abbott[125], D.C. Abbott[100], A. Abed Abud[35], K. Abeling[52], D.K. Abhayasinghe[92], S.H. Abidi[28], A. Aboulhorma[34e], H. Abramowicz[158], H. Abreu[157], Y. Abulaiti[122], A.C. Abusleme Hoffman[143a], B.S. Acharya[65a,65b,o], B. Achkar[52], L. Adam[97], C. Adam Bourdarios[4], L. Adamczyk[82a], L. Adamek[163], S.V. Addepalli[25], J. Adelman[117], A. Adiguzel[11c,aa], S. Adorni[53], T. Adye[140], A.A. Affolder[142], Y. Afik[35], C. Agapopoulou[63], M.N. Agaras[13], J. Agarwala[69a,69b], A. Aggarwal[115], C. Agheorghiesei[26c], J.A. Aguilar-Saavedra[136f,136a,z], A. Ahmad[35], F. Ahmadov[78], W.S. Ahmed[101], X. Ai[45], G. Aielli[72a,72b], I. Aizenberg[176], S. Akatsuka[84], M. Akbiyik[97], T.P.A. Åkesson[95], A.V. Akimov[108], K. Al Khoury[38], G.L. Alberghi[22b], J. Albert[172], P. Albicocco[50], M.J. Alconada Verzini[87], S. Alderweireldt[49], M. Aleksa[35], I.N. Aleksandrov[78], C. Alexa[26b], T. Alexopoulos[9], A. Alfonsi[116], F. Alfonsi[22b], M. Alhroob[125], B. Ali[138], S. Ali[155], M. Aliev[162], G. Alimonti[67a], C. Allaire[35], B.M.M. Allbrooke[153], P.P. Allport[20], A. Aloisio[68a,68b], F. Alonso[87], C. Alpigiani[145], E. Alunno Camelia[72a,72b], M. Alvarez Estevez[96], M.G. Alviggi[68a,68b], Y. Amaral Coutinho[79b], A. Ambler[101], L. Ambroz[131], C. Amelung[35], D. Amidei[103], S.P. Amor Dos Santos[136a], S. Amoroso[45], K.R. Amos[170], C.S. Amrouche[53], V. Ananiev[130], C. Anastopoulos[146], N. Andari[141], T. Andeen[10], J.K. Anders[19], S.Y. Andrean[44a,44b], A. Andreazza[67a,67b], S. Angelidakis[8], A. Angerami[38], A.V. Anisenkov[118b,118a], A. Annovi[70a], C. Antel[53], M.T. Anthony[146], E. Antipov[126], M. Antonelli[50], D.J.A. Antrim[17], F. Anulli[71a], M. Aoki[80], J.A. Aparisi Pozo[170], M.A. Aparo[153], L. Aperio Bella[45], N. Aranzabal[35], V. Araujo Ferraz[79a], C. Arcangeletti[50], A.T.H. Arce[48], E. Arena[89], J-F. Arguin[107], S. Argyropoulos[51], J.-H. Arling[45], A.J. Armbruster[35], A. Armstrong[167], O. Arnaez[163], H. Arnold[35], Z.P. Arrubarrena Tame[111], G. Artoni[71a,71b], H. Asada[113], K. Asai[123], S. Asai[160], N.A. Asbah[58], E.M. Asimakopoulou[168], L. Asquith[153], J. Assahsah[34d], K. Assamagan[28], R. Astalos[27a], R.J. Atkin[32a], M. Atkinson[169], N.B. Atlay[18], H. Atmani[59b], P.A. Atmasiddha[103], K. Augsten[138], S. Auricchio[68a,68b], V.A. Austrup[178], G. Avner[157], G. Avolio[35], M.K. Ayoub[14c], G. Azuelos[107,ai], D. Babal[27a], H. Bachacou[141], K. Bachas[159], A. Bachiu[33], F. Backman[44a,44b], A. Badea[58], P. Bagnaia[71a,71b], M. Bahmani[18], H. Bahrasemani[149], A.J. Bailey[170], V.R. Bailey[169], J.T. Baines[140], C. Bakalis[9], O.K. Baker[179], P.J. Bakker[116], E. Bakos[15], D. Bakshi Gupta[7], S. Balaji[154], R. Balasubramanian[116], E.M. Baldin[118b,118a], P. Balek[139], E. Ballabene[67a,67b], F. Balli[141], L.M. Baltes[60a], W.K. Balunas[131], J. Balz[97], E. Banas[83], M. Bandieramonte[135], A. Bandyopadhyay[23], S. Bansal[23], L. Barak[158], E.L. Barberio[102], D. Barberis[54b,54a], M. Barbero[99], G. Barbour[93], K.N. Barends[32a], T. Barillari[112], M-S. Barisits[35], J. Barkeloo[128], T. Barklow[150], R.M. Barnett[17], A. Baroncelli[59a], G. Barone[28], A.J. Barr[131], L. Barranco Navarro[44a,44b], F. Barreiro[96], J. Barreiro Guimarães da Costa[14a], U. Barron[158], S. Barsov[134], F. Bartels[60a], R. Bartoldus[150], G. Bartolini[99], A.E. Barton[88], P. Bartos[27a], A. Basalaev[45], A. Basan[97], M. Baselga[45], I. Bashta[73a,73b], A. Bassalat[63,af], M.J. Basso[163], C.R. Basson[98], R.L. Bates[56], S. Batlamous[34e], J.R. Batley[31], B. Batool[148], M. Battaglia[142], M. Bauce[71a,71b], F. Bauer[141,*], P. Bauer[23], H.S. Bawa[30], A. Bayirli[11c], J.B. Beacham[48], T. Beau[132], P.H. Beauchemin[166], F. Becherer[51], P. Bechtle[23], H.P. Beck[19,q], K. Becker[174], C. Becot[45], A.J. Beddall[11c], V.A. Bednyakov[78], C.P. Bee[152], T.A. Beermann[35], M. Begalli[79b], M. Begel[28], A. Behera[152], J.K. Behr[45], C. Beirao Da Cruz E Silva[35], J.F. Beirer[52,35], F. Beisiegel[23], M. Belfkir[4], G. Bella[158], L. Bellagamba[22b], A. Bellerive[33], P. Bellos[20], K. Beloborodov[118b,118a], K. Belotskiy[109], N.L. Belyaev[109], D. Benchekroun[34a], Y. Benhammou[158], D.P. Benjamin[28], M. Benoit[28], J.R. Bensinger[25], S. Bentvelsen[116], L. Beresford[35], M. Beretta[50], D. Berge[18], E. Bergeaas Kuutmann[168], N. Berger[4], B. Bergmann[138], L.J. Bergsten[25], J. Beringer[17], S. Berlendis[6], G. Bernardi[132], C. Bernius[150], F.U. Bernlochner[23], T. Berry[92], P. Berta[139], I.A. Bertram[88], O. Bessidskaia Bylund[178], S. Bethke[112], A. Betti[41], A.J. Bevan[91], S. Bhatta[152], D.S. Bhattacharya[173], P. Bhattarai[25], V.S. Bhopatkar[5], R. Bi[135], R. Bi[28], R.M. Bianchi[135], O. Biebel[111], R. Bielski[128], N.V. Biesuz[70a,70b], M. Biglietti[73a], T.R.V. Billoud[138],

M. Bindi[52], A. Bingul[11d], C. Bini[71a,71b], S. Biondi[22b,22a], A. Biondini[89], C.J. Birch-sykes[98], G.A. Bird[20,140], M. Birman[176], T. Bisanz[35], J.P. Biswal[2], D. Biswas[177,j], A. Bitadze[98], K. Bjørke[130], I. Bloch[45], C. Blocker[25], A. Blue[56], U. Blumenschein[91], J. Blumenthal[97], G.J. Bobbink[116], V.S. Bobrovnikov[118b,118a], M. Boehler[51], D. Bogavac[13], A.G. Bogdanchikov[118b,118a], C. Bohm[44a], V. Boisvert[92], P. Bokan[45], T. Bold[82a], M. Bomben[132], M. Bona[91], M. Boonekamp[141], C.D. Booth[92], A.G. Borbély[56], H.M. Borecka-Bielska[107], L.S. Borgna[93], G. Borissov[88], D. Bortoletto[131], D. Boscherini[22b], M. Bosman[13], J.D. Bossio Sola[35], K. Bouaouda[34a], J. Boudreau[135], E.V. Bouhova-Thacker[88], D. Boumediene[37], R. Bouquet[132], A. Boveia[124], J. Boyd[35], D. Boye[28], I.R. Boyko[78], A.J. Bozson[92], J. Bracinik[20], N. Brahimi[59d,59c], G. Brandt[178], O. Brandt[31], F. Braren[45], B. Brau[100], J.E. Brau[128], W.D. Breaden Madden[56], K. Brendlinger[45], R. Brener[176], L. Brenner[35], R. Brenner[168], S. Bressler[176], B. Brickwedde[97], D. Britton[56], D. Britzger[112], I. Brock[23], R. Brock[104], G. Brooijmans[38], W.K. Brooks[143e], E. Brost[28], P.A. Bruckman de Renstrom[83], B. Brüers[45], D. Bruncko[27b], A. Bruni[22b], G. Bruni[22b], M. Bruschi[22b], N. Bruscino[71a,71b], L. Bryngemark[150], T. Buanes[16], Q. Buat[145], P. Buchholz[148], A.G. Buckley[56], I.A. Budagov[78], M.K. Bugge[130], O. Bulekov[109], B.A. Bullard[58], S. Burdin[89], C.D. Burgard[45], A.M. Burger[126], B. Burghgrave[7], J.T.P. Burr[31], C.D. Burton[10], J.C. Burzynski[149], E.L. Busch[38], V. Büscher[97], P.J. Bussey[56], J.M. Butler[24], C.M. Buttar[56], J.M. Butterworth[93], W. Buttinger[140], C.J. Buxo Vazquez[104], A.R. Buzykaev[118b,118a], G. Cabras[22b], S. Cabrera Urbán[170], D. Caforio[55], H. Cai[135], V.M.M. Cairo[150], O. Cakir[3a], N. Calace[35], P. Calafiura[17], G. Calderini[132], P. Calfayan[64], G. Callea[56], L.P. Caloba[79b], D. Calvet[37], S. Calvet[37], T.P. Calvet[99], M. Calvetti[70a,70b], R. Camacho Toro[132], S. Camarda[35], D. Camarero Munoz[96], P. Camarri[72a,72b], M.T. Camerlingo[73a,73b], D. Cameron[130], C. Camincher[172], M. Campanelli[93], A. Camplani[39], V. Canale[68a,68b], A. Canesse[101], M. Cano Bret[76], J. Cantero[96], Y. Cao[169], F. Capocasa[25], M. Capua[40b,40a], A. Carbone[67a,67b], R. Cardarelli[72a], J.C.J. Cardenas[7], F. Cardillo[170], G. Carducci[40b,40a], T. Carli[35], G. Carlino[68a], B.T. Carlson[135], E.M. Carlson[172,164a], L. Carminati[67a,67b], M. Carnesale[71a,71b], R.M.D. Carney[150], S. Caron[115], E. Carquin[143e], S. Carrá[45], G. Carratta[22b,22a], J.W.S. Carter[163], T.M. Carter[49], D. Casadei[32c], M.P. Casado[13,g], A.F. Casha[163], E.G. Castiglia[179], F.L. Castillo[60a], L. Castillo Garcia[13], V. Castillo Gimenez[170], N.F. Castro[136a,136e], A. Catinaccio[35], J.R. Catmore[130], A. Cattai[35], V. Cavaliere[28], N. Cavalli[22b,22a], V. Cavasinni[70a,70b], E. Celebi[11c], F. Celli[131], M.S. Centonze[66a,66b], K. Cerny[127], A.S. Cerqueira[79a], A. Cerri[153], L. Cerrito[72a,72b], F. Cerutti[17], A. Cervelli[22b], S.A. Cetin[11c,ab], Z. Chadi[34a], D. Chakraborty[117], M. Chala[136f], J. Chan[177], W.S. Chan[116], W.Y. Chan[89], J.D. Chapman[31], B. Chargeishvili[156b], D.G. Charlton[20], T.P. Charman[91], M. Chatterjee[19], S. Chekanov[5], S.V. Chekulaev[164a], G.A. Chelkov[78,ad], A. Chen[103], B. Chen[158], B. Chen[172], C. Chen[59a], C.H. Chen[77], H. Chen[14c], H. Chen[28], J. Chen[59c], J. Chen[25], S. Chen[133], S.J. Chen[14c], X. Chen[59c], X. Chen[14b], Y. Chen[59a], Y-H. Chen[45], C.L. Cheng[177], H.C. Cheng[61a], A. Cheplakov[78], E. Cheremushkina[45], E. Cherepanova[78], R. Cherkaoui El Moursli[34e], E. Cheu[6], K. Cheung[62], L. Chevalier[141], V. Chiarella[50], G. Chiarelli[70a], G. Chiodini[66a], A.S. Chisholm[20], A. Chitan[26b], Y.H. Chiu[172], M.V. Chizhov[78], K. Choi[10], A.R. Chomont[71a,71b], Y. Chou[100], Y.S. Chow[116], T. Chowdhury[32f], L.D. Christopher[32f], M.C. Chu[61a], X. Chu[14a,14d], J. Chudoba[137], J.J. Chwastowski[83], D. Cieri[112], K.M. Ciesla[83], V. Cindro[90], I.A. Cioară[26b], A. Ciocio[17], F. Cirotto[68a,68b], Z.H. Citron[176,k], M. Citterio[67a], D.A. Ciubotaru[26b], B.M. Ciungu[163], A. Clark[53], P.J. Clark[49], J.M. Clavijo Columbie[45], S.E. Clawson[98], C. Clement[44a,44b], L. Clissa[22b,22a], Y. Coadou[99], M. Cobal[65a,65c], A. Coccaro[54b], J. Cochran[77], R.F. Coelho Barrue[136a], R. Coelho Lopes De Sa[100], S. Coelli[67a], H. Cohen[158], A.E.C. Coimbra[35], B. Cole[38], J. Collot[57], P. Conde Muiño[136a,136g], S.H. Connell[32c], I.A. Connelly[56], E.I. Conroy[131], F. Conventi[68a,aj], H.G. Cooke[20], A.M. Cooper-Sarkar[131], F. Cormier[171], L.D. Corpe[35], M. Corradi[71a,71b], E.E. Corrigan[95], F. Corriveau[101,x], M.J. Costa[170], F. Costanza[4], D. Costanzo[146], B.M. Cote[124], G. Cowan[92], J.W. Cowley[31], K. Cranmer[122], S. Crépé-Renaudin[57], F. Crescioli[132], M. Cristinziani[148], M. Cristoforetti[74a,74b,b], V. Croft[166], G. Crosetti[40b,40a], A. Cueto[35],

T. Cuhadar Donszelmann[167], H. Cui[14a,14d], Z. Cui[6], A.R. Cukierman[150], W.R. Cunningham[56], F. Curcio[40b,40a], P. Czodrowski[35], M.M. Czurylo[60b], M.J. Da Cunha Sargedas De Sousa[59a], J.V. Da Fonseca Pinto[79b], C. Da Via[98], W. Dabrowski[82a], T. Dado[46], S. Dahbi[32f], T. Dai[103], C. Dallapiccola[100], M. Dam[39], G. D'amen[28], V. D'Amico[73a,73b], J. Damp[97], J.R. Dandoy[133], M.F. Daneri[29], M. Danninger[149], V. Dao[35], G. Darbo[54b], S. Darmora[5], A. Dattagupta[128], S. D'Auria[67a,67b], C. David[164b], T. Davidek[139], D.R. Davis[48], B. Davis-Purcell[33], I. Dawson[91], K. De[7], R. De Asmundis[68a], M. De Beurs[116], S. De Castro[22b,22a], N. De Groot[115], P. de Jong[116], H. De la Torre[104], A. De Maria[14c], D. De Pedis[71a], A. De Salvo[71a], U. De Sanctis[72a,72b], M. De Santis[72a,72b], A. De Santo[153], J.B. De Vivie De Regie[57], D.V. Dedovich[78], J. Degens[116], A.M. Deiana[41], J. Del Peso[96], F. Del Rio[60a], F. Deliot[141], C.M. Delitzsch[6], M. Della Pietra[68a,68b], D. Della Volpe[53], A. Dell'Acqua[35], L. Dell'Asta[67a,67b], M. Delmastro[4], P.A. Delsart[57], S. Demers[179], M. Demichev[78], S.P. Denisov[119], L. D'Eramo[117], D. Derendarz[83], J.E. Derkaoui[34d], F. Derue[132], P. Dervan[89], K. Desch[23], K. Dette[163], C. Deutsch[23], P.O. Deviveiros[35], F.A. Di Bello[71a,71b], A. Di Ciaccio[72a,72b], L. Di Ciaccio[4], A. Di Domenico[71a,71b], C. Di Donato[68a,68b], A. Di Girolamo[35], G. Di Gregorio[70a,70b], A. Di Luca[74a,74b,b], B. Di Micco[73a,73b], R. Di Nardo[73a,73b], C. Diaconu[99], F.A. Dias[116], T. Dias Do Vale[136a], M.A. Diaz[143a], F.G. Diaz Capriles[23], M. Didenko[170], E.B. Diehl[103], S. Díez Cornell[45], C. Diez Pardos[148], C. Dimitriadi[23,168], A. Dimitrievska[17], W. Ding[14b], J. Dingfelder[23], I-M. Dinu[26b], S.J. Dittmeier[60b], F. Dittus[35], F. Djama[99], T. Djobava[156b], J.I. Djuvsland[16], M.A.B. Do Vale[144], D. Dodsworth[25], C. Doglioni[95], J. Dolejsi[139], Z. Dolezal[139], M. Donadelli[79c], B. Dong[59c], J. Donini[37], A. D'onofrio[14c], M. D'Onofrio[89], J. Dopke[140], A. Doria[68a], M.T. Dova[87], A.T. Doyle[56], E. Drechsler[149], E. Dreyer[176], A.S. Drobac[166], D. Du[59a], T.A. du Pree[116], F. Dubinin[108], M. Dubovsky[27a], E. Duchovni[176], G. Duckeck[111], O.A. Ducu[35,26b], D. Duda[112], A. Dudarev[35], M. D'uffizi[98], L. Duflot[63], M. Dührssen[35], C. Dülsen[178], A.E. Dumitriu[26b], M. Dunford[60a], S. Dungs[46], K. Dunne[44a,44b], A. Duperrin[99], H. Duran Yildiz[3a], M. Düren[55], A. Durglishvili[156b], B. Dutta[45], B.L. Dwyer[117], G.I. Dyckes[17], M. Dyndal[82a], S. Dysch[98], B.S. Dziedzic[83], B. Eckerova[27a], M.G. Eggleston[48], E. Egidio Purcino De Souza[79b], L.F. Ehrke[53], G. Eigen[16], K. Einsweiler[17], T. Ekelof[168], Y. El Ghazali[34b], H. El Jarrari[34e], A. El Moussaouy[34a], V. Ellajosyula[168], M. Ellert[168], F. Ellinghaus[178], A.A. Elliot[91], N. Ellis[35], J. Elmsheuser[28], M. Elsing[35], D. Emeliyanov[140], A. Emerman[38], Y. Enari[160], J. Erdmann[46], A. Ereditato[19], P.A. Erland[83], M. Errenst[178], M. Escalier[63], C. Escobar[170], O. Estrada Pastor[170], E. Etzion[158], G. Evans[136a], H. Evans[64], M.O. Evans[153], A. Ezhilov[134], S. Ezzarqtouni[34a], F. Fabbri[56], L. Fabbri[22b,22a], G. Facini[174], V. Fadeyev[142], R.M. Fakhrutdinov[119], S. Falciano[71a], P.J. Falke[23], S. Falke[35], J. Faltova[139], Y. Fan[14a], Y. Fang[14a], G. Fanourakis[43], M. Fanti[67a,67b], M. Faraj[59c], A. Farbin[7], A. Farilla[73a], E.M. Farina[69a,69b], T. Farooque[104], S.M. Farrington[49], P. Farthouat[35], F. Fassi[34e], D. Fassouliotis[8], M. Faucci Giannelli[72a,72b], W.J. Fawcett[31], L. Fayard[63], O.L. Fedin[134,p], G. Fedotov[134], M. Feickert[169], L. Feligioni[99], A. Fell[146], C. Feng[59b], M. Feng[14b], M.J. Fenton[167], A.B. Fenyuk[119], S.W. Ferguson[42], J.A. Fernandez Pretel[51], J. Ferrando[45], A. Ferrari[168], P. Ferrari[116], R. Ferrari[69a], D. Ferrere[53], C. Ferretti[103], F. Fiedler[97], A. Filipčič[90], F. Filthaut[115], M.C.N. Fiolhais[136a,136c,a], L. Fiorini[170], F. Fischer[148], W.C. Fisher[104], T. Fitschen[20], I. Fleck[148], P. Fleischmann[103], T. Flick[178], L. Flores[133], M. Flores[32d], L.R. Flores Castillo[61a], F.M. Follega[74a,74b], N. Fomin[16], J.H. Foo[163], B.C. Forland[64], A. Formica[141], F.A. Förster[13], A.C. Forti[98], E. Fortin[99], M.G. Foti[131], L. Fountas[8], D. Fournier[63], H. Fox[88], P. Francavilla[70a,70b], S. Francescato[58], M. Franchini[22b,22a], S. Franchino[60a], D. Francis[35], L. Franco[4], L. Franconi[19], M. Franklin[58], G. Frattari[71a,71b], A.C. Freegard[91], P.M. Freeman[20], W.S. Freund[79b], E.M. Freundlich[46], D. Froidevaux[35], J.A. Frost[131], Y. Fu[59a], M. Fujimoto[123], E. Fullana Torregrosa[170], J. Fuster[170], A. Gabrielli[22b,22a], A. Gabrielli[35], P. Gadow[45], G. Gagliardi[54b,54a], L.G. Gagnon[17], G.E. Gallardo[131], E.J. Gallas[131], B.J. Gallop[140], R. Gamboa Goni[91], K.K. Gan[124], S. Ganguly[160], J. Gao[59a], Y. Gao[49], Y.S. Gao[30,m], F.M. Garay Walls[143a], C. García[170], J.E. García Navarro[170], J.A. García Pascual[14a], M. Garcia-Sciveres[17], R.W. Gardner[36], D. Garg[76], R.B. Garg[150], S. Gargiulo[51], C.A. Garner[163], V. Garonne[28], S.J. Gasiorowski[145], P. Gaspar[79b], G. Gaudio[69a], P. Gauzzi[71a,71b], I.L. Gavrilenko[108], A. Gavrilyuk[120], C. Gay[171], G. Gaycken[45], E.N. Gazis[9], A.A. Geanta[26b], C.M. Gee[142], J. Geisen[95], M. Geisen[97], C. Gemme[54b], M.H. Genest[57], S. Gentile[71a,71b], S. George[92], W.F. George[20], T. Geralis[43], L.O. Gerlach[52], P. Gessinger-Befurt[35], M. Ghasemi Bostanabad[172], A. Ghosh[167], A. Ghosh[6], B. Giacobbe[22b], S. Giagu[71a,71b], N. Giangiacomi[163], P. Giannetti[70a], A. Giannini[68a,68b], S.M. Gibson[92], M. Gignac[142], D.T. Gil[82b], B.J. Gilbert[38], D. Gillberg[33], G. Gilles[116], N.E.K. Gillwald[45], D.M. Gingrich[2,ai], M.P. Giordani[65a,65c], P.F. Giraud[141], G. Giugliarelli[65a,65c], D. Giugni[67a], F. Giuli[72a,72b], I. Gkialas[8,h], P. Gkountoumis[9], L.K. Gladilin[110], C. Glasman[96], G.R. Gledhill[128], M. Glisic[128], I. Gnesi[40b,d], Y. Go[28], M. Goblirsch-Kolb[25], D. Godin[107], S. Goldfarb[102], T. Golling[53], D. Golubkov[119], J.P. Gombas[104], A. Gomes[136a,136b], R. Goncalves Gama[52], R. Gonçalo[136a,136c], G. Gonella[128], L. Gonella[20], A. Gongadze[78], F. Gonnella[20], J.L. Gonski[38], S. González de la Hoz[170], S. Gonzalez Fernandez[13], R. Gonzalez Lopez[89], C. Gonzalez Renteria[17], R. Gonzalez Suarez[168], S. Gonzalez-Sevilla[53], G.R. Gonzalvo Rodriguez[170], R.Y. González Andana[49], L. Goossens[35], N.A. Gorasia[20], P.A. Gorbounov[120], H.A. Gordon[28], B. Gorini[35], E. Gorini[66a,66b], A. Gorišek[90], A.T. Goshaw[48], M.I. Gostkin[78], C.A. Gottardo[115], M. Gouighri[34b], V. Goumarre[45], A.G. Goussiou[145], N. Govender[32c], C. Goy[4], I. Grabowska-Bold[82a], K. Graham[33], E. Gramstad[130], S. Grancagnolo[18], M. Grandi[153], V. Gratchev[134], P.M. Gravila[26f], F.G. Gravili[66a,66b], H.M. Gray[17], C. Grefe[23], I.M. Gregor[45], P. Grenier[150], K. Grevtsov[45], C. Grieco[13], N.A. Grieser[125], A.A. Grillo[142], K. Grimm[30,l], S. Grinstein[13,u], J.-F. Grivaz[63], S. Groh[97], E. Gross[176], J. Grosse-Knetter[52], C. Grud[103], A. Grummer[114], J.C. Grundy[131], L. Guan[103], W. Guan[177], C. Gubbels[171], J.G.R. Guerrero Rojas[170], F. Guescini[112], D. Guest[18], R. Gugel[97], A. Guida[45], T. Guillemin[4], S. Guindon[35], F. Guo[14a], J. Guo[59c], L. Guo[63], Y. Guo[103], R. Gupta[45], S. Gurbuz[23], G. Gustavino[35], M. Guth[53], P. Gutierrez[125], L.F. Gutierrez Zagazeta[133], C. Gutschow[93], C. Guyot[141], C. Gwenlan[131], C.B. Gwilliam[89], E.S. Haaland[130], A. Haas[122], M. Habedank[45], C. Haber[17], H.K. Hadavand[7], A. Hadef[97], S. Hadzic[112], M. Haleem[173], J. Haley[126], J.J. Hall[146], G. Halladjian[104], G.D. Hallewell[99], L. Halser[19], K. Hamano[172], H. Hamdaoui[34e], M. Hamer[23], G.N. Hamity[49], K. Han[59a], L. Han[14c], L. Han[59a], S. Han[17], Y.F. Han[163], K. Hanagaki[80,s], M. Hance[142], D.A. Hangal[38], M.D. Hank[36], R. Hankache[98], E. Hansen[95], J.B. Hansen[39], J.D. Hansen[39], P.H. Hansen[39], K. Hara[165], T. Harenberg[178], S. Harkusha[105], Y.T. Harris[131], P.F. Harrison[174], N.M. Hartman[150], N.M. Hartmann[111], Y. Hasegawa[147], A. Hasib[49], S. Haug[19], R. Hauser[104], M. Havranek[138], C.M. Hawkes[20], R.J. Hawkings[35], S. Hayashida[113], D. Hayden[104], C. Hayes[103], R.L. Hayes[171], C.P. Hays[131], J.M. Hays[91], H.S. Hayward[89], F. He[59a], Y. He[161], Y. He[132], M.P. Heath[49], V. Hedberg[95], A.L. Heggelund[130], N.D. Hehir[91], C. Heidegger[51], K.K. Heidegger[51], W.D. Heidorn[77], J. Heilman[33], S. Heim[45], T. Heim[17], B. Heinemann[45,ag], J.G. Heinlein[133], J.J. Heinrich[128], L. Heinrich[35], J. Hejbal[137], L. Helary[45], A. Held[122], C.M. Helling[142], S. Hellman[44a,44b], C. Helsens[35], R.C.W. Henderson[88], L. Henkelmann[31], A.M. Henriques Correia[35], H. Herde[150], Y. Hernández Jiménez[152], H. Herr[97], M.G. Herrmann[111], T. Herrmann[47], G. Herten[51], R. Hertenberger[111], L. Hervas[35], N.P. Hessey[164a], H. Hibi[81], S. Higashino[80], E. Higón-Rodriguez[170], S.J. Hillier[20], I. Hinchliffe[17], F. Hinterkeuser[23], M. Hirose[129], S. Hirose[165], D. Hirschbuehl[178], B. Hiti[90], O. Hladik[137], J. Hobbs[152], R. Hobincu[26e], N. Hod[176], M.C. Hodgkinson[146], B.H. Hodkinson[31], A. Hoecker[35], J. Hofer[45], D. Hohn[51], T. Holm[23], M. Holzbock[112], L.B.A.H. Hommels[31], B.P. Honan[98], J. Hong[59c], T.M. Hong[135], Y. Hong[52], J.C. Honig[51], A. Hönle[112], B.H. Hooberman[169], W.H. Hopkins[5], Y. Horii[113], L.A. Horyn[36], S. Hou[155], J. Howarth[56], J. Hoya[87], M. Hrabovsky[127], A. Hrynevich[106], T. Hryn'ova[4], P.J. Hsu[62], S.-C. Hsu[145], Q. Hu[38], S. Hu[59c], Y.F. Hu[14a,14d,ak], D.P. Huang[93], X. Huang[14c], Y. Huang[59a], Y. Huang[14a], Z. Hubacek[138], F. Hubaut[99], M. Huebner[23], F. Huegging[23], T.B. Huffman[131], M. Huhtinen[35], S.K. Huiberts[16], R. Hulsken[57], N. Huseynov[12,ac], J. Huston[104], J. Huth[58], R. Hyneman[150], S. Hyrych[27a], G. Iacobucci[53], G. Iakovidis[28], I. Ibragimov[148], L. Iconomidou-Fayard[63], P. Iengo[35], R. Iguchi[160], T. Iizawa[53], Y. Ikegami[80], A. Ilg[19], N. Ilic[163], H. Imam[34a], T. Ingebretsen Carlson[44a,44b], G. Introzzi[69a,69b], M. Iodice[73a], V. Ippolito[71a,71b], M. Ishino[160], W. Islam[177], C. Issever[18,45], S. Istin[11c,al],

H. Ito[175], J.M. Iturbe Ponce[61a], R. Iuppa[74a,74b], A. Ivina[176], J.M. Izen[42], V. Izzo[68a], P. Jacka[137], P. Jackson[1], R.M. Jacobs[45], B.P. Jaeger[149], C.S. Jagfeld[111], G. Jäkel[178], K. Jakobs[51], T. Jakoubek[176], J. Jamieson[56], K.W. Janas[82a], G. Jarlskog[95], A.E. Jaspan[89], T. Javůrek[35], M. Javurkova[100], F. Jeanneau[141], L. Jeanty[128], J. Jejelava[156a,y], P. Jenni[51,e], S. Jézéquel[4], J. Jia[152], Z. Jia[14c], Y. Jiang[59a], S. Jiggins[49], J. Jimenez Pena[112], S. Jin[14c], A. Jinaru[26b], O. Jinnouchi[161], H. Jivan[32f], P. Johansson[146], K.A. Johns[6], C.A. Johnson[64], D.M. Jones[31], E. Jones[174], R.W.L. Jones[88], T.J. Jones[89], J. Jovicevic[15], X. Ju[17], J.J. Junggeburth[35], A. Juste Rozas[13,u], S. Kabana[143d], A. Kaczmarska[83], M. Kado[71a,71b], H. Kagan[124], M. Kagan[150], A. Kahn[38], A. Kahn[133], C. Kahra[97], T. Kaji[175], E. Kajomovitz[157], C.W. Kalderon[28], A. Kamenshchikov[119], N.J. Kang[142], Y. Kano[113], D. Kar[32f], K. Karava[131], M.J. Kareem[164b], E. Karentzos[51], I. Karkanias[159], S.N. Karpov[78], Z.M. Karpova[78], V. Kartvelishvili[88], A.N. Karyukhin[119], E. Kasimi[159], C. Kato[59d], J. Katzy[45], S. Kaur[33], K. Kawade[147], K. Kawagoe[86], T. Kawaguchi[113], T. Kawamoto[141], G. Kawamura[52], E.F. Kay[172], F.I. Kaya[166], S. Kazakos[13], V.F. Kazanin[118b,118a], Y. Ke[152], J.M. Keaveney[32a], R. Keeler[172], J.S. Keller[33], A.S. Kelly[93], D. Kelsey[153], J.J. Kempster[20], J. Kendrick[20], K.E. Kennedy[38], O. Kepka[137], S. Kersten[178], B.P. Kerševan[90], S. Ketabchi Haghighat[163], M. Khandoga[132], A. Khanov[126], A.G. Kharlamov[118b,118a], T. Kharlamova[118b,118a], E.E. Khoda[145], T.J. Khoo[18], G. Khoriauli[173], E. Khramov[78], J. Khubua[156b], M. Kiehn[35], A. Kilgallon[128], E. Kim[161], Y.K. Kim[36], N. Kimura[93], A. Kirchhoff[52], D. Kirchmeier[47], C. Kirfel[23], J. Kirk[140], A.E. Kiryunin[112], T. Kishimoto[160], D.P. Kisliuk[163], C. Kitsaki[9], O. Kivernyk[23], M. Klassen[60a], C. Klein[33], L. Klein[173], M.H. Klein[103], M. Klein[89], U. Klein[89], P. Klimek[35], A. Klimentov[28], F. Klimpel[112], T. Klingl[23], T. Klioutchnikova[35], F.F. Klitzner[111], P. Kluit[116], S. Kluth[112], E. Kneringer[75], T.M. Knight[163], A. Knue[51], D. Kobayashi[86], R. Kobayashi[84], M. Kocian[150], T. Kodama[160], P. Kodys[139], D.M. Koeck[153], P.T. Koenig[23], T. Koffas[33], N.M. Köhler[35], M. Kolb[141], I. Koletsou[4], T. Komarek[127], K. Köneke[51], A.X.Y. Kong[1], T. Kono[123], V. Konstantinides[93], N. Konstantinidis[93], B. Konya[95], R. Kopeliansky[64], S. Koperny[82a], K. Korcyl[83], K. Kordas[159], G. Koren[158], A. Korn[93], S. Korn[52], I. Korolkov[13], N. Korotkova[110], B. Kortman[116], O. Kortner[112], S. Kortner[112], W.H. Kostecka[117], V.V. Kostyukhin[148,162], A. Kotsokechagia[63], A. Kotwal[48], A. Koulouris[35], A. Kourkoumeli-Charalampidi[69a,69b], C. Kourkoumelis[8], E. Kourlitis[5], O. Kovanda[153], R. Kowalewski[172], W. Kozanecki[141], A.S. Kozhin[119], V.A. Kramarenko[110], G. Kramberger[90], P. Kramer[97], D. Krasnopevtsev[59a], M.W. Krasny[132], A. Krasznahorkay[35], J.A. Kremer[97], J. Kretzschmar[89], K. Kreul[18], P. Krieger[163], F. Krieter[111], S. Krishnamurthy[100], A. Krishnan[60b], M. Krivos[139], K. Krizka[17], K. Kroeninger[46], H. Kroha[112], J. Kroll[137], J. Kroll[133], K.S. Krowpman[104], U. Kruchonak[78], H. Krüger[23], N. Krumnack[77], M.C. Kruse[48], J.A. Krzysiak[83], A. Kubota[161], O. Kuchinskaia[162], S. Kuday[3a], D. Kuechler[45], J.T. Kuechler[45], S. Kuehn[35], T. Kuhl[45], V. Kukhtin[78], Y. Kulchitsky[105,ac], S. Kuleshov[143c], M. Kumar[32f], N. Kumari[99], M. Kuna[57], A. Kupco[137], T. Kupfer[46], O. Kuprash[51], H. Kurashige[81], L.L. Kurchaninov[164a], Y.A. Kurochkin[105], A. Kurova[109], E.S. Kuwertz[35], M. Kuze[161], A.K. Kvam[145], J. Kvita[127], T. Kwan[101], K.W. Kwok[61a], C. Lacasta[170], F. Lacava[71a,71b], H. Lacker[18], D. Lacour[132], N.N. Lad[93], E. Ladygin[78], B. Laforge[132], T. Lagouri[143d], S. Lai[52], I.K. Lakomiec[82a], N. Lalloue[57], J.E. Lambert[125], M. Lamberti[67b], S. Lammers[64], W. Lampl[6], C. Lampoudis[159], E. Lançon[28], U. Landgraf[51], M.P.J. Landon[91], V.S. Lang[51], J.C. Lange[52], R.J. Langenberg[100], A.J. Lankford[167], F. Lanni[28], K. Lantzsch[23], A. Lanza[69a], A. Lapertosa[54b,54a], J.F. Laporte[141], T. Lari[67a], F. Lasagni Manghi[22b], M. Lassnig[35], V. Latonova[137], T.S. Lau[61a], A. Laudrain[97], A. Laurier[33], M. Lavorgna[68a,68b], S.D. Lawlor[92], Z. Lawrence[98], M. Lazzaroni[67a,67b], B. Le[98], B. Leban[90], A. Lebedev[77], M. LeBlanc[35], T. LeCompte[5], F. Ledroit-Guillon[57], A.C.A. Lee[93], G.R. Lee[16], L. Lee[58], S.C. Lee[155], S. Lee[77], L.L. Leeuw[32c], B. Lefebvre[164a], H.P. Lefebvre[92], M. Lefebvre[172], C. Leggett[17], K. Lehmann[149], G. Lehmann Miotto[35], W.A. Leight[45], A. Leisos[159,t], M.A.L. Leite[79c], C.E. Leitgeb[45], R. Leitner[139], K.J.C. Leney[41], T. Lenz[23], S. Leone[70a], C. Leonidopoulos[49], A. Leopold[151], C. Leroy[107], R. Les[104], C.G. Lester[31], M. Levchenko[134], J. Levêque[4], D. Levin[103], L.J. Levinson[176], D.J. Lewis[20], B. Li[14b], B. Li[59b], C. Li[59a], C-Q. Li[59c,59d], H. Li[59a], H. Li[59b], H. Li[59b], J. Li[59c], K. Li[145], L. Li[59c],

M. Li[14a,14d], Q.Y. Li[59a], S. Li[59d,59c,c], T. Li[59b], X. Li[45], Z. Li[59b], Z. Li[131], Z. Li[101], Z. Li[89], Z. Liang[14a], M. Liberatore[45], B. Liberti[72a], K. Lie[61c], J. Lieber Marin[79b], K. Lin[104], R.A. Linck[64], R.E. Lindley[6], J.H. Lindon[2], A. Linss[45], E. Lipeles[133], A. Lipniacka[16], T.M. Liss[169,ah], A. Lister[171], J.D. Little[7], B. Liu[14a], B.X. Liu[149], D. Liu[59d,59c], J.B. Liu[59a], J.K.K. Liu[36], K. Liu[59d,59c], M. Liu[59a], M.Y. Liu[59a], P. Liu[14a], Q. Liu[59d,145,59c], X. Liu[59a], Y. Liu[45], Y. Liu[14c,14d], Y.L. Liu[103], Y.W. Liu[59a], M. Livan[69a,69b], J. Llorente Merino[149], S.L. Lloyd[91], E.M. Lobodzinska[45], P. Loch[6], S. Loffredo[72a,72b], T. Lohse[18], K. Lohwasser[146], M. Lokajicek[137], J.D. Long[169], I. Longarini[71a,71b], L. Longo[35], R. Longo[169], I. Lopez Paz[35], A. Lopez Solis[45], J. Lorenz[111], N. Lorenzo Martinez[4], A.M. Lory[111], A. Lösle[51], X. Lou[44a,44b], X. Lou[14a], A. Lounis[63], J. Love[5], P.A. Love[88], J.J. Lozano Bahilo[170], G. Lu[14a], M. Lu[59a], S. Lu[133], Y.J. Lu[62], H.J. Lubatti[145], C. Luci[71a,71b], F.L. Lucio Alves[14c], A. Lucotte[57], F. Luehring[64], I. Luise[152], L. Luminari[71a], O. Lundberg[151], B. Lund-Jensen[151], N.A. Luongo[128], M.S. Lutz[158], D. Lynn[28], H. Lyons[89], R. Lysak[137], E. Lytken[95], F. Lyu[14a], V. Lyubushkin[78], T. Lyubushkina[78], H. Ma[28], L.L. Ma[59b], Y. Ma[93], D.M. Mac Donell[172], G. Maccarrone[50], C.M. Macdonald[146], J.C. MacDonald[146], R. Madar[37], W.F. Mader[47], J. Maeda[81], T. Maeno[28], M. Maerker[47], V. Magerl[51], J. Magro[65a,65c], D.J. Mahon[38], C. Maidantchik[79b], A. Maio[136a,136b,136d], K. Maj[82a], O. Majersky[27a], S. Majewski[128], N. Makovec[63], V. Maksimovic[15], B. Malaescu[132], Pa. Malecki[83], V.P. Maleev[134], F. Malek[57], D. Malito[40b,40a], U. Mallik[76], C. Malone[31], S. Maltezos[9], S. Malyukov[78], J. Mamuzic[170], G. Mancini[50], J.P. Mandalia[91], I. Mandić[90], L. Manhaes de Andrade Filho[79a], I.M. Maniatis[159], M. Manisha[141], J. Manjarres Ramos[47], K.H. Mankinen[95], A. Mann[111], A. Manousos[75], B. Mansoulie[141], I. Manthos[159], S. Manzoni[35], A. Marantis[159,t], G. Marchiori[132], M. Marcisovsky[137], L. Marcoccia[72a,72b], C. Marcon[95], M. Marjanovic[125], Z. Marshall[17], S. Marti-Garcia[170], T.A. Martin[174], V.J. Martin[49], B. Martin dit Latour[16], L. Martinelli[71a,71b], M. Martinez[13,u], P. Martinez Agullo[170], V.I. Martinez Outschoorn[100], S. Martin-Haugh[140], V.S. Martoiu[26b], A.C. Martyniuk[93], A. Marzin[35], S.R. Maschek[112], L. Masetti[97], T. Mashimo[160], J. Masik[98], A.L. Maslennikov[118b,118a], L. Massa[22b], P. Massarotti[68a,68b], P. Mastrandrea[70a,70b], A. Mastroberardino[40b,40a], T. Masubuchi[160], D. Matakias[28], T. Mathisen[168], A. Matic[111], N. Matsuzawa[160], J. Maurer[26b], B. Maček[90], D.A. Maximov[118b,118a], R. Mazini[155], I. Maznas[159], S.M. Mazza[142], C. Mc Ginn[28], J.P. Mc Gowan[101], S.P. Mc Kee[103], T.G. McCarthy[112], W.P. McCormack[17], E.F. McDonald[102], A.E. McDougall[116], J.A. Mcfayden[153], G. Mchedlidze[156b], M.A. McKay[41], R.P. Mckenzie[32f], D.J. Mclaughlin[93], K.D. McLean[172], S.J. McMahon[140], P.C. McNamara[102], R.A. McPherson[172,x], J.E. Mdhluli[32f], Z.A. Meadows[100], S. Meehan[35], T. Megy[37], S. Mehlhase[111], A. Mehta[89], B. Meirose[42], D. Melini[157], B.R. Mellado Garcia[32f], A.H. Melo[52], F. Meloni[45], A. Melzer[23], E.D. Mendes Gouveia[136a], A.M. Mendes Jacques Da Costa[20], H.Y. Meng[163], L. Meng[88], S. Menke[112], M. Mentink[35], E. Meoni[40b,40a], C. Merlassino[131], P. Mermod[53,*], L. Merola[68a,68b], C. Meroni[67a], G. Merz[103], O. Meshkov[108,110], J.K.R. Meshreki[148], J. Metcalfe[5], A.S. Mete[5], C. Meyer[64], J-P. Meyer[141], M. Michetti[18], R.P. Middleton[140], L. Mijović[49], G. Mikenberg[176], M. Mikestikova[137], M. Mikuž[90], H. Mildner[146], A. Milic[163], C.D. Milke[41], D.W. Miller[36], L.S. Miller[33], A. Milov[176], D.A. Milstead[44a,44b], T. Min[14c], A.A. Minaenko[119], I.A. Minashvili[156b], L. Mince[56], A.I. Mincer[122], B. Mindur[82a], M. Mineev[78], Y. Minegishi[160], Y. Mino[84], L.M. Mir[13], M. Miralles Lopez[170], M. Mironova[131], T. Mitani[175], A. Mitra[174], V.A. Mitsou[170], O. Miu[163], P.S. Miyagawa[91], Y. Miyazaki[86], A. Mizukami[80], J.U. Mjörnmark[95], T. Mkrtchyan[60a], M. Mlynarikova[117], T. Moa[44a,44b], S. Mobius[52], K. Mochizuki[107], P. Moder[45], P. Mogg[111], A.F. Mohammed[14a], S. Mohapatra[38], G. Mokgatitswane[32f], B. Mondal[148], S. Mondal[138], K. Mönig[45], E. Monnier[99], L. Monsonis Romero[170], A. Montalbano[149], J. Montejo Berlingen[35], M. Montella[124], F. Monticelli[87], N. Morange[63], A.L. Moreira De Carvalho[136a], M. Moreno Llácer[170], C. Moreno Martinez[13], P. Morettini[54b], S. Morgenstern[174], D. Mori[149], M. Morii[58], M. Morinaga[160], V. Morisbak[130], A.K. Morley[35], A.P. Morris[93], L. Morvaj[35], P. Moschovakos[35], B. Moser[116], M. Mosidze[156b], T. Moskalets[51], P. Moskvitina[115], J. Moss[30,n], E.J.W. Moyse[100], S. Muanza[99], J. Mueller[135], R. Mueller[19], D. Muenstermann[88], G.A. Mullier[95], J.J. Mullin[133], D.P. Mungo[67a,67b], J.L. Munoz Martinez[13], F.J. Munoz Sanchez[98], M. Murin[98], P. Murin[27b], W.J. Murray[174,140], A. Murrone[67a,67b], J.M. Muse[125], M. Muškinja[17], C. Mwewa[28], A.G. Myagkov[119,ad], A.J. Myers[7], A.A. Myers[135], G. Myers[64], M. Myska[138], B.P. Nachman[17], O. Nackenhorst[46], A.Nag Nag[47], K. Nagai[131], K. Nagano[80], J.L. Nagle[28], E. Nagy[99], A.M. Nairz[35], Y. Nakahama[80], K. Nakamura[80], H. Nanjo[129], F. Napolitano[60a], R. Narayan[41], E.A. Narayanan[114], I. Naryshkin[134], M. Naseri[33], C. Nass[23], G. Navarro[21a], J. Navarro-Gonzalez[170], R. Nayak[158], P.Y. Nechaeva[108], F. Nechansky[45], T.J. Neep[20], A. Negri[69a,69b], M. Negrini[22b], C. Nellist[115], C. Nelson[101], K. Nelson[103], S. Nemecek[137], M. Nessi[35,f], M.S. Neubauer[169], F. Neuhaus[97], J. Neundorf[45], R. Newhouse[171], P.R. Newman[20], C.W. Ng[135], Y.S. Ng[18], Y.W.Y. Ng[167], B. Ngair[34e], H.D.N. Nguyen[107], R.B. Nickerson[131], R. Nicolaidou[141], D.S. Nielsen[39], J. Nielsen[142], M. Niemeyer[52], N. Nikiforou[10], V. Nikolaenko[119,ad], I. Nikolic-Audit[132], K. Nikolopoulos[20], P. Nilsson[28], H.R. Nindhito[53], A. Nisati[71a], N. Nishu[2], R. Nisius[112], T. Nitta[175], T. Nobe[160], D.L. Noel[31], Y. Noguchi[84], I. Nomidis[132], M.A. Nomura[28], M.B. Norfolk[146], R.R.B. Norisam[93], J. Novak[90], T. Novak[45], O. Novgorodova[47], L. Novotny[138], R. Novotny[114], L. Nozka[127], K. Ntekas[167], E. Nurse[93], F.G. Oakham[33,ai], J. Ocariz[132], A. Ochi[81], I. Ochoa[136a], J.P. Ochoa-Ricoux[143a], S. Oda[86], S. Odaka[80], S. Oerdek[168], A. Ogrodnik[82a], A. Oh[98], C.C. Ohm[151], H. Oide[161], R. Oishi[160], M.L. Ojeda[45], Y. Okazaki[84], M.W. O'Keefe[89], Y. Okumura[160], A. Olariu[26b], L.F. Oleiro Seabra[136a], S.A. Olivares Pino[143d], D. Oliveira Damazio[28], D. Oliveira Goncalves[79a], J.L. Oliver[167], M.J.R. Olsson[167], A. Olszewski[83], J. Olszowska[83], Ö.O. Öncel[23], D.C. O'Neil[149], A.P. O'neill[19], A. Onofre[136a,136e], P.U.E. Onyisi[10], R.G. Oreamuno Madriz[117], M.J. Oreglia[36], G.E. Orellana[87], D. Orestano[73a,73b], N. Orlando[13], R.S. Orr[163], V. O'Shea[56], R. Ospanov[59a], G. Otero y Garzon[29], H. Otono[86], P.S. Ott[60a], G.J. Ottino[17], M. Ouchrif[34d], J. Ouellette[28], F. Ould-Saada[130], A. Ouraou[141,*], Q. Ouyang[14a], M. Owen[56], R.E. Owen[140], K.Y. Oyulmaz[11c], V.E. Ozcan[11c], N. Ozturk[7], S. Ozturk[11c,ab], J. Pacalt[127], H.A. Pacey[31], K. Pachal[48], A. Pacheco Pages[13], C. Padilla Aranda[13], S. Pagan Griso[17], G. Palacino[64], S. Palazzo[49], S. Palestini[35], M. Palka[82b], J. Pan[179], D.K. Panchal[10], C.E. Pandini[53], J.G. Panduro Vazquez[92], P. Pani[45], G. Panizzo[65a,65c], L. Paolozzi[53], C. Papadatos[107], S. Parajuli[41], A. Paramonov[5], C. Paraskevopoulos[9], D. Paredes Hernandez[61b], B. Parida[176], T.H. Park[163], A.J. Parker[30], M.A. Parker[31], F. Parodi[54b,54a], E.W. Parrish[117], V.A. Parrish[49], J.A. Parsons[38], U. Parzefall[51], L. Pascual Dominguez[158], V.R. Pascuzzi[17], F. Pasquali[116], E. Pasqualucci[71a], S. Passaggio[54b], F. Pastore[92], P. Pasuwan[44a,44b], J.R. Pater[98], A. Pathak[177], J. Patton[89], T. Pauly[35], J. Pearkes[150], M. Pedersen[130], R. Pedro[136a], S.V. Peleganchuk[118b,118a], O. Penc[137], C. Peng[61b], H. Peng[59a], M. Penzin[162], B.S. Peralva[79a], A.P. Pereira Peixoto[136a], L. Pereira Sanchez[44a,44b], D.V. Perepelitsa[28], E. Perez Codina[164a], M. Perganti[9], L. Perini[67a,67b], H. Pernegger[35], S. Perrella[35], A. Perrevoort[115], K. Peters[45], R.F.Y. Peters[98], B.A. Petersen[35], T.C. Petersen[39], E. Petit[99], V. Petousis[138], C. Petridou[159], A. Petrukhin[148], M. Pettee[17], N.E. Pettersson[35], K. Petukhova[139], A. Peyaud[141], R. Pezoa[143e], L. Pezzotti[35], G. Pezzullo[179], T. Pham[102], P.W. Phillips[140], M.W. Phipps[169], G. Piacquadio[152], E. Pianori[17], F. Piazza[67a,67b], A. Picazio[100], R. Piegaia[29], D. Pietreanu[26b], J.E. Pilcher[36], A.D. Pilkington[98], M. Pinamonti[65a,65c], J.L. Pinfold[2], C. Pitman Donaldson[93], D.A. Pizzi[33], L. Pizzimento[72a,72b], A. Pizzini[116], M.-A. Pleier[28], V. Plesanovs[51], V. Pleskot[139], E. Plotnikova[78], R. Poettgen[95], R. Poggi[53], L. Poggioli[132], I. Pogrebnyak[104], D. Pohl[23], I. Pokharel[52], G. Polesello[69a], A. Poley[149,164a], R. Polifka[138], A. Polini[22b], C.S. Pollard[131], Z.B. Pollock[124], V. Polychronakos[28], D. Ponomarenko[109], L. Pontecorvo[35], S. Popa[26a], G.A. Popeneciu[26d], L. Portales[4], D.M. Portillo Quintero[164a], S. Pospisil[138], P. Postolache[26c], K. Potamianos[131], I.N. Potrap[78], C.J. Potter[31], H. Potti[1], T. Poulsen[45], J. Poveda[170], T.D. Powell[146], G. Pownall[45], M.E. Pozo Astigarraga[35], A. Prades Ibanez[170], P. Pralavorio[99], M.M. Prapa[43], S. Prell[77], D. Price[98], M. Primavera[66a], M.A. Principe Martin[96], M.L. Proffitt[145], N. Proklova[109], K. Prokofiev[61c], F. Prokoshin[78], G. Proto[72a,72b], S. Protopopescu[28], J. Proudfoot[5], M. Przybycien[82a], D. Pudzha[134], P. Puzo[63], D. Pyatiizbyantseva[109], J. Qian[103], Y. Qin[98], T. Qiu[91], A. Quadt[52], M. Queitsch-Maitland[35], G. Rabanal Bolanos[58], F. Ragusa[67a,67b], J.A. Raine[53], S. Rajagopalan[28], K. Ran[14a,14d], D.F. Rassloff[60a], S. Rave[97], B. Ravina[56],

I. Ravinovich[176], M. Raymond[35], A.L. Read[130], N.P. Readioff[146], D.M. Rebuzzi[69a,69b], G. Redlinger[28], K. Reeves[42], D. Reikher[158], A. Reiss[97], A. Rej[148], C. Rembser[35], A. Renardi[45], M. Renda[26b], M.B. Rendel[112], A.G. Rennie[56], S. Resconi[67a], M. Ressegotti[54b,54a], E.D. Resseguie[17], S. Rettie[93], B. Reynolds[124], E. Reynolds[17], M. Rezaei Estabragh[178], O.L. Rezanova[118b,118a], P. Reznicek[139], E. Ricci[74a,74b], R. Richter[112], S. Richter[45], E. Richter-Was[82b], M. Ridel[132], P. Rieck[122], P. Riedler[35], M. Rijssenbeek[152], A. Rimoldi[69a,69b], M. Rimoldi[45], L. Rinaldi[22b,22a], T.T. Rinn[169], M.P. Rinnagel[111], G. Ripellino[151], I. Riu[13], P. Rivadeneira[45], J.C. Rivera Vergara[172], F. Rizatdinova[126], E. Rizvi[91], C. Rizzi[53], B.A. Roberts[174], B.R. Roberts[17], S.H. Robertson[101,x], M. Robin[45], D. Robinson[31], C.M. Robles Gajardo[143e], M. Robles Manzano[97], A. Robson[56], A. Rocchi[72a,72b], C. Roda[70a,70b], S. Rodriguez Bosca[60a], Y. Rodriguez Garcia[21a], A. Rodriguez Rodriguez[51], A.M. Rodríguez Vera[164b], S. Roe[35], A.R. Roepe[125], J. Roggel[178], O. Røhne[130], R.A. Rojas[172], B. Roland[51], C.P.A. Roland[64], J. Roloff[28], A. Romaniouk[109], M. Romano[22b], A.C. Romero Hernandez[169], N. Rompotis[89], M. Ronzani[122], L. Roos[132], S. Rosati[71a], B.J. Rosser[133], E. Rossi[163], E. Rossi[4], E. Rossi[68a,68b], L.P. Rossi[54b], L. Rossini[45], R. Rosten[124], M. Rotaru[26b], B. Rottler[51], D. Rousseau[63], D. Rousso[31], G. Rovelli[69a,69b], A. Roy[10], A. Rozanov[99], Y. Rozen[157], X. Ruan[32f], A.J. Ruby[89], T.A. Ruggeri[1], F. Rühr[51], A. Ruiz-Martinez[170], A. Rummler[35], Z. Rurikova[51], N.A. Rusakovich[78], H.L. Russell[172], L. Rustige[37], J.P. Rutherfoord[6], E.M. Rüttinger[146], K. Rybacki[88], M. Rybar[139], E.B. Rye[130], A. Ryzhov[119], J.A. Sabater Iglesias[53], P. Sabatini[170], L. Sabetta[71a,71b], H.F-W. Sadrozinski[142], R. Sadykov[78], F. Safai Tehrani[71a], B. Safarzadeh Samani[153], M. Safdari[150], S. Saha[101], M. Sahinsoy[112], A. Sahu[178], M. Saimpert[141], M. Saito[160], T. Saito[160], D. Salamani[35], G. Salamanna[73a,73b], A. Salnikov[150], J. Salt[170], A. Salvador Salas[13], D. Salvatore[40b,40a], F. Salvatore[153], A. Salzburger[35], D. Sammel[51], D. Sampsonidis[159], D. Sampsonidou[59d,59c], J. Sánchez[170], A. Sanchez Pineda[4], V. Sanchez Sebastian[170], H. Sandaker[130], C.O. Sander[45], I.G. Sanderswood[88], J.A. Sandesara[100], M. Sandhoff[178], C. Sandoval[21b], D.P.C. Sankey[140], M. Sannino[54b,54a], A. Sansoni[50], C. Santoni[37], H. Santos[136a,136b], S.N. Santpur[17], A. Santra[176], K.A. Saoucha[146], A. Sapronov[78], J.G. Saraiva[136a,136d], J. Sardain[99], O. Sasaki[80], K. Sato[165], C. Sauer[60b], F. Sauerburger[51], E. Sauvan[4], P. Savard[163,ai], R. Sawada[160], C. Sawyer[140], L. Sawyer[94], I. Sayago Galvan[170], C. Sbarra[22b], A. Sbrizzi[22b,22a], T. Scanlon[93], J. Schaarschmidt[145], P. Schacht[112], D. Schaefer[36], U. Schäfer[97], A.C. Schaffer[63], D. Schaile[111], R.D. Schamberger[152], E. Schanet[111], C. Scharf[18], N. Scharmberg[98], V.A. Schegelsky[134], D. Scheirich[139], F. Schenck[18], M. Schernau[167], C. Schiavi[54b,54a], Z.M. Schillaci[25], E.J. Schioppa[66a,66b], M. Schioppa[40b,40a], B. Schlag[97], K.E. Schleicher[51], S. Schlenker[35], K. Schmieden[97], C. Schmitt[97], S. Schmitt[45], L. Schoeffel[141], A. Schoening[60b], P.G. Scholer[51], E. Schopf[131], M. Schott[97], J. Schovancova[35], S. Schramm[53], F. Schroeder[178], H-C. Schultz-Coulon[60a], M. Schumacher[51], B.A. Schumm[142], Ph. Schune[141], A. Schwartzman[150], T.A. Schwarz[103], Ph. Schwemling[141], R. Schwienhorst[104], A. Sciandra[142], G. Sciolla[25], F. Scuri[70a], F. Scutti[102], C.D. Sebastiani[89], K. Sedlaczek[46], P. Seema[18], S.C. Seidel[114], A. Seiden[142], B.D. Seidlitz[28], T. Seiss[36], C. Seitz[45], J.M. Seixas[79b], G. Sekhniaidze[68a], S.J. Sekula[41], L. Selem[4], N. Semprini-Cesari[22b,22a], S. Sen[48], C. Serfon[28], L. Serin[63], L. Serkin[65a,65b], M. Sessa[73a,73b], H. Severini[125], S. Sevova[150], F. Sforza[54b,54a], A. Sfyrla[53], E. Shabalina[52], R. Shaheen[151], J.D. Shahinian[133], N.W. Shaikh[44a,44b], D. Shaked Renous[176], L.Y. Shan[14a], M. Shapiro[17], A. Sharma[35], A.S. Sharma[1], S. Sharma[45], P.B. Shatalov[120], K. Shaw[153], S.M. Shaw[98], P. Sherwood[93], L. Shi[93], C.O. Shimmin[179], Y. Shimogama[175], J.D. Shinner[92], I.P.J. Shipsey[131], S. Shirabe[53], M. Shiyakova[78], J. Shlomi[176], M.J. Shochet[36], J. Shojaii[102], D.R. Shope[151], S. Shrestha[124], E.M. Shrif[32f], M.J. Shroff[172], E. Shulga[176], P. Sicho[137], A.M. Sickles[169], E. Sideras Haddad[32f], O. Sidiropoulou[35], A. Sidoti[22b], F. Siegert[47], Dj. Sijacki[15], J.M. Silva[20], M.V. Silva Oliveira[35], S.B. Silverstein[44a], S. Simion[63], R. Simoniello[35], N.D. Simpson[95], S. Simsek[11c], S. Sindhu[52], P. Sinervo[163], V. Sinetckii[110], S. Singh[149], S. Singh[163], S. Sinha[45], S. Sinha[32f], M. Sioli[22b,22a], I. Siral[128], S.Yu. Sivoklokov[110], J. Sjölin[44a,44b], A. Skaf[52], E. Skorda[95], P. Skubic[125], M. Slawinska[83], K. Sliwa[166], V. Smakhtin[176], B.H. Smart[140],

J. Smiesko[139], S.Yu. Smirnov[109], Y. Smirnov[109], L.N. Smirnova[110,r], O. Smirnova[95], E.A. Smith[36], H.A. Smith[131], M. Smizanska[88], K. Smolek[138], A. Smykiewicz[83], A.A. Snesarev[108], H.L. Snoek[116], S. Snyder[28], R. Sobie[172,x], A. Soffer[158], C.A. Solans Sanchez[35], E.Yu. Soldatov[109], U. Soldevila[170], A.A. Solodkov[119], S. Solomon[51], A. Soloshenko[78], K. Solovieva[51], O.V. Solovyanov[119], V. Solovyev[134], P. Sommer[146], H. Son[166], A. Sonay[13], W.Y. Song[164b], A. Sopczak[138], A.L. Sopio[93], F. Sopkova[27b], S. Sottocornola[69a,69b], R. Soualah[121c], A.M. Soukharev[118b,118a], Z. Soumaimi[34e], D. South[45], S. Spagnolo[66a,66b], M. Spalla[112], M. Spangenberg[174], F. Spanò[92], D. Sperlich[51], G. Spigo[35], M. Spina[153], S. Spinali[88], D.P. Spiteri[56], M. Spousta[139], A. Stabile[67a,67b], R. Stamen[60a], M. Stamenkovic[116], A. Stampekis[20], M. Standke[23], E. Stanecka[83], B. Stanislaus[17], M.M. Stanitzki[45], M. Stankaityte[131], B. Stapf[45], E.A. Starchenko[119], G.H. Stark[142], J. Stark[99], D.M. Starko[164b], P. Staroba[137], P. Starovoitov[60a], S. Stärz[101], R. Staszewski[83], G. Stavropoulos[43], P. Steinberg[28], A.L. Steinhebel[128], B. Stelzer[149,164a], H.J. Stelzer[135], O. Stelzer-Chilton[164a], H. Stenzel[55], T.J. Stevenson[153], G.A. Stewart[35], M.C. Stockton[35], G. Stoicea[26b], M. Stolarski[136a], S. Stonjek[112], A. Straessner[47], J. Strandberg[151], S. Strandberg[44a,44b], M. Strauss[125], T. Strebler[99], P. Strizenec[27b], R. Ströhmer[173], D.M. Strom[128], L.R. Strom[45], R. Stroynowski[41], A. Strubig[44a,44b], S.A. Stucci[28], B. Stugu[16], J. Stupak[125], N.A. Styles[45], D. Su[150], S. Su[59a], W. Su[59d,145,59c], X. Su[59a], K. Sugizaki[160], V.V. Sulin[108], M.J. Sullivan[89], D.M.S. Sultan[74a,74b], L. Sultanaliyeva[108], S. Sultansoy[3c], T. Sumida[84], S. Sun[103], S. Sun[177], O. Sunneborn Gudnadottir[168], M.R. Sutton[153], M. Svatos[137], M. Swiatlowski[164a], T. Swirski[173], I. Sykora[27a], M. Sykora[139], T. Sykora[139], D. Ta[97], K. Tackmann[45,v], A. Taffard[167], R. Tafirout[164a], R.H.M. Taibah[132], R. Takashima[85], K. Takeda[81], E.P. Takeva[49], Y. Takubo[80], M. Talby[99], A.A. Talyshev[118b,118a], K.C. Tam[61b], N.M. Tamir[158], A. Tanaka[160], J. Tanaka[160], R. Tanaka[63], J. Tang[59c], Z. Tao[171], S. Tapia Araya[77], S. Tapprogge[97], A. Tarek Abouelfadl Mohamed[104], S. Tarem[157], K. Tariq[59b], G. Tarna[26b], G.F. Tartarelli[67a], P. Tas[139], M. Tasevsky[137], E. Tassi[40b,40a], G. Tateno[160], Y. Tayalati[34e], G.N. Taylor[102], W. Taylor[164b], H. Teagle[89], A.S. Tee[177], R. Teixeira De Lima[150], P. Teixeira-Dias[92], H. Ten Kate[35], J.J. Teoh[116], K. Terashi[160], J. Terron[96], S. Terzo[13], M. Testa[50], R.J. Teuscher[163,x], N. Themistokleous[49], T. Theveneaux-Pelzer[18], O. Thielmann[178], D.W. Thomas[92], J.P. Thomas[20], E.A. Thompson[45], P.D. Thompson[20], E. Thomson[133], E.J. Thorpe[91], Y. Tian[52], V.O. Tikhomirov[108,ae], Yu.A. Tikhonov[118b,118a], S. Timoshenko[109], E.X.L. Ting[1], P. Tipton[179], S. Tisserant[99], S.H. Tlou[32f], A. Tnourji[37], K. Todome[22b,22a], S. Todorova-Nova[139], S. Todt[47], M. Togawa[80], J. Tojo[86], S. Tokár[27a], K. Tokushuku[80], E. Tolley[124], R. Tombs[31], M. Tomoto[80,113], L. Tompkins[150], P. Tornambe[100], E. Torrence[128], H. Torres[47], E. Torró Pastor[170], M. Toscani[29], C. Tosciri[36], J. Toth[99,w], D.R. Tovey[146], A. Traeet[16], C.J. Treado[122], T. Trefzger[173], A. Tricoli[28], I.M. Trigger[164a], S. Trincaz-Duvoid[132], D.A. Trischuk[171], W. Trischuk[163], B. Trocmé[57], A. Trofymov[63], C. Troncon[67a], F. Trovato[153], L. Truong[32c], M. Trzebinski[83], A. Trzupek[83], F. Tsai[152], M. Tsai[103], A. Tsiamis[159], P.V. Tsiareshka[105], A. Tsirigotis[159,t], V. Tsiskaridze[152], E.G. Tskhadadze[156a], M. Tsopoulou[159], Y. Tsujikawa[84], I.I. Tsukerman[120], V. Tsulaia[17], S. Tsuno[80], O. Tsur[157], D. Tsybychev[152], Y. Tu[61b], A. Tudorache[26b], V. Tudorache[26b], A.N. Tuna[35], S. Turchikhin[78], I. Turk Cakir[3a], R. Turra[67a], P.M. Tuts[38], S. Tzamarias[159], P. Tzanis[9], E. Tzovara[97], K. Uchida[160], F. Ukegawa[165], P.A. Ulloa Poblete[143b], G. Unal[35], M. Unal[10], A. Undrus[28], G. Unel[167], K. Uno[160], J. Urban[27b], P. Urquijo[102], G. Usai[7], R. Ushioda[161], M. Usman[107], Z. Uysal[11d], V. Vacek[138], B. Vachon[101], K.O.H. Vadla[130], T. Vafeiadis[35], C. Valderanis[111], E. Valdes Santurio[44a,44b], M. Valente[164a], S. Valentinetti[22b,22a], A. Valero[170], R.A. Vallance[20], A. Vallier[99], J.A. Valls Ferrer[170], T.R. Van Daalen[145], P. Van Gemmeren[5], S. Van Stroud[93], I. Van Vulpen[116], M. Vanadia[72a,72b], W. Vandelli[35], M. Vandenbroucke[141], E.R. Vandewall[126], D. Vannicola[158], L. Vannoli[54b,54a], R. Vari[71a], E.W. Varnes[6], C. Varni[17], T. Varol[155], D. Varouchas[63], K.E. Varvell[154], M.E. Vasile[26b], L. Vaslin[37], G.A. Vasquez[172], F. Vazeille[37], D. Vazquez Furelos[13], T. Vazquez Schroeder[35], J. Veatch[52], V. Vecchio[98], M.J. Veen[116], I. Veliscek[131], L.M. Veloce[163], F. Veloso[136a,136c], S. Veneziano[71a], A. Ventura[66a,66b], A. Verbytskyi[112], M. Verducci[70a,70b], C. Vergis[23], M. Verissimo De Araujo[79b], W. Verkerke[116], J.C. Vermeulen[116],

C. Vernieri[150], P.J. Verschuuren[92], M. Vessella[100], M.L. Vesterbacka[122], M.C. Vetterli[149,ai], A. Vgenopoulos[159], N. Viaux Maira[143e], T. Vickey[146], O.E. Vickey Boeriu[146], G.H.A. Viehhauser[131], L. Vigani[60b], M. Villa[22b,22a], M. Villaplana Perez[170], E.M. Villhauer[49], E. Vilucchi[50], M.G. Vincter[33], G.S. Virdee[20], A. Vishwakarma[49], C. Vittori[22b,22a], I. Vivarelli[153], V. Vladimirov[174], E. Voevodina[112], M. Vogel[178], P. Vokac[138], J. Von Ahnen[45], E. Von Toerne[23], B. Vormwald[35], V. Vorobel[139], K. Vorobev[109], M. Vos[170], J.H. Vossebeld[89], M. Vozak[98], L. Vozdecky[91], N. Vranjes[15], M. Vranjes Milosavljevic[15], V. Vrba[138,*], M. Vreeswijk[116], N.K. Vu[99], R. Vuillermet[35], O.V. Vujinovic[97], I. Vukotic[36], S. Wada[165], C. Wagner[100], W. Wagner[178], S. Wahdan[178], H. Wahlberg[87], R. Wakasa[165], M. Wakida[113], V.M. Walbrecht[112], J. Walder[140], R. Walker[111], S.D. Walker[92], W. Walkowiak[148], A.M. Wang[58], A.Z. Wang[177], C. Wang[59a], C. Wang[59c], H. Wang[17], J. Wang[61a], P. Wang[41], R.-J. Wang[97], R. Wang[58], R. Wang[117], S.M. Wang[155], S. Wang[59b], T. Wang[59a], W.T. Wang[76], W.X. Wang[59a], X. Wang[14c], X. Wang[169], X. Wang[59c], Y. Wang[59a], Z. Wang[103], Z. Wang[59d,48,59c], Z. Wang[103], A. Warburton[101], R.J. Ward[20], N. Warrack[56], A.T. Watson[20], M.F. Watson[20], G. Watts[145], B.M. Waugh[93], A.F. Webb[10], C. Weber[28], M.S. Weber[19], S.A. Weber[33], S.M. Weber[60a], C. Wei[59a], Y. Wei[131], A.R. Weidberg[131], J. Weingarten[46], M. Weirich[97], C. Weiser[51], T. Wenaus[28], B. Wendland[46], T. Wengler[35], S. Wenig[35], N. Wermes[23], M. Wessels[60a], K. Whalen[128], A.M. Wharton[88], A.S. White[58], A. White[7], M.J. White[1], D. Whiteson[167], L. Wickremasinghe[129], W. Wiedenmann[177], C. Wiel[47], M. Wielers[140], N. Wieseotte[97], C. Wiglesworth[39], L.A.M. Wiik-Fuchs[51], D.J. Wilbern[125], H.G. Wilkens[35], L.J. Wilkins[92], D.M. Williams[38], H.H. Williams[133], S. Williams[31], S. Willocq[100], P.J. Windischhofer[131], I. Wingerter-Seez[4], F. Winklmeier[128], B.T. Winter[51], M. Wittgen[150], M. Wobisch[94], A. Wolf[97], R. Wölker[131], J. Wollrath[167], M.W. Wolter[83], H. Wolters[136a,136c], V.W.S. Wong[171], A.F. Wongel[45], S.D. Worm[45], B.K. Wosiek[83], K.W. Woźniak[83], K. Wraight[56], J. Wu[14a,14d], S.L. Wu[177], X. Wu[53], Y. Wu[59a], Z. Wu[141,59a], J. Wuerzinger[131], T.R. Wyatt[98], B.M. Wynne[49], S. Xella[39], L. Xia[14c], M. Xia[14b], J. Xiang[61c], X. Xiao[103], M. Xie[59a], X. Xie[59a], I. Xiotidis[153], D. Xu[14a], H. Xu[59a], H. Xu[59a], L. Xu[59a], R. Xu[133], T. Xu[59a], W. Xu[103], Y. Xu[14b], Z. Xu[59b], Z. Xu[150], B. Yabsley[154], S. Yacoob[32a], N. Yamaguchi[86], Y. Yamaguchi[161], H. Yamauchi[165], T. Yamazaki[17], Y. Yamazaki[81], J. Yan[59c], S. Yan[131], Z. Yan[24], H.J. Yang[59c,59d], H.T. Yang[17], S. Yang[59a], T. Yang[61c], X. Yang[59a], X. Yang[14a], Y. Yang[160], Z. Yang[103,59a], W-M. Yao[17], Y.C. Yap[45], H. Ye[14c], J. Ye[41], S. Ye[28], I. Yeletskikh[78], M.R. Yexley[88], P. Yin[38], K. Yorita[175], K. Yoshihara[77], C.J.S. Young[51], C. Young[150], M. Yuan[103], R. Yuan[59b,i], X. Yue[60a], M. Zaazoua[34e], B. Zabinski[83], G. Zacharis[9], E. Zaid[49], A.M. Zaitsev[119,ad], T. Zakareishvili[156b], N. Zakharchuk[33], S. Zambito[35], D. Zanzi[51], O. Zaplatilek[138], S.V. Zeißner[46], C. Zeitnitz[178], J.C. Zeng[169], D.T. Zenger Jr[25], O. Zenin[119], T. Ženiš[27a], S. Zenz[91], S. Zerradi[34a], D. Zerwas[63], B. Zhang[14c], D.F. Zhang[146], G. Zhang[14b], J. Zhang[5], K. Zhang[14a], L. Zhang[14c], M. Zhang[169], R. Zhang[177], S. Zhang[103], X. Zhang[59c], X. Zhang[59b], Z. Zhang[63], P. Zhao[48], T. Zhao[59b], Y. Zhao[142], Z. Zhao[59a], A. Zhemchugov[78], Z. Zheng[150], D. Zhong[169], B. Zhou[103], C. Zhou[177], H. Zhou[6], N. Zhou[59c], Y. Zhou[6], C.G. Zhu[59b], C. Zhu[14a,14d], H.L. Zhu[59a], H. Zhu[14a], J. Zhu[103], Y. Zhu[59a], X. Zhuang[14a], K. Zhukov[108], V. Zhulanov[118b,118a], D. Zieminska[64], N.I. Zimine[78], S. Zimmermann[51,*], J. Zinsser[60b], M. Ziolkowski[148], L. Živković[15], A. Zoccoli[22b,22a], K. Zoch[53], T.G. Zorbas[146], O. Zormpa[43], W. Zou[38], L. Zwalinski[35].

[1]Department of Physics, University of Adelaide, Adelaide; Australia.
[2]Department of Physics, University of Alberta, Edmonton AB; Canada.
[3](a)Department of Physics, Ankara University, Ankara;(b)Istanbul Aydin University, Application and Research Center for Advanced Studies, Istanbul;(c)Division of Physics, TOBB University of Economics and Technology, Ankara; Turkey.
[4]LAPP, Univ. Savoie Mont Blanc, CNRS/IN2P3, Annecy ; France.
[5]High Energy Physics Division, Argonne National Laboratory, Argonne IL; United States of America.
[6]Department of Physics, University of Arizona, Tucson AZ; United States of America.

[7]Department of Physics, University of Texas at Arlington, Arlington TX; United States of America.
[8]Physics Department, National and Kapodistrian University of Athens, Athens; Greece.
[9]Physics Department, National Technical University of Athens, Zografou; Greece.
[10]Department of Physics, University of Texas at Austin, Austin TX; United States of America.
[11] [(a)]Bahcesehir University, Faculty of Engineering and Natural Sciences, Istanbul;[(b)]Istanbul Bilgi University, Faculty of Engineering and Natural Sciences, Istanbul;[(c)]Department of Physics, Bogazici University, Istanbul;[(d)]Department of Physics Engineering, Gaziantep University, Gaziantep; Turkey.
[12]Institute of Physics, Azerbaijan Academy of Sciences, Baku; Azerbaijan.
[13]Institut de Física d'Altes Energies (IFAE), Barcelona Institute of Science and Technology, Barcelona; Spain.
[14] [(a)]Institute of High Energy Physics, Chinese Academy of Sciences, Beijing;[(b)]Physics Department, Tsinghua University, Beijing;[(c)]Department of Physics, Nanjing University, Nanjing;[(d)]University of Chinese Academy of Science (UCAS), Beijing; China.
[15]Institute of Physics, University of Belgrade, Belgrade; Serbia.
[16]Department for Physics and Technology, University of Bergen, Bergen; Norway.
[17]Physics Division, Lawrence Berkeley National Laboratory and University of California, Berkeley CA; United States of America.
[18]Institut für Physik, Humboldt Universität zu Berlin, Berlin; Germany.
[19]Albert Einstein Center for Fundamental Physics and Laboratory for High Energy Physics, University of Bern, Bern; Switzerland.
[20]School of Physics and Astronomy, University of Birmingham, Birmingham; United Kingdom.
[21] [(a)]Facultad de Ciencias y Centro de Investigaciónes, Universidad Antonio Nariño, Bogotá;[(b)]Departamento de Física, Universidad Nacional de Colombia, Bogotá; Colombia.
[22] [(a)]Dipartimento di Fisica e Astronomia A. Righi, Università di Bologna, Bologna;[(b)]INFN Sezione di Bologna; Italy.
[23]Physikalisches Institut, Universität Bonn, Bonn; Germany.
[24]Department of Physics, Boston University, Boston MA; United States of America.
[25]Department of Physics, Brandeis University, Waltham MA; United States of America.
[26] [(a)]Transilvania University of Brasov, Brasov;[(b)]Horia Hulubei National Institute of Physics and Nuclear Engineering, Bucharest;[(c)]Department of Physics, Alexandru Ioan Cuza University of Iasi, Iasi;[(d)]National Institute for Research and Development of Isotopic and Molecular Technologies, Physics Department, Cluj-Napoca;[(e)]University Politehnica Bucharest, Bucharest;[(f)]West University in Timisoara, Timisoara; Romania.
[27] [(a)]Faculty of Mathematics, Physics and Informatics, Comenius University, Bratislava;[(b)]Department of Subnuclear Physics, Institute of Experimental Physics of the Slovak Academy of Sciences, Kosice; Slovak Republic.
[28]Physics Department, Brookhaven National Laboratory, Upton NY; United States of America.
[29]Departamento de Física (FCEN) and IFIBA, Universidad de Buenos Aires and CONICET, Buenos Aires; Argentina.
[30]California State University, CA; United States of America.
[31]Cavendish Laboratory, University of Cambridge, Cambridge; United Kingdom.
[32] [(a)]Department of Physics, University of Cape Town, Cape Town;[(b)]iThemba Labs, Western Cape;[(c)]Department of Mechanical Engineering Science, University of Johannesburg, Johannesburg;[(d)]National Institute of Physics, University of the Philippines Diliman (Philippines);[(e)]University of South Africa, Department of Physics, Pretoria;[(f)]School of Physics, University of the Witwatersrand, Johannesburg; South Africa.
[33]Department of Physics, Carleton University, Ottawa ON; Canada.

[34] [(a)] Faculté des Sciences Ain Chock, Réseau Universitaire de Physique des Hautes Energies - Université Hassan II, Casablanca; [(b)] Faculté des Sciences, Université Ibn-Tofail, Kénitra; [(c)] Faculté des Sciences Semlalia, Université Cadi Ayyad, LPHEA-Marrakech; [(d)] LPMR, Faculté des Sciences, Université Mohamed Premier, Oujda; [(e)] Faculté des sciences, Université Mohammed V, Rabat; [(f)] Mohammed VI Polytechnic University, Ben Guerir; Morocco.
[35] CERN, Geneva; Switzerland.
[36] Enrico Fermi Institute, University of Chicago, Chicago IL; United States of America.
[37] LPC, Université Clermont Auvergne, CNRS/IN2P3, Clermont-Ferrand; France.
[38] Nevis Laboratory, Columbia University, Irvington NY; United States of America.
[39] Niels Bohr Institute, University of Copenhagen, Copenhagen; Denmark.
[40] [(a)] Dipartimento di Fisica, Università della Calabria, Rende; [(b)] INFN Gruppo Collegato di Cosenza, Laboratori Nazionali di Frascati; Italy.
[41] Physics Department, Southern Methodist University, Dallas TX; United States of America.
[42] Physics Department, University of Texas at Dallas, Richardson TX; United States of America.
[43] National Centre for Scientific Research "Demokritos", Agia Paraskevi; Greece.
[44] [(a)] Department of Physics, Stockholm University; [(b)] Oskar Klein Centre, Stockholm; Sweden.
[45] Deutsches Elektronen-Synchrotron DESY, Hamburg and Zeuthen; Germany.
[46] Fakultät Physik , Technische Universität Dortmund, Dortmund; Germany.
[47] Institut für Kern- und Teilchenphysik, Technische Universität Dresden, Dresden; Germany.
[48] Department of Physics, Duke University, Durham NC; United States of America.
[49] SUPA - School of Physics and Astronomy, University of Edinburgh, Edinburgh; United Kingdom.
[50] INFN e Laboratori Nazionali di Frascati, Frascati; Italy.
[51] Physikalisches Institut, Albert-Ludwigs-Universität Freiburg, Freiburg; Germany.
[52] II. Physikalisches Institut, Georg-August-Universität Göttingen, Göttingen; Germany.
[53] Département de Physique Nucléaire et Corpusculaire, Université de Genève, Genève; Switzerland.
[54] [(a)] Dipartimento di Fisica, Università di Genova, Genova; [(b)] INFN Sezione di Genova; Italy.
[55] II. Physikalisches Institut, Justus-Liebig-Universität Giessen, Giessen; Germany.
[56] SUPA - School of Physics and Astronomy, University of Glasgow, Glasgow; United Kingdom.
[57] LPSC, Université Grenoble Alpes, CNRS/IN2P3, Grenoble INP, Grenoble; France.
[58] Laboratory for Particle Physics and Cosmology, Harvard University, Cambridge MA; United States of America.
[59] [(a)] Department of Modern Physics and State Key Laboratory of Particle Detection and Electronics, University of Science and Technology of China, Hefei; [(b)] Institute of Frontier and Interdisciplinary Science and Key Laboratory of Particle Physics and Particle Irradiation (MOE), Shandong University, Qingdao; [(c)] School of Physics and Astronomy, Shanghai Jiao Tong University, Key Laboratory for Particle Astrophysics and Cosmology (MOE), SKLPPC, Shanghai; [(d)] Tsung-Dao Lee Institute, Shanghai; China.
[60] [(a)] Kirchhoff-Institut für Physik, Ruprecht-Karls-Universität Heidelberg, Heidelberg; [(b)] Physikalisches Institut, Ruprecht-Karls-Universität Heidelberg, Heidelberg; Germany.
[61] [(a)] Department of Physics, Chinese University of Hong Kong, Shatin, N.T., Hong Kong; [(b)] Department of Physics, University of Hong Kong, Hong Kong; [(c)] Department of Physics and Institute for Advanced Study, Hong Kong University of Science and Technology, Clear Water Bay, Kowloon, Hong Kong; China.
[62] Department of Physics, National Tsing Hua University, Hsinchu; Taiwan.
[63] IJCLab, Université Paris-Saclay, CNRS/IN2P3, 91405, Orsay; France.
[64] Department of Physics, Indiana University, Bloomington IN; United States of America.
[65] [(a)] INFN Gruppo Collegato di Udine, Sezione di Trieste, Udine; [(b)] ICTP, Trieste; [(c)] Dipartimento Politecnico di Ingegneria e Architettura, Università di Udine, Udine; Italy.
[66] [(a)] INFN Sezione di Lecce; [(b)] Dipartimento di Matematica e Fisica, Università del Salento, Lecce; Italy.

[67] (a) INFN Sezione di Milano; (b) Dipartimento di Fisica, Università di Milano, Milano; Italy.
[68] (a) INFN Sezione di Napoli; (b) Dipartimento di Fisica, Università di Napoli, Napoli; Italy.
[69] (a) INFN Sezione di Pavia; (b) Dipartimento di Fisica, Università di Pavia, Pavia; Italy.
[70] (a) INFN Sezione di Pisa; (b) Dipartimento di Fisica E. Fermi, Università di Pisa, Pisa; Italy.
[71] (a) INFN Sezione di Roma; (b) Dipartimento di Fisica, Sapienza Università di Roma, Roma; Italy.
[72] (a) INFN Sezione di Roma Tor Vergata; (b) Dipartimento di Fisica, Università di Roma Tor Vergata, Roma; Italy.
[73] (a) INFN Sezione di Roma Tre; (b) Dipartimento di Matematica e Fisica, Università Roma Tre, Roma; Italy.
[74] (a) INFN-TIFPA; (b) Università degli Studi di Trento, Trento; Italy.
[75] Institut für Astro- und Teilchenphysik, Leopold-Franzens-Universität, Innsbruck; Austria.
[76] University of Iowa, Iowa City IA; United States of America.
[77] Department of Physics and Astronomy, Iowa State University, Ames IA; United States of America.
[78] Joint Institute for Nuclear Research, Dubna; Russia.
[79] (a) Departamento de Engenharia Elétrica, Universidade Federal de Juiz de Fora (UFJF), Juiz de Fora; (b) Universidade Federal do Rio De Janeiro COPPE/EE/IF, Rio de Janeiro; (c) Instituto de Física, Universidade de São Paulo, São Paulo; Brazil.
[80] KEK, High Energy Accelerator Research Organization, Tsukuba; Japan.
[81] Graduate School of Science, Kobe University, Kobe; Japan.
[82] (a) AGH University of Science and Technology, Faculty of Physics and Applied Computer Science, Krakow; (b) Marian Smoluchowski Institute of Physics, Jagiellonian University, Krakow; Poland.
[83] Institute of Nuclear Physics Polish Academy of Sciences, Krakow; Poland.
[84] Faculty of Science, Kyoto University, Kyoto; Japan.
[85] Kyoto University of Education, Kyoto; Japan.
[86] Research Center for Advanced Particle Physics and Department of Physics, Kyushu University, Fukuoka ; Japan.
[87] Instituto de Física La Plata, Universidad Nacional de La Plata and CONICET, La Plata; Argentina.
[88] Physics Department, Lancaster University, Lancaster; United Kingdom.
[89] Oliver Lodge Laboratory, University of Liverpool, Liverpool; United Kingdom.
[90] Department of Experimental Particle Physics, Jožef Stefan Institute and Department of Physics, University of Ljubljana, Ljubljana; Slovenia.
[91] School of Physics and Astronomy, Queen Mary University of London, London; United Kingdom.
[92] Department of Physics, Royal Holloway University of London, Egham; United Kingdom.
[93] Department of Physics and Astronomy, University College London, London; United Kingdom.
[94] Louisiana Tech University, Ruston LA; United States of America.
[95] Fysiska institutionen, Lunds universitet, Lund; Sweden.
[96] Departamento de Física Teorica C-15 and CIAFF, Universidad Autónoma de Madrid, Madrid; Spain.
[97] Institut für Physik, Universität Mainz, Mainz; Germany.
[98] School of Physics and Astronomy, University of Manchester, Manchester; United Kingdom.
[99] CPPM, Aix-Marseille Université, CNRS/IN2P3, Marseille; France.
[100] Department of Physics, University of Massachusetts, Amherst MA; United States of America.
[101] Department of Physics, McGill University, Montreal QC; Canada.
[102] School of Physics, University of Melbourne, Victoria; Australia.
[103] Department of Physics, University of Michigan, Ann Arbor MI; United States of America.
[104] Department of Physics and Astronomy, Michigan State University, East Lansing MI; United States of America.
[105] B.I. Stepanov Institute of Physics, National Academy of Sciences of Belarus, Minsk; Belarus.

[106]Research Institute for Nuclear Problems of Byelorussian State University, Minsk; Belarus.
[107]Group of Particle Physics, University of Montreal, Montreal QC; Canada.
[108]P.N. Lebedev Physical Institute of the Russian Academy of Sciences, Moscow; Russia.
[109]National Research Nuclear University MEPhI, Moscow; Russia.
[110]D.V. Skobeltsyn Institute of Nuclear Physics, M.V. Lomonosov Moscow State University, Moscow; Russia.
[111]Fakultät für Physik, Ludwig-Maximilians-Universität München, München; Germany.
[112]Max-Planck-Institut für Physik (Werner-Heisenberg-Institut), München; Germany.
[113]Graduate School of Science and Kobayashi-Maskawa Institute, Nagoya University, Nagoya; Japan.
[114]Department of Physics and Astronomy, University of New Mexico, Albuquerque NM; United States of America.
[115]Institute for Mathematics, Astrophysics and Particle Physics, Radboud University/Nikhef, Nijmegen; Netherlands.
[116]Nikhef National Institute for Subatomic Physics and University of Amsterdam, Amsterdam; Netherlands.
[117]Department of Physics, Northern Illinois University, DeKalb IL; United States of America.
[118(a)]Budker Institute of Nuclear Physics and NSU, SB RAS, Novosibirsk;[(b)]Novosibirsk State University Novosibirsk; Russia.
[119]Institute for High Energy Physics of the National Research Centre Kurchatov Institute, Protvino; Russia.
[120]Institute for Theoretical and Experimental Physics named by A.I. Alikhanov of National Research Centre "Kurchatov Institute", Moscow; Russia.
[121(a)]New York University Abu Dhabi, Abu Dhabi;[(b)]United Arab Emirates University, Al Ain;[(c)]University of Sharjah, Sharjah; United Arab Emirates.
[122]Department of Physics, New York University, New York NY; United States of America.
[123]Ochanomizu University, Otsuka, Bunkyo-ku, Tokyo; Japan.
[124]Ohio State University, Columbus OH; United States of America.
[125]Homer L. Dodge Department of Physics and Astronomy, University of Oklahoma, Norman OK; United States of America.
[126]Department of Physics, Oklahoma State University, Stillwater OK; United States of America.
[127]Palacký University, Joint Laboratory of Optics, Olomouc; Czech Republic.
[128]Institute for Fundamental Science, University of Oregon, Eugene, OR; United States of America.
[129]Graduate School of Science, Osaka University, Osaka; Japan.
[130]Department of Physics, University of Oslo, Oslo; Norway.
[131]Department of Physics, Oxford University, Oxford; United Kingdom.
[132]LPNHE, Sorbonne Université, Université de Paris, CNRS/IN2P3, Paris; France.
[133]Department of Physics, University of Pennsylvania, Philadelphia PA; United States of America.
[134]Konstantinov Nuclear Physics Institute of National Research Centre "Kurchatov Institute", PNPI, St. Petersburg; Russia.
[135]Department of Physics and Astronomy, University of Pittsburgh, Pittsburgh PA; United States of America.
[136(a)]Laboratório de Instrumentação e Física Experimental de Partículas - LIP, Lisboa;[(b)]Departamento de Física, Faculdade de Ciências, Universidade de Lisboa, Lisboa;[(c)]Departamento de Física, Universidade de Coimbra, Coimbra;[(d)]Centro de Física Nuclear da Universidade de Lisboa, Lisboa;[(e)]Departamento de Física, Universidade do Minho, Braga;[(f)]Departamento de Física Teórica y del Cosmos, Universidad de Granada, Granada (Spain);[(g)]Instituto Superior Técnico, Universidade de Lisboa, Lisboa; Portugal.
[137]Institute of Physics of the Czech Academy of Sciences, Prague; Czech Republic.
[138]Czech Technical University in Prague, Prague; Czech Republic.

[139]Charles University, Faculty of Mathematics and Physics, Prague; Czech Republic.
[140]Particle Physics Department, Rutherford Appleton Laboratory, Didcot; United Kingdom.
[141]IRFU, CEA, Université Paris-Saclay, Gif-sur-Yvette; France.
[142]Santa Cruz Institute for Particle Physics, University of California Santa Cruz, Santa Cruz CA; United States of America.
[143][(a)]Departamento de Física, Pontificia Universidad Católica de Chile, Santiago;[(b)]Instituto de Investigación Multidisciplinario en Ciencia y Tecnología, y Departamento de Física, Universidad de La Serena;[(c)]Universidad Andres Bello, Department of Physics, Santiago;[(d)]Instituto de Alta Investigación, Universidad de Tarapacá, Arica;[(e)]Departamento de Física, Universidad Técnica Federico Santa María, Valparaíso; Chile.
[144]Universidade Federal de São João del Rei (UFSJ), São João del Rei; Brazil.
[145]Department of Physics, University of Washington, Seattle WA; United States of America.
[146]Department of Physics and Astronomy, University of Sheffield, Sheffield; United Kingdom.
[147]Department of Physics, Shinshu University, Nagano; Japan.
[148]Department Physik, Universität Siegen, Siegen; Germany.
[149]Department of Physics, Simon Fraser University, Burnaby BC; Canada.
[150]SLAC National Accelerator Laboratory, Stanford CA; United States of America.
[151]Department of Physics, Royal Institute of Technology, Stockholm; Sweden.
[152]Departments of Physics and Astronomy, Stony Brook University, Stony Brook NY; United States of America.
[153]Department of Physics and Astronomy, University of Sussex, Brighton; United Kingdom.
[154]School of Physics, University of Sydney, Sydney; Australia.
[155]Institute of Physics, Academia Sinica, Taipei; Taiwan.
[156][(a)]E. Andronikashvili Institute of Physics, Iv. Javakhishvili Tbilisi State University, Tbilisi;[(b)]High Energy Physics Institute, Tbilisi State University, Tbilisi; Georgia.
[157]Department of Physics, Technion, Israel Institute of Technology, Haifa; Israel.
[158]Raymond and Beverly Sackler School of Physics and Astronomy, Tel Aviv University, Tel Aviv; Israel.
[159]Department of Physics, Aristotle University of Thessaloniki, Thessaloniki; Greece.
[160]International Center for Elementary Particle Physics and Department of Physics, University of Tokyo, Tokyo; Japan.
[161]Department of Physics, Tokyo Institute of Technology, Tokyo; Japan.
[162]Tomsk State University, Tomsk; Russia.
[163]Department of Physics, University of Toronto, Toronto ON; Canada.
[164][(a)]TRIUMF, Vancouver BC;[(b)]Department of Physics and Astronomy, York University, Toronto ON; Canada.
[165]Division of Physics and Tomonaga Center for the History of the Universe, Faculty of Pure and Applied Sciences, University of Tsukuba, Tsukuba; Japan.
[166]Department of Physics and Astronomy, Tufts University, Medford MA; United States of America.
[167]Department of Physics and Astronomy, University of California Irvine, Irvine CA; United States of America.
[168]Department of Physics and Astronomy, University of Uppsala, Uppsala; Sweden.
[169]Department of Physics, University of Illinois, Urbana IL; United States of America.
[170]Instituto de Física Corpuscular (IFIC), Centro Mixto Universidad de Valencia - CSIC, Valencia; Spain.
[171]Department of Physics, University of British Columbia, Vancouver BC; Canada.
[172]Department of Physics and Astronomy, University of Victoria, Victoria BC; Canada.
[173]Fakultät für Physik und Astronomie, Julius-Maximilians-Universität Würzburg, Würzburg; Germany.
[174]Department of Physics, University of Warwick, Coventry; United Kingdom.

[175]Waseda University, Tokyo; Japan.
[176]Department of Particle Physics and Astrophysics, Weizmann Institute of Science, Rehovot; Israel.
[177]Department of Physics, University of Wisconsin, Madison WI; United States of America.
[178]Fakultät für Mathematik und Naturwissenschaften, Fachgruppe Physik, Bergische Universität Wuppertal, Wuppertal; Germany.
[179]Department of Physics, Yale University, New Haven CT; United States of America.
[a] Also at Borough of Manhattan Community College, City University of New York, New York NY; United States of America.
[b] Also at Bruno Kessler Foundation, Trento; Italy.
[c] Also at Center for High Energy Physics, Peking University; China.
[d] Also at Centro Studi e Ricerche Enrico Fermi; Italy.
[e] Also at CERN, Geneva; Switzerland.
[f] Also at Département de Physique Nucléaire et Corpusculaire, Université de Genève, Genève; Switzerland.
[g] Also at Departament de Fisica de la Universitat Autonoma de Barcelona, Barcelona; Spain.
[h] Also at Department of Financial and Management Engineering, University of the Aegean, Chios; Greece.
[i] Also at Department of Physics and Astronomy, Michigan State University, East Lansing MI; United States of America.
[j] Also at Department of Physics and Astronomy, University of Louisville, Louisville, KY; United States of America.
[k] Also at Department of Physics, Ben Gurion University of the Negev, Beer Sheva; Israel.
[l] Also at Department of Physics, California State University, East Bay; United States of America.
[m] Also at Department of Physics, California State University, Fresno; United States of America.
[n] Also at Department of Physics, California State University, Sacramento; United States of America.
[o] Also at Department of Physics, King's College London, London; United Kingdom.
[p] Also at Department of Physics, St. Petersburg State Polytechnical University, St. Petersburg; Russia.
[q] Also at Department of Physics, University of Fribourg, Fribourg; Switzerland.
[r] Also at Faculty of Physics, M.V. Lomonosov Moscow State University, Moscow; Russia.
[s] Also at Graduate School of Science, Osaka University, Osaka; Japan.
[t] Also at Hellenic Open University, Patras; Greece.
[u] Also at Institucio Catalana de Recerca i Estudis Avancats, ICREA, Barcelona; Spain.
[v] Also at Institut für Experimentalphysik, Universität Hamburg, Hamburg; Germany.
[w] Also at Institute for Particle and Nuclear Physics, Wigner Research Centre for Physics, Budapest; Hungary.
[x] Also at Institute of Particle Physics (IPP); Canada.
[y] Also at Institute of Theoretical Physics, Ilia State University, Tbilisi; Georgia.
[z] Also at Instituto de Fisica Teorica, IFT-UAM/CSIC, Madrid; Spain.
[aa] Also at Istanbul University, Dept. of Physics, Istanbul; Turkey.
[ab] Also at Istinye University, Istanbul; Turkey.
[ac] Also at Joint Institute for Nuclear Research, Dubna; Russia.
[ad] Also at Moscow Institute of Physics and Technology State University, Dolgoprudny; Russia.
[ae] Also at National Research Nuclear University MEPhI, Moscow; Russia.
[af] Also at Physics Department, An-Najah National University, Nablus; Palestine.
[ag] Also at Physikalisches Institut, Albert-Ludwigs-Universität Freiburg, Freiburg; Germany.
[ah] Also at The City College of New York, New York NY; United States of America.
[ai] Also at TRIUMF, Vancouver BC; Canada.
[aj] Also at Universita di Napoli Parthenope, Napoli; Italy.

[ak] Also at University of Chinese Academy of Sciences (UCAS), Beijing; China.
[al] Also at Yeditepe University, Physics Department, Istanbul; Turkey.
[*] Deceased